Large scale simulations of swirling and particle-laden flows using the Lattice-Boltzmann Method

Dominik Schuster

THÈSE

En vue de l'obtention du

DOCTORAT DE L'UNIVERSITÉ DE TOULOUSE

Délivré par :

Institut National Polytechnique de Toulouse (Toulouse INP)

Discipline ou spécialité :

Dynamique des fluides

Présentée et soutenue par :

M. DOMINIK SCHUSTER

le mardi 13 juillet 2021

Titre :

Large scale simulations of swirling and particle-laden flows using the Lattice-Boltzmann Method

---

Ecole doctorale :

Mécanique, Energétique, Génie civil, Procédés (MEGeP)

Unité de recherche :

Institut de Mécanique des Fluides de Toulouse (IMFT)

Directeur(s) de Thèse :

M. THIERRY POINSOT

M. ERIC CLIMENT

Rapporteurs :

M. PIERRE SAGAUT, AIX-MARSEILLE UNIVERSITE

M. TIMM KRUGER, UNIVERSITY OF EDINBURGH

Membre(s) du jury :

MME IVANA VINKOVIC, UNIVERSITE LYON 1, Président

M. ERIC CLIMENT, TOULOUSE INP, Membre

M. LAURENT LACAZE, TOULOUSE INP, Membre

M. PHILIPPE GONDRET, UNIVERSITE PARIS-SUD, Membre

M. THIERRY POINSOT, CNRS TOULOUSE, Membre

M. ULRICH RÜDE, UNIVERSITE D'ERLANGEN-NUREMBERG, Membre

Abstract

Since the development of high performance computers, numerical simulations have evolved into an important scientific tool by means of mathematical modeling to address physical problems that are complex to handle experimentally. Predicting the behavior of physical systems which are not directly observable helps to design and optimize new technology. Computational fluid dynamics in specific aims to understand natural flow phenomena as well as to design and operate engineering processes in industry. With the continuous increase in computational power every year, the question of how to efficiently use computational resources becomes increasingly more important. Improving existing practices involves a better understanding of the underlying physical mechanisms as well as optimizing the algorithms that are used to solve them with robust and rapid numerical methods. The Lattice-Boltzmann method (LBM) is a mesoscopic approach to approximate the macroscopic equations of mass and momentum balance equations for a fluid flow.

The objective of this study is to apply this concept to large scale problems and present its capabilities in terms of physical modelling and computing efficiency. As a validation step, computational models are tested against referenced theoretical, numerical and experimental evidences over a wide range of hydrodynamic conditions from creeping to turbulent flows and granular media. Turbulent flows are multi-scale flows that required fine meshes and long simulation times to converge statistics.Special care is taken to verify the fluid-solid interface for dispersed two-phase flows.Two main setups are examined – the non-reacting, swirling flow inside an injector and a particle-laden flow around a cylinder.

Swirling flows are typical of aeronautical combustion chambers. The selected configuration is used to benchmark three different large eddy simulation solvers regarding their accuracy and computational efficiency. The obtained numerical results are compared to experimental results in terms of mean and fluctuating velocity profiles and pressure drop. The scaling, that is the code performance on a large range of processors, is characterized. Differences between several algorithmic approaches and different solvers are evaluated and commented.

Next, we focused on particle laden flows around a cylinder as generic configuration for the interaction of a dispersed phase and flow hydrodynamic instabilities. It has been shown that the viscosity of a suspension increases relative to the particle volume fraction and for a certain range of particle material and concentration, this a fairly good model of interphase coupling. This phenomenon only occurs in numerical simulations that are able to describe finite size effects for rigid bodies. Comparing global flow parameters of suspensions at different particle volume fractions and sizes have shown that these flow features can be obtained for an equivalent single phase fluid with effective viscosity. Starting from neutrally buoyant particles the transition to granular flow is investigated. By increasing the relative density of particles, the influence of particle inertia on the equivalent fluid prediction is investigated and the contribution of particle collisions on the drag coefficient for varying relative densities is discussed. Conclusions are drawn regarding the code performance and physical representativeness of results.

Résumé

Depuis le développement des ordinateurs à haute performance, les simulations numériques sont devenues un outil scientifique important qui permet, grâce à la modélisation mathématique, de résoudre des problèmes physiques complexes à traiter expérimentalement. La prédiction du comportement de systèmes physiques qui ne sont pas directement observables aide à concevoir et à optimiser de nouvelles technologies. La mécanique des fluides numérique est un outil important qui nous aide à comprendre les phénomènes naturels et à dimensionner et opérer des procédés complexes d'ingénierie dans l'industrie. Avec l'augmentation continue des ressources de calcul au fur et à mesure des années, la question de savoir comment utiliser ces moyens de manière efficace, robuste et précise devient de plus en plus importante. L'amélioration des pratiques existantes implique une meilleure compréhension des mécanismes physiques sous-jacents ainsi que l'optimisation des algorithmes employées pour résoudre les équations de bilan.

La méthode de Lattice-Boltzmann (LBM) est une approche mésoscopique permettant d'approximer les équations macroscopiques de conservation de la masse et de la quantité de mouvement d'un fluide. L'objectif de cette étude est d'appliquer cette approche à des simulations de grande échelle et de présenter ses performances numériques et physiques. Deux configurations principales sont examinées – un écoulement swirlé non-réactif à l'intérieur d'un injecteur et un écoulement chargé en particules autour d'un cylindre. Afin de valider les modélisations et techniques numériques retenues, nous avons conduit plusieurs tests par rapport à des prédictions théoriques, numériques et expérimentales de la littérature pour une large gamme d'écoulements allant du régime de Stokes aux écoulements turbulents.

Les écoulements swirlés sont typiques des chambres de combustion aéronautiques. La configuration retenue a été choisie pour évaluer la précision et l'efficacité de trois solveurs différents de simulation des grandes structures de la turbulence. Les résultats de simulation numérique sont comparés à des résultats expérimentaux en termes de profils de vitesse moyenne et fluctuante et de perte de charge. La mise à l'échelle, c'est-à-dire la performance du code sur une grande gamme de processeurs a été caractérisée ainsi que les différences entre les différentes approches algorithmiques.

Le deuxième cas d'étude est celui d'un fluide chargé en particules s'écoulant autour d'un cylindre. Ceci permet de prendre en compte l'effet d'augmentation de la viscosité effective de la suspension en fonction de la fraction volumique des particules. Ce phénomène n'apparaît en simulation numérique que si les particules sont rigides et de taille finie. Cette approximation d'un fluide diphasique en milieu équivalent est confirmée en comparant les paramètres d'écoulement globaux.En partant de particules à flottabilité neutre, la transition vers un écoulement granulaire est analysée. L'influence de l'inertie des particules est mise en évidence sur la réponse de l'écoulement en augmentant la densité relative des particules, En particulier, la contribution des collisions des particules avec le cylindre sur le coefficient de traînée pour des densités relatives variables est discutée. Pour conclure, nous avons dressé un bilan des performances de calcul mais aussi de représentativité physique des résultats.

Acknowledgments

First I would like to thank all members of the jury for agreeing to evaluate my PhD work. Especially Pierre Sagaut and Timm Krüger for reviewing my manuscript.

I am deeply thankful for the supervision by Thierry Poinsot, who is an excellent motivator and Eric Climent, who dedicated much of his time to discuss with me about relevant issues. You lead me well through world of science and I learned a lot from you. I also want to thank Ulrich Rüde, who assisted many times with valuable advice and suggestions.

The last three years I was lucky enough to be part of the CFD team at CERFACS, which offered many social exchanges as well as opportunities for scientific development. Thank you Jean-François Boussuge and Gabriel Staffelbach for your support on LBM and HPC during many joint meetings. I greatly appreciated the fast and persevering technical support of the CSG group.

Likewise, I enjoyed being a member of the MiR group at IMFT and their heated discussions during lunch time. Thank you Laurent Selle for your advice.

I want to say thank you to the waLBerla team at LSS Erlangen-Nürnberg for introducing me to LBM and continuously assisting me in technical and scientific questions. In particular, there is Christoph Rettinger who helped me numerous times with the fluid-solid coupling and Martin Bauer & Markus Holzer, who assisted me with the code generation aspects. I also need to highlight the efforts by Andrea Aniello and Paul Werner for operating AVBP and ProLB, respectively during the collaboration on the swirler geometry. It was a pleasure working together.

This PhD was a marvelous experience and part of the journey, which is my life. It would not have been possible without the support of some very special people. Finally, I want to express my gratitude to the people who supported on a personal level me along the way: my family and my extended family - my friends.

I would like to thank the support and computational resources (500,000 CPU hours) provided by CALMIP on Olympe supercomputer (project P19040). Furthermore, this work was granted access to the HPC resources (4,500,000 CPU hours) of CINES, IDRIS, TGCC under the allocation 2020-A0082B11478 made by GENCI.

Acronyms

BB	**B**ounce **B**ack
BE	**B**oltzmann **E**quation
BGK	**B**hatnagar-**G**ross-**K**rook
CFD	**C**omputational **F**luid **D**ynamics
CFL	**C**ourant-**F**riedrichs-**L**ewy
CLI	**C**entral **L**inear **I**nterpolated
DC	**D**irect-**C**oupling
DEM	**D**iscrete **E**lement **M**ethod
EFN	**E**quivalent **F**ine **N**odes
EFFN	**E**quivalent **F**ine **F**luid **N**odes
FV	**F**inite **V**olume
HPC	**H**igh **P**erformance **C**omputing
HRR	**H**ybrid **R**ecursive **R**egularized
IRZ	**I**nner **R**ecirculation **Z**one
KBC	**K**arlin **B**ösch **C**hikatamarla
LB	**L**attice **B**oltzmann
LBM	**L**attice **B**oltzmann **M**ethod
LDV	**L**aser **D**oppler **V**elocimetry
LES	**L**arge **E**ddy **S**imulation
MLUPS	**M**ega **L**attice **U**pdates **P**er **S**econd
MFLUPS	**M**ega **F**luid **L**attice **U**pdates **P**er **S**econd

MPI	**M**essage **P**assing **I**nterface
MRT	**M**ulti-**R**elaxation **T**ime
MR	**M**ulti-**R**eflection
PDF	**P**article **D**istribution **F**unction
PGS	**P**ressure **G**radient **S**caling
PIV	**P**article **I**mage **V**elocimetry
PSD	**P**ower **S**pectral **D**ensity
RANS	**R**eynolds **A**veraged **N**avier-**S**tokes
RMS	**R**oot **M**ean **S**quare
SGS	**S**ub**G**rid **S**cale
TRT	**T**wo-**R**elaxation **T**ime

Contents

Chapter 1

Introduction

Numerical simulations are a valuable complement to experiments for engineering and research configurations. In many cases, experimental measurements are technically infeasible or simply too expensive to perform. On the other hand, the numerical approach is comparatively cost-effective and can be set up in a short time, but requires a certain amount of experimental validation. Simulations provide access to all relevant quantities at any point in space and time within the computational domain and allow rapid adaptation to an existing design. Since a new physical prototype does not need to be built for each design iteration, simulations are often used for optimization in fluid dynamic problems.

It cannot be claimed that the Lattice Boltzmann method (LBM) is a novel concept for computational fluid dynamics (CFD). The mathematical foundation, i.e. the link between the Boltzmann equation (BE) and the Navier-Stokes equations (NSE) was derived by Chapman [1] and Enskog [2] in 1916/17, the first model for the collision process - which is still used today - was described by Bhatnagar, Gross and Krook (BGK) in 1954 [3] and the first actual fluid flow simulation was performed by Frisch, Hasslacher and Pomeau in 1986 [4]. However, new scientific developments and the rise of massively parallel supercomputers have sparked the interest in the method. There are conceptual differences that arise from LBM's origin in kinetic theory in contrast to classic CFD methods (Finite difference, finite volume, finite element), which are based on continuum theory. Case in point: there is no need to explicitly solve a Poisson's equation and thus LBM can be solved strictly local. Due to the velocity discretization of the BE on a Cartesian grid, the LBM is essentially a *stencil code*, which is generally easy to implement and has obvious advantages in the context of massively parallel computations.

In recent years, we were able to witness the success of applying the LBM to engineering problems such as multiphase flows [5, 6, 7], aeroacoustics for aircraft and cars [8], heat transfer [9] or turbulent flows in complex geometries [10]. Even though the standard LBM is limited to isothermal and weakly compressible to incompressible flows, there have been advances in its extensions to compressible flows [11, 12, 13]. Simulation of hemodynamics has been demonstrated with a focus on code performance and scalability [14].

The LBM is well suited to perform on GPU [15] and heterogeneous (CPU&GPU) architectures [16], which are becoming more prevalent in modern future supercomputers. Löhner [17] argues that the "LES crisis", i.e. the barrier of running computations with $O(10^9)$ degrees of freedom and $O(10^7)$ timesteps during one night, could be overcome in the next few years and that the LBM is a good candidate for achieving this goal. Indeed, the extreme dimensions to which the method can be scaled up has been recently exemplified by SunwayLB [18] by sustaining a performance of 4.7 PFlops on 10,400,000 cores of the Sunway TaihuLight computer.

Comparing the efficiency to classic methods [19, 20] is a difficult task since great care has to be taken to find unbiased initial conditions and define appropriate accuracy criteria. As we will see later, the inherent restriction of LBM to Cartesian grids prevents us from comparing results on the same mesh that would typically be used in a finite volume solver. However, running the finite volume solver on a Cartesian grid would constitute an evident disadvantage in complex geometries.

For our simulations, we use the software framework waLBerla[1], which is built on previous work of Godenschwager [21], Feichtinger [22], Götz [23], Schornbaum [24], Bartuschat [25], Rettinger [26]. Complementary, the code generation technique of *lbmpy*[2] is employed, which is based on the development by Bauer [27] . The current work is dedicated to continuing and expanding on these efforts.

The first objective of the present PhD was to explore the potential of waLBerla's tools in the framework of IMFT (Institut de Mécanique des Fluides de Toulouse), where multiple codes are used for CFD. Two specific domains were targeted:

- Aerodynamics in turbulent flows : The intrinsic nature of LBM sometimes makes it difficult to apply near walls, where adaptive meshes are preferred by many groups.
- Two phase flows: The capacity of LBM to handle large meshes with inclusions of particles is an attractive feature at IMFT, where multiple groups tackle such phenomena.

Even though the comparison of LBM codes with classical CFD solvers is difficult because they use different meshes, we tried to give a fair comparison by investigating code performance at "fixed precision". We also checked the intrinsic performance of the waLBerla framework by comparing it to another LBM code, which is a reference in this field: the ProLB solver developed by AMU, Renault, Airbus, LMFA and CS.

This Thesis is a collaboration, that brings together the knowledge of aerodynamics at CERFACS (Centre Européen de Recherche et de Formation Avancée en Calcul Scientifique), the research group involved in particle-laden flows at IMFT and the high performance computing (HPC) code development at LSS (Lehrstuhl für Systemsimulation, Friedrich-Alexander-Universität Erlangen-Nürnberg).

The manuscript is organized as follows: Chap. 2 outlines the path from kinetic theory to the continuous NSE and introduces the methods and models that are needed later. It also highlights some aspects of the implementation of these methods in waLBerla and *lbmpy*. Several configurations, such as the first and second Stokes problems [28, 29], the Basset history force [30, 31], the Segré-Silberberg effect [32] and the turbulent flow between two plates [33], are tested and compared to analytic or empirical solutions in Chap. 3 to verify the accuracy of our simulation approach for flows from the Stokes regime to turbulent flows, the momentum exchange between particle and fluid and the dynamics of rigid bodies. The main results are found in Chap. 4 and Chap. 5. The former presents the comparison between three different fluid dynamics solvers for a swirling flow at moderate Reynolds number and the latter explores the generic configuration of the flow around a cylinder but with the presence of resolved particles. Our findings are summarized and an outlook for future projects is given in Chap. 6.

[1] `https://www.walberla.net`
[2] `https://pypi.org/project/lbmpy/`

Chapter 2

Methods and implementation

Contents

The first part of this chapter outlines the physical fundamentals of fluid and gas dynamics. We start at the Navier-Stokes equations (NSE), which describe the fluid as a continuum, followed by the Boltzmann equation (BE), which is based on the mesoscopic description of kinetic theory. The connection between BE and NSE will be explained briefly. We will construct the LBM by discretizing the BE in space, time and velocity. Different models for the collision operator are introduced, such as the BGK, MRT, TRT and cumulant models. Two methods for simulating turbulent flows are presented: the Smagorinksy type SGS model and the entropic stabilization. Next, we show how to include external forces and present boundary conditions, refilling schemes for empty fluid cells and the collision modeling of the granular solver. The last section highlights certain aspects of the implementation of these methods in the framework of waLBerla *and* lbmpy*. We discuss the single node performance, the mesh creation procedure for complex geometries and the fluid-solid coupling algorithm.*

2.1 Hydrodynamic flow description

2.1.1 Laws of conservation

Common fluids are composed of a large number of individual molecules, but from a macroscopic viewpoint can be interpreted as a continuum. Inside a constant fluid element mass and momentum are balanced through the laws of conservation

$$\frac{\partial \rho}{\partial t} + \boldsymbol{\nabla} \cdot (\rho \boldsymbol{u}) = 0 \tag{2.1}$$

and

$$\frac{\partial (\rho \boldsymbol{u})}{\partial t} + \boldsymbol{\nabla} \cdot (\rho \boldsymbol{u}\boldsymbol{u}) = -\boldsymbol{\nabla} p + \boldsymbol{F}, \tag{2.2}$$

with the fluid density ρ, velocity $\boldsymbol{u}$, pressure p and an external force $\boldsymbol{F}$. They were first derived by Euler [34] for flows that exclusively involve isotropic stress, i.e. inviscid fluids.

2.1.2 Navier-Stokes equations

When taking shear stress into account, the momentum equation has to be complemented by the deviatoric stress tensor σ:

$$\frac{\partial (\rho \boldsymbol{u})}{\partial t} + \boldsymbol{\nabla} \cdot (\rho \boldsymbol{u}\boldsymbol{u}) = -\nabla p + \boldsymbol{\nabla} \cdot \sigma + \boldsymbol{F} \tag{2.3}$$

While the transfer of momentum in the Euler equation Eq. (2.2) is reversible, viscous fluids exhibit internal friction, which leads to an irreversible and dissipative transfer of momentum. This general form of momentum equation was first proposed by Cauchy [35] and later put into the context of fluid mechanics by Stokes [36] to form the famous Navier-Stokes equations (NSE). The viscous stress tensor in the NSE can be written as

$$\sigma = \mu \left(\boldsymbol{\nabla} \boldsymbol{u} + (\boldsymbol{\nabla} \boldsymbol{u})^{\mathsf{T}} \right) + \xi \left(\boldsymbol{\nabla} \cdot \boldsymbol{u} \right) \mathbf{I}, \tag{2.4}$$

where μ is the dynamic viscosity, ξ is the second viscosity and $\mathbf{I}$ is the identity matrix. This tensor can be split into a normal and a shear stress

$$\sigma = \mu \left(\boldsymbol{\nabla} \boldsymbol{u} + (\boldsymbol{\nabla} \boldsymbol{u})^{\mathsf{T}} - 2/3 \left(\boldsymbol{\nabla} \cdot \boldsymbol{u} \right) \mathbf{I} \right) + \mu_B \left(\boldsymbol{\nabla} \cdot \boldsymbol{u} \right) \mathbf{I}, \tag{2.5}$$

introducing the bulk viscosity $\mu_B = 2\mu/3 + \xi$. In the case that the dynamic viscosity is assumed to be constant, the NSE can be simplified to

$$\frac{\partial (\rho \boldsymbol{u})}{\partial t} + \boldsymbol{\nabla} \cdot (\rho \boldsymbol{u}\boldsymbol{u}) = -\nabla p + \mu \boldsymbol{\Delta} \boldsymbol{u} + (\mu_B + \mu/3) \, \boldsymbol{\nabla} (\boldsymbol{\nabla} \cdot \boldsymbol{u}) + \boldsymbol{F}. \tag{2.6}$$

Additionally, the velocity field of an incompressible flow with constant density is divergence free $\boldsymbol{\nabla} \cdot \boldsymbol{u} = 0$, which allows us to reduce the NSE to it's incompressible form

$$\rho \frac{D \boldsymbol{u}}{D t} = -\nabla p + \mu \boldsymbol{\Delta} \boldsymbol{u} + \boldsymbol{F}, \tag{2.7}$$

using the material derivative $\frac{D}{Dt} = \frac{\partial}{\partial t} + \boldsymbol{u} \cdot \boldsymbol{\nabla}$.

2.1.3 Equation of state

To solve the incompressible NSE, the conservation of mass and momentum are sufficient. If the density is not constant, an additional equation is needed to close the system of equations. Following the thermodynamics of fluids [37], the ideal gas law is introduced

$$p = \rho R T, \tag{2.8}$$

with the specific gas constant R and the temperature T. From the expansion of the discrete Boltzmann equation to second order it can be shown that the Lattice Boltzmann equations are linked to the NSE via the isothermal equation of state [38]. While it is possible to use alternative equations of state to better model thermal flows, we consider only isothermal flows in the context of this thesis. Hence the temperature is assumed to be constant $T = T_0$, so that the state equation used here becomes $p = \rho R T_0$. Using the general definition of the speed of sound c_s at constant entropy S

$$c_s^2 = \left(\frac{\partial p}{\partial \rho}\right)_S \tag{2.9}$$

the pressure can be expressed as a reference value plus fluctuation:

$$p = c_s^2 \rho_0 + c_s^2 \rho'. \tag{2.10}$$

This expression is also valid for nonlinear equations of state if the deviation from the reference state

$$p' = p - p_0 \tag{2.11}$$

is small, so that it can be approximated by linearization.

2.2 Kinetic theory

The statistical behavior of microscopic particles (atoms, molecules) in a gas is modeled by kinetic theory and developed out of the works of Maxwell [39] and Boltzmann [40]. It is based on the particle distribution function (PDF) $f(\boldsymbol{\xi}, \boldsymbol{x}, t)$, which describes the probability density of finding *fictive particles* with microscopic velocity $\boldsymbol{\xi}$ at position $\boldsymbol{x}$ and time t. The evolution of this distribution function is given by the Boltzmann equation

$$\frac{\partial f}{\partial t} + \boldsymbol{\xi} \cdot \boldsymbol{\nabla} f + \frac{\boldsymbol{F}}{\rho} \cdot \boldsymbol{\nabla}_{\boldsymbol{\xi}} f = \Omega_f, \tag{2.12}$$

where Ω_f is the collision operator and $\boldsymbol{F}$ is an external body force. Integration of the PDF over the microscopic velocity space yields moments, that consider the contribution of particles of all velocities. These moments are used to recover macroscopic quantities such as mass density ρ, momentum density $\rho \boldsymbol{u}$, total energy density ρE and internal energy density ρe as follows:

$$\rho(\boldsymbol{x}, t) = \int f(\boldsymbol{x}, \boldsymbol{\xi}, t) d\boldsymbol{\xi}, \tag{2.13a}$$

$$\rho(\boldsymbol{x}, t)\boldsymbol{u}(\boldsymbol{x}, t) = \int \boldsymbol{\xi} f(\boldsymbol{x}, \boldsymbol{\xi}, t) d\boldsymbol{\xi}, \tag{2.13b}$$

$$\rho(\boldsymbol{x}, t)E(\boldsymbol{x}, t) = \frac{1}{2} \int |\boldsymbol{\xi}|^2 f(\boldsymbol{x}, \boldsymbol{\xi}, t) d\boldsymbol{\xi}, \tag{2.13c}$$

$$\rho(\boldsymbol{x}, t)e(\boldsymbol{x}, t) = \frac{1}{2} \int |\boldsymbol{\xi} - \boldsymbol{u}|^2 f(\boldsymbol{x}, \boldsymbol{\xi}, t) d\boldsymbol{\xi}. \tag{2.13d}$$

The left hand side of the Boltzmann equation corresponds to the advection of the PDF, whereas the right hand side describes local redistribution of f caused by the collision of fictive particles. Finding a suitable model for this collision operator is an essential part of setting up the LBM. Since collisions conserve the quantities of mass, momentum and energy, the collision model must satisfy the conservation laws of following quantities:

$$\int \Omega(f)\,\mathrm{d}^3\xi = 0, \tag{2.14a}$$

$$\int \boldsymbol{\xi}\Omega(f)\,\mathrm{d}^3\xi = 0, \tag{2.14b}$$

$$\int |\boldsymbol{\xi}|^2\Omega(f)\,\mathrm{d}^3\xi = 0, \tag{2.14c}$$

$$\int |\boldsymbol{\xi} - \boldsymbol{u}|^2\Omega(f)\,\mathrm{d}^3\xi = 0. \tag{2.14d}$$

The simplest form is the Bhatnagar, Gross and Krook (BGK) [3] operator:

$$\Omega^{\mathrm{BGK}} = -\frac{1}{\tau}\left(f - f^{\mathrm{eq}}\right), \tag{2.15}$$

which specifies the collision as relaxation of distribution functions towards an equilibrium state f^{eq} with relaxation time τ. The relaxation time is determined by viscosity and heat diffusivity (if thermal equations are considered). The equilibrium distribution is given by a Maxwell-Boltzmann distribution [41]:

$$f^{\mathrm{eq}} = \rho\left(\frac{1}{(2\pi RT)}\right)^{3/2}\exp\left(-\frac{|\boldsymbol{\xi} - \boldsymbol{u}|^2}{2RT}\right). \tag{2.16}$$

The macroscopic continuity equations can be recovered from the Boltzmann equation [42]. For this purpose the PDF is expanded as deviations from the equilibrium distribution in powers of the Knudsen number:

$$f = f^{\mathrm{eq}} + \epsilon(\mathrm{Kn})f^{(1)} + \epsilon^2(\mathrm{Kn})f^{(2)} + ... \tag{2.17}$$

The Knudsen number is given as the ratio between the particle mean free path λ and the physical length scale L

$$\mathrm{Kn} = \frac{\lambda}{L} \propto \frac{\mathrm{Ma}}{\mathrm{Re}}. \tag{2.18}$$

and it is also proportional to ratio of Mach number to Reynolds number. When the Knudsen number is low, the fluid is dominated by collisions and the PDF is approximately equal to its local equilibrium $f = f^{\mathrm{eq}}$. This yields the macroscopic Euler equations, which are found by integration of the Boltzmann equation over velocity space:

$$\frac{\partial}{\partial t}\int f\,\mathrm{d}^3\xi + \frac{\partial}{\partial x_j}\int \xi_j f\,\mathrm{d}^3\xi + \frac{F_j}{\rho}\int \frac{\partial f}{\partial \xi_j}\,\mathrm{d}^3\xi = \int \Omega_f\,\mathrm{d}^3\xi. \tag{2.19}$$

To solve the terms in this equation we introduce the moments of f

$$\Pi_0 = \int f\,\mathrm{d}^3\xi = \rho, \qquad \Pi_i = \int \xi_i f\,\mathrm{d}^3\xi = \rho u_i, \tag{2.20a}$$

$$\Pi_{ij} = \int \xi_i\xi_j f\,\mathrm{d}^3\xi, \qquad \Pi_{ijk} = \int \xi_i\xi_j\xi_k f\,\mathrm{d}^3\xi, \tag{2.20b}$$

where the first two moments are equivalent to Eq. (2.13) and the second order moment Π_{ij} is the momentum flux tensor. The moments of the force term are obtained through multidimensional integration by parts [43] as

$$\int \frac{\partial f}{\partial \xi_j} \, \mathrm{d}^3\xi = 0, \qquad \int \xi_i \frac{\partial f}{\partial \xi_j} \, \mathrm{d}^3\xi = \int \frac{\partial \xi_i}{\partial \xi_j} f \, \mathrm{d}^3\xi = -\rho\delta_{ij}. \tag{2.21}$$

By using these moment definitions and the conservation properties of the collision operator in Eq. (2.14), Eq. (2.19) simplifies to

$$\frac{\partial(\rho)}{\partial t} + \frac{\partial\left(\rho u_j\right)}{\partial x_j} = 0, \tag{2.22}$$

which is equivalent to the continuity equation from Eq. (2.1). Likewise, the momentum conservation is found by first multiplying the Boltzmann equation by ξ_α and then integrating over velocity space:

$$\frac{\partial((\rho u_i))}{\partial t} + \frac{\partial \Pi_{ij}}{\partial x_j} = F_i. \tag{2.23}$$

We recover Eq. (2.2) with the momentum flux tensor from Eq. (2.20).

2.3 Lattice Boltzmann method

It has been shown numerous times, that the Lattice Boltzmann method can be used to solve several transport equations and in particular the incompressible NSE [44, 45, 46, 47, 48]. To construct our LBM scheme, we need to discretize the Boltzmann equation (Eq. (2.12)) in space, time and microscopic velocity. The discrete distribution function $f(\boldsymbol{c}_\alpha, \boldsymbol{x}, t)$ corresponds to the probability density of fictive particles moving at discrete velocity $\boldsymbol{c}_\alpha$ in lattice direction α at a grid cell with cell center position $\boldsymbol{x}$ at time t. The velocity discretization can generally be represented by a stencil of the form DdQq in d dimensions with q discrete velocities $\alpha \in 0...q-1$ [49]. To recover the NSE one can use the *D1Q3* velocity discretization in one dimension, *D2Q9* in two dimensions or *D3Q15*, *D3Q19*, *D3Q27* in three dimensions (see Fig. 2.1). For our simulations, we will use the *D3Q19* stencil because it provides a good agreement between accuracy and computational efficiency. The space discretization in LBM has to be performed with a uniform, Cartesian grid, so that the discrete lattice direction point to adjacent cells.

The LBM algorithm can be split into two steps - the collision step

$$\tilde{f}_\alpha(\boldsymbol{x}, t) = f_\alpha(\boldsymbol{x}, t) + \Omega_\alpha(\boldsymbol{x}, t), \tag{2.24}$$

with the discrete collision operator Ω_α and the subsequent streaming step

$$f_\alpha(\boldsymbol{x} + \boldsymbol{c}_\alpha \Delta t, t + \Delta t) = \tilde{f}_\alpha(\boldsymbol{x}, t) \tag{2.25}$$

that propagates the updated set of distribution functions to neighboring cells $\boldsymbol{x} + \boldsymbol{c}_\alpha \Delta t$ and advances the simulation by time step Δt. During the collision the distribution functions are relaxed towards the local equilibrium

$$f_\alpha^{\mathrm{eq}}(\boldsymbol{u}, \rho) = w_\alpha \rho \left(1 + \frac{\boldsymbol{c}_\alpha \cdot \boldsymbol{u}}{c_s^2}) + \frac{(\boldsymbol{c}_\alpha \cdot \boldsymbol{u})^2}{2c_s^4} - \frac{\boldsymbol{u} \cdot \boldsymbol{u}}{2c_s^2}\right), \tag{2.26}$$

where w_α are the stencil specific lattice weights (see [49]). More specifically, we use a formulation of the equilibrium distribution, which is suitable for small deviation from the reference pressure $\rho_0 = \rho - \rho'$ and better approximates the incompressible flow equations [50]:

$$f_\alpha^{\mathrm{eq}}(\boldsymbol{u}, \rho) = \omega_\alpha \left(\rho + \rho_0 \left[\frac{\boldsymbol{c}_\alpha \cdot \boldsymbol{u}}{c_s^2}) + \frac{(\boldsymbol{c}_\alpha \cdot \boldsymbol{u})^2}{2c_s^4} - \frac{\boldsymbol{u} \cdot \boldsymbol{u}}{2c_s^2} \right] \right). \tag{2.27}$$

Macroscopic values are recovered as moments of the discrete distribution functions

$$\rho = \sum_\alpha f_\alpha, \quad \boldsymbol{u} = \frac{1}{\rho} \sum_\alpha \boldsymbol{c}_\alpha f_\alpha, \tag{2.28}$$

and the pressure is related to density via equation of state $p = c_s^2 \rho$, according to Sec. 2.1.3.

For our simulations of particle-laden flow around a cylinder, we employ the classic single relaxation time collision operator

$$\Omega_\alpha^{\mathrm{BGK}} = -\frac{\Delta t}{\tau} \left(f_\alpha - f_\alpha^{\mathrm{eq}} \right), \tag{2.29}$$

with the relaxation rate $\omega = 1/\tau$. Furthermore, we set $\Delta x = 1$, $\Delta t = 1$, $\rho_0 = 1$ and $c_s^2 = 1/3$ in lattice units for all upcoming simulations.

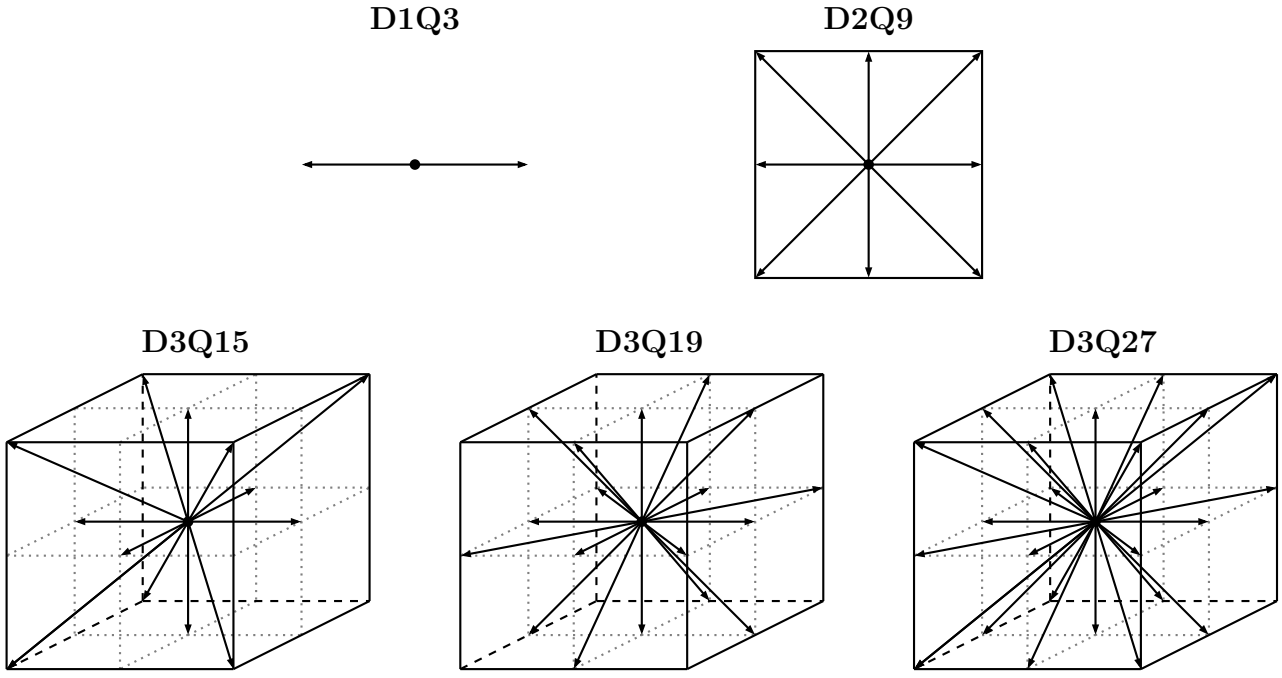

Figure 2.1 – D2Q9, D3Q15, D3Q19 and D3Q27 lattice velocity discretization

2.3.1 Chapman-Enskog Analysis

The so-called Chapman-Enskog analysis [38] is used to obtain macroscopic equations from the Boltzmann equation. It also considers the stress tensor and hence describes the connection between the LB equation and the NSE. In Sec. 2.2 we showed that the momentum conservation equation is recovered for $f = f^{\mathrm{eq}}$. Thus, the stress tensor must be linked to the non-equilibrium part of the distribution function:

$$f^{\mathrm{neq}} = f - f^{\mathrm{eq}}. \tag{2.30}$$

The Chapman-Enskog analysis is essentially a perturbation expansion around the equilibrium distribution for different orders of Kn, see Eq. (2.17). Now we consider terms up to first order of Kn, i.e. $f = f^{\mathrm{eq}} + \epsilon(\mathrm{Kn}) f^{(1)}$, which is sufficient to recover the NSE [51]. The approach is presented using the space and time continuous Boltzmann equation and the BGK collision operator[1]:

$$\partial_t f_\alpha + c_{\alpha i}\partial_i f_\alpha = -\frac{1}{\tau}\left(f_\alpha - f_\alpha^{\mathrm{eq}}\right). \tag{2.31}$$

Applying a Taylor expansion yields

$$\Delta t\left(\partial_t + c_{\alpha i}\partial_i\right) f_\alpha + \frac{\Delta t^2}{2}\left(\partial_t + c_{\alpha i}\partial_i\right)^2 f_\alpha + \mathcal{O}\left(\Delta t^3\right) = -\frac{\Delta t}{\tau} f_\alpha^{\mathrm{neq}}, \tag{2.32}$$

where the third order error terms will be neglected since it is assumed that they are sufficiently small [43]. To get rid of the second order derivative we multiply this equation by $\frac{\Delta t}{2}\left(\partial_t + c_{\alpha i}\partial_i\right)$ and subtract the result from itself while again neglecting the $\mathcal{O}\left(\Delta t^3\right)$ terms leads to

$$\Delta t\left(\partial_t + c_{\alpha i}\partial_i\right) f_\alpha = -\frac{\Delta t}{\tau} f_\alpha^{\mathrm{neq}} + \Delta t\left(\partial_t + c_{\alpha i}\partial_i\right)\frac{\Delta t}{2\tau} f_\alpha^{\mathrm{neq}}. \tag{2.33}$$

The next step is to expand the time derivative into orders of Kn

$$\Delta t\partial_t f_\alpha = \Delta t\left(\epsilon(Kn)\partial_t^{(1)} f_\alpha + \epsilon^2(Kn)\partial_t^{(2)} f_\alpha + ...\right), \tag{2.34}$$

while the space derivative is not expanded:

$$\Delta t c_{\alpha i}\partial_i f_\alpha = \Delta t\left(\epsilon(Kn) c_{\alpha i}\partial_x^{(1)}\right) f_\alpha. \tag{2.35}$$

In perturbation theory this approach is called multiple-scale expansion. It is used to independently deal with the derivative in terms of different orders in Kn, which summed up yield the total derivative. Inserting this expansion along with Eq. (2.17) in Eq. (2.33), we can formulate the equation in terms of the first $\mathcal{O}(\epsilon)$ and second order $\mathcal{O}(\epsilon^2)$ in Kn :

$$\left(\partial_t^{(1)} + c_{\alpha i}\partial_i^{(1)}\right) f_\alpha^{\mathrm{eq}} = -\frac{1}{\tau} f_\alpha^{(1)}, \tag{2.36a}$$

$$\partial_t^{(2)} f_\alpha^{\mathrm{eq}} + \left(\partial_t^{(1)} + c_{\alpha i}\partial_i^{(1)}\right)\left(1 - \frac{\Delta t}{2\tau}\right) f_\alpha^{(1)} = -\frac{1}{\tau} f_\alpha^{(2)}. \tag{2.36b}$$

Multiplying by 1, $c_{\alpha i}$ and summing over α, we obtain the zeroth and first order moments of these equations. The terms of order $\mathcal{O}(\epsilon)$ are the conservation equations, similar to what we have seen in Sec. 2.2:

$$\partial_t^{(1)}\rho + \partial_k^{(1)}\left(\rho u_k\right) = 0, \tag{2.37a}$$

$$\partial_t^{(1)}\left(\rho u_i\right) + \partial_j^{(1)}\Pi_{ij}^{\mathrm{eq}} = 0. \tag{2.37b}$$

[1] It also possible to perform the analysis with a general collision operator, but this will not be covered here.

Repeating the same process for order $\mathcal{O}(\epsilon^2)$ yields the second order correction terms to the Euler equations:

$$\partial_t^{(2)} \rho = 0, \tag{2.38a}$$

$$\partial_t^{(2)} (\rho u_i) + \partial_j^{(1)} \left(1 - \frac{\Delta t}{2\tau}\right) \Pi_{ij}^{(1)} = 0. \tag{2.38b}$$

Now, we can add Eq. (2.37) and (2.38) of corresponding order to find:

$$\left(\epsilon \partial_t^{(1)} + \epsilon^2 \partial_t^{(2)}\right) \rho + \epsilon \partial_k^{(1)} (\rho u_k) = 0, \tag{2.39a}$$

$$\left(\epsilon \partial_t^{(1)} + \epsilon^2 \partial_t^{(2)}\right) (\rho u_i) + \epsilon \partial_j^{(1)} \Pi_{ij}^{\mathrm{eq}} = -\epsilon^2 \partial_j^{(1)} \left(1 - \frac{\Delta t}{2\tau}\right) \Pi_{ij}^{(1)}, \tag{2.39b}$$

which become the mass and momentum conversation equations after reversing the derivative expansion made in Eq. (2.34) and (2.35). Here, the viscous stress tensor takes the form:

$$\sigma'_{ij} = -\left(1 - \frac{\Delta t}{2\tau}\right) \Pi_{ij}^{(1)}. \tag{2.40}$$

It can be shown [43] that the equilibrium moment and the perturbation moment are equal to

$$\Pi_{ij}^{\mathrm{eq}} = \sum_\alpha c_{\alpha i} c_{\alpha j} f_\alpha^{\mathrm{eq}} = \rho u_i u_j + \rho d_s^2 \delta_{ij}, \tag{2.41a}$$

$$\Pi_{ij}^{(1)} = \sum_\alpha c_{\alpha i} c_{\alpha j} f_\alpha^{(1)} = -\rho c_s^2 \tau \left(\partial_j^{(1)} u_i + \partial_i^{(1)} u_j\right) + \tau \partial_k^{(1)} (\rho u_i u_j u_k). \tag{2.41b}$$

The perturbation moment contains an error term of order $\mathcal{O}(u^3)$, which can be neglected for $\mathrm{Ma}^2 = \frac{u^2}{c_s^2} \ll 1$ [52]. As a consequence the LBM is considered to be only weakly compressible, implying it is not suitable for strongly compressible flows [43].

Neglecting the $\mathcal{O}(u^3)$ term, substituting the moments back into Eq. (2.39) and considering the isothermal equation of state leads to

$$\partial_t + \partial_k (\rho u_k) = 0, \tag{2.42a}$$

$$\partial_t (\rho u_i) + \partial_j (\rho u_i u_j) = -\partial_i p + \partial_j (\nu (\partial_j u_i + \partial_i u_j)), \tag{2.42b}$$

with $p = \rho c_s^2$, $\nu = c_s^2 \left(\tau - \frac{\Delta t}{2}\right)$ and $\nu_B = \frac{2}{3}\nu$. Finally, this form is equivalent to the NSE from Eq. (2.3). The Chapman-Enskog expansion can also be performed by projecting onto Hermite polynomials to derive the relation between the Boltzmann equation and the NSE [53].

2.3.2 Multiple-relaxation time model

The BGK operator is the most straightforward approach to model the collision step of the LBM. Unfortunately, it suffers from distinct drawback in terms of accuracy and stability when the viscosity is too small ($\omega \to 2$), too large ($\omega \to 0$) or the velocity magnitudes exceeds the incompressible range ($\|\boldsymbol{u}\| \to c_s$) [54, 55, 56] . Moreover, some flow problems yield viscosity dependent results when using the BGK model in combination with the classic bounce-back boundary condition. The best example for this behavior is the Poiseuille flow, where the simulated wall location varies with the relaxation time τ[57]. To attenuate some of these problems we can introduce a more general way of formulating the collision operator, such that it offers more degrees of freedom.

The multiple-relaxation-times model (MRT) [58] is based on the idea of transforming the populations of the PDF set f to *moment space*

$$\mathrm{m} = \mathbf{M}\mathrm{f}. \tag{2.43}$$

For a DdQq space and velocity discretization the transformation matrix takes the form:

$$\mathbf{M} = \begin{bmatrix} \mathrm{M}_{0,0} & \dots & \mathrm{M}_{0,q-1} \\ \vdots & \ddots & \vdots \\ \mathrm{M}_{q-1,0} & \dots & \mathrm{M}_{q-1,q-1} \end{bmatrix}. \tag{2.44}$$

The obtained moments m_α can be related to particular hydrodynamic terms by selecting the entries of the transformation matrix. Replacing the relaxation rate $\omega = 1/\tau$ in equations 2.24 and 2.25 by the matrix $\mathbf{M}^{-1}\mathbf{S}\mathbf{M}$ yields

$$\begin{aligned} f_\alpha(\boldsymbol{x} + \boldsymbol{c}_\alpha \Delta t, t + \Delta t) &= f_\alpha(\boldsymbol{x}, t) - \mathbf{M}^{-1}\mathbf{S}\mathbf{M}(f_\alpha(\boldsymbol{x}, t) - f_\alpha^{\mathrm{eq}}(\boldsymbol{x}, t)) \\ &= f_\alpha(\boldsymbol{x}, t) - \mathbf{M}^{-1}\mathbf{S}(m_\alpha(\boldsymbol{x}, t) - m_\alpha^{\mathrm{eq}}(\boldsymbol{x}, t)), \end{aligned} \tag{2.45}$$

where $\mathbf{S}$ is a diagonal matrix containing q individual relaxation rates

$$\mathbf{S} = \begin{bmatrix} \omega_0 & 0 & \dots & 0 \\ 0 & \omega_1 & \dots & 0 \\ \vdots & \vdots & \ddots & \vdots \\ 0 & 0 & \dots & \omega_{q-1} \end{bmatrix}. \tag{2.46}$$

When all relaxation rates of $\mathbf{S}$ have the same value we recover the BGK operator, which is why it is also called single-relaxation time (SRT) operator.

There are different ways to determine the entries of the transformation matrix, but we can follow some guideline to produce physical meaningful moments [43]. Setting the first row to $\mathbf{M}_{0,\alpha} = 1$ leads to the zeroth order moment

$$m_0 = \sum_\alpha f_\alpha, \tag{2.47}$$

which corresponds to the density. First order moments are connected to the momentum j by choosing $\mathbf{M}_{l,\alpha} = c_{\alpha,l}$, such that

$$m_l = \sum_\alpha f_\alpha c_{\alpha,l} = \rho u_l = j_l, \tag{2.48}$$

where $l \in \{x, y\}$ is the spatial direction in 2D or $l \in \{x, y, z\}$ in 3D. These zeroth and first order moments represent conserved macroscopic quantities like density or momentum and are therefore not relaxed. The corresponding relaxation rate can be chosen arbitrarily (or set to zero). The remaining vectors $\mathbf{M}_i$, which are the rows of the transformation matrix, can be constructed orthogonal to each other. This is most commonly achieved by applying the Gram-Schmidt process or using Hermite polynomials. For a transformation matrix with non-orthogonal row vectors, there are q distinct relaxation rates that have to be specified. The orthogonalization reduces the number of relaxation rates and ensure that their corresponding moments m_l are uniquely defined and can be relaxed independently. Second order moments are linked to components of the stress tensor, i.e. the shear and bulk viscosity in the Navier-Stokes equations (Eq. (2.6)). Additional moments comprise the energy flux components, energy and energy squared. Third and Fourth order moments are called "non-hydrodynamic" since they do not directly contribute to hydrodynamic terms [44]. They can be chosen freely to improve accuracy and stability for specific flow configurations [58]. Note that the MRT operator allows to adjust the bulk viscosity independently of the shear viscosity, which can dampen unwanted acoustic waves and help stabilizing the simulation [59, 60].

Finally, the MRT collision step is the succession of the following operations: transformation of PDFs and their equilibrium from population space to moment space, the relaxation in moment space and the back transformation to population space. We can write the MRT collision operator as

$$\Omega_\alpha^{\mathrm{MRT}} = -\mathbf{M}^{-1}\mathbf{S}(\mathbf{M}\mathrm{f} - \mathbf{M}\mathrm{f}^{\mathrm{eq}}). \tag{2.49}$$

The consecutive streaming step and the calculation of macroscopic quantities is equivalent to the BGK scheme.

2.3.3 Two-relaxation time model

For certain configurations in the validation chapter Chap. 3, the two relaxation times (TRT) collision operator [57] is utilized. Distribution functions are split into symmetric and antisymmetric parts

$$f_\alpha^{\pm} = \frac{1}{2}\left(f_\alpha \pm f_{\bar{\alpha}}\right), \quad f_\alpha^{\mathrm{eq}\pm} = \frac{1}{2}\left(f_\alpha^{\mathrm{eq}} \pm f_{\bar{\alpha}}^{\mathrm{eq}}\right) \tag{2.50}$$

with $\bar{\alpha}$ denoting the inverse direction, i.e. $\boldsymbol{c}_{\bar{\alpha}} = -\boldsymbol{c}_\alpha$. The TRT collision operator can be written as

$$\Omega_\alpha^{\mathrm{TRT}} = -\omega^+\left(f_\alpha^+ - f_\alpha^{\mathrm{eq}+}\right) - \omega^-\left(f_\alpha^- - f_\alpha^{\mathrm{eq}-}\right) \tag{2.51}$$

and involves the two distinct relaxation times ω^+, ω^-. While τ^+ is determines the kinematic fluid viscosity $\nu = c_s^2\left(\tau^+ - \frac{1}{2}\right)$, the second relaxation time τ^- can be chosen freely to improve accuracy and stability. The TRT collision operator is a specialization of the MRT operator, where all even-order moments are relaxed with ω^+ and all odd-order moments are relaxed with ω^+. The relation between ω^+ and ω^- is the so-called "magic parameter"

$$\Lambda = \left(\frac{1}{2} - \tau^+\right)\left(\frac{1}{2} - \tau^-\right). \tag{2.52}$$

Setting $\Lambda = 3/16$ has been shown to produce the correct velocity profile for the Poiseuille flow when using bounce-back boundary schemes [61], whereas the best stability in a generic simulation can be achieved via $\Lambda = 1/4$ [56]. The TRT operator is particularly beneficial in the low Reynolds number limit, as we will see later in Chap. 3.

2.3.4 Cumulant relaxation model

A recently proposed alternative to the MRT method is the cumulant-based LBM [62]. Instead of relaxing distribution functions in *moment space*, they are transformed into *cumulant space*, where the collision takes place. We want to find a new moment formulation such that the distribution functions can be composed of statistically independent quantities. These quantities C_m represent different physical processes and they successively describe the deviation from a Gaussian equilibrium distribution. Mathematically, the statistical independence is expressed as a factorization of the distribution function f_{ijk} as products of constraints and probabilities F_α that depend on certain physical processes with value C_α:

$$f_{ijk} = \prod_\alpha F_\alpha(C_\alpha). \tag{2.53}$$

Here, we use a different notation of the distribution function, where $i, j, k \in \{-1, 0, 1\}$. To find this new formulation, the distribution functions are rewritten using the continuous microscopic velocity $\boldsymbol{\xi} = (\xi, \upsilon, \zeta)$, the lattice velocity c (which is always 1 for first-neighbor stencils) and the Dirac delta function ($\delta(x) = 1$ when $x = 0$ and $\delta(x) = 0$ when $x \neq 0$):

$$f(\boldsymbol{\xi}) = \sum_{i,j,k} f_{i,j,k}\delta(ic - \xi)\delta(jc - \upsilon)\delta(kc - \zeta). \tag{2.54}$$

Using the two-sided Laplace transformation

$$F(s) = \mathcal{L}[f(x)](s) = \int_{-\infty}^{+\infty} f(x) \cdot e^{-sx}\, dx, \tag{2.55}$$

the distribution functions are transformed into frequency space. We find the Laplace transformed distribution function $F(\boldsymbol{\Xi})$ with wave number $\boldsymbol{\Xi} = \{\Xi, \Upsilon, Z\}$:

$$F(\boldsymbol{\Xi}) = \mathcal{L}[f(\boldsymbol{\xi})] = \int_{-\infty}^{+\infty} f(\boldsymbol{\xi}) \cdot e^{-\boldsymbol{\Xi}\cdot\boldsymbol{\xi}}\, d\boldsymbol{\xi} = \sum_{i,j,k} f_{i,j,k} e^{-\Xi ic} e^{-\Upsilon jc} e^{-Zkc}. \tag{2.56}$$

Unlike $f(\boldsymbol{\xi})$, this new function $F(\boldsymbol{\Xi})$ is indefinitely often differentiable in the wave number $\boldsymbol{\Xi}$. Similar to Eq. (2.53), we can express it as product of yet unknown, statistically independent quantities:

$$F(\boldsymbol{\Xi}) = \prod_\alpha F_\alpha(C_\alpha). \tag{2.57}$$

Applying the logarithm to our function yields the sum

$$\ln(F(\boldsymbol{\Xi})) = \sum_\alpha \ln(F_\alpha(C_\alpha)), \tag{2.58}$$

which can be used in a Taylor expansion:

$$\ln(F(\boldsymbol{\Xi})) = \sum_{o+p+q\geq 0} \frac{1}{o!p!q!} \frac{\partial^{o+p+q}}{\partial\Xi^o\partial\Upsilon^p\partial Z^q} \ln(F(\Xi, \Upsilon, Z))\bigg|_{\Xi=\Upsilon=Z=0} \cdot \Xi^o\Upsilon^p Z^q. \tag{2.59}$$

The evaluated derivatives, which appear as coefficients in this series are now defined as cumulants c_{opq}:

$$c_{opq} := c^{-o-p-q} \frac{\partial^{o+p+q}}{\partial\Xi^o\partial\Upsilon^p\partial Z^q} \ln(F(\Xi, \Upsilon, Z))\bigg|_{\Xi=\Upsilon=Z=0} \tag{2.60}$$

At this point, we introduce a different notation for moments. A *raw moment* (see Sec. 2.3.2) in the continuous form will be defined as

$$m_{opq} = \int \xi^o \cdot \upsilon^p \cdot \zeta^q \cdot f(t, \boldsymbol{x}, \boldsymbol{\xi})\, d\boldsymbol{\xi}, \tag{2.61}$$

where the indices $o, p, q \in \mathbb{N}_0$ indicate the order of the moment in spatial direction x, y, z, respectively. Consequently, the discrete form of raw moments in the new notation is written:

$$m_{opq} = \sum_\alpha c^o_{\alpha,x} \cdot c^p_{\alpha,y} \cdot c^q_{\alpha,z} \cdot f_\alpha = \sum_{ijk} c^o_{ijk,x} \cdot c^p_{ijk,y} \cdot c^q_{ijk,z} \cdot f_{ijk}. \tag{2.62}$$

If we revisit the Taylor series in Eq. (2.59) but without the logarithm (F instead of $\ln(F)$), the relation between cumulants and raw moments becomes apparent:

$$\begin{aligned} \frac{\partial^{o+p+q}}{\partial \Xi^o \partial \Upsilon^p \partial Z^q} F(\Xi, \Upsilon, Z)\bigg|_{\Xi=\Upsilon=Z=0} &= \sum_{ijk} f_{ijk} (-ic)^o e^{-\Xi ic} (-jc)^p e^{-\Upsilon jc} (-kc)^q e^{-Zkc} \bigg|_{\Xi=\Upsilon=Z=0} \\ &= (-c)^{o+p+q} \sum_{ijk} i^o\, j^p\, k^q\, f_{ijk} \\ &= (-c)^{o+p+q} m_{opq}. \end{aligned} \tag{2.63}$$

We can now express the raw moments in similar fashion to the *cumulants*:

$$m_{opq} = (-c)^{-o-p-q} \frac{\partial^{o+p+q}}{\partial \Xi^o \partial \Upsilon^p \partial Z^q} F(\Xi, \Upsilon, Z)\bigg|_{\Xi=\Upsilon=Z=0}. \tag{2.64}$$

Raw moments do not respect Galilean invariance, i.e. the independence of physical processes from the velocity of the frame of reference. Another moment basis are *central moments*, which consider velocity differences to the frame of reference instead of absolute values. In this way, Galilean invariance is restored and the asymptotic error of the term in the Chapman-Enskog analysis, that relates to the velocity dependence of viscosity, is reduced. Similar to raw moments, we define central moments in the continuous form as

$$\kappa_{opq} = \int (\xi - u_x)^o \cdot (\upsilon - u_y)^p \cdot (\zeta - u_z)^q \cdot f(t, \boldsymbol{x}, \boldsymbol{\xi})\, d\boldsymbol{\xi} \tag{2.65}$$

and in the discrete form as

$$\begin{aligned} \kappa_{opq} &= \sum_\alpha (c_{\alpha,x} - u_x)^o \cdot (c_{\alpha,y} - u_y)^p \cdot (c_{\alpha,z} - u_z)^q \cdot f_\alpha \\ &= \sum_{ijk} (c_{ijk,x} - u_x)^o \cdot (c_{ijk,y} - u_y)^p \cdot (c_{ijk,z} - u_z)^q \cdot f_{ijk}. \end{aligned} \tag{2.66}$$

In order to find the Taylor series in frequency space of central moments, we introduce the new distribution function

$$\tilde{f}(\boldsymbol{\xi}) = f(\boldsymbol{\xi} - \boldsymbol{u}) = f(\xi - u_x, \upsilon - u_y, \zeta - u_z), \tag{2.67}$$

to which we apply the two sided Laplace transform:

$$\tilde{F}(\boldsymbol{\Xi}) = \mathcal{L}[\tilde{f}(\boldsymbol{\xi})] = e^{-u\Xi - v\Upsilon - wZ} F(\boldsymbol{\Xi}) = \sum_{ijk} f_{ijk} e^{-\Xi(ic+u_x} e^{-\Upsilon(jc+u_y} e^{-Z(kc+u_z)} \tag{2.68}$$

Performing a Taylor expansion on $\tilde{F}$

$$\tilde{F}(\boldsymbol{\Xi}) = \sum_{o+p+q\geq 0} \frac{1}{o!p!q!} \frac{\partial^{o+p+q}}{\partial \Xi^o \partial \Upsilon^p \partial Z^q} \tilde{F}(\Xi, \Upsilon, Z)\bigg|_{\Xi=\Upsilon=Z=0} \cdot \Xi^o \Upsilon^p \beta Z^q, \tag{2.69}$$

gives us the following coefficients:

$$\frac{\partial^{o+p+q}}{\partial \Xi^o \partial \Upsilon^p \partial Z^q} \tilde{F}(\Xi, \Upsilon, Z)\bigg|_{\Xi=\Upsilon=Z=0} = \sum_{ijk} f_{ijk}[-(ic+u_x)]^o[-(jc+u_y)]^p[-(kc+u_z)]^q. \tag{2.70}$$

When we divide this expression by c^{o+p+q}, we find a definition for the central moments, that is similar to the one for raw moments and cumulants:

$$\begin{aligned} \kappa_{opq} &= (-c)^{-o-p-q} \frac{\partial^{o+p+q}}{\partial \Xi^o \partial \Upsilon^p \partial Z^q} \tilde{F}(\Xi, \Upsilon, Z)\bigg|_{\Xi=\Upsilon=Z=0} \\ &= \sum_{ijk} f_{ijk} \left(i + \frac{u_x}{c}\right)^o \left(j + \frac{u_y}{c}\right)^p \left(k + \frac{u_z}{c}\right)^q \end{aligned} \tag{2.71}$$

Additional information on the implementation of the cumulant method can be found in [63]. In *lbmpy* cumulant relaxation is implemented by transforming distribution functions from population space into central moment space and then into cumulant space, where the collision takes place. We can write a central moment generating function $K(\boldsymbol{\Xi})$, that transforms populations to central moments:

$$K(\boldsymbol{\Xi}) = \exp(-\boldsymbol{\Xi} \cdot \boldsymbol{u}) \sum_{c_\alpha} f_\alpha \exp(c_\alpha \cdot \boldsymbol{\Xi}) \tag{2.72}$$

Subsequently, central moments are transformed into cumulants via the cumulant generating function:

$$C(\boldsymbol{\Xi}) = \boldsymbol{\Xi} \cdot \boldsymbol{u} + \ln(K(\boldsymbol{\Xi})). \tag{2.73}$$

Differentiating and evaluating this function at zero yields the cumulants, which are used during the collision step. Afterwards, cumulants have to be transformed back to central moment space and then to population space. Finding and evaluating the derivative of the moment generating functions can be a tedious task. Fortunately, there is an easier method to construct central moments from populations, called fast central-moment-transformation:

$$\begin{aligned} \kappa_{ij|q} &= \sum_k (c_{ijk,z} - u_z)^q \cdot f_{ijk} \\ \kappa_{i|pq} &= \sum_j (c_{ijk,y} - u_y)^q \cdot \kappa_{ij|q} \\ \kappa_{opq} &= \sum_k (c_{ijk,x} - u_x)^q \cdot \kappa_{i|pq} \end{aligned} \tag{2.74}$$

It can be shown that cumulants up to order three are almost identical to central moments:

$$\begin{aligned} \rho c_{000} &= \kappa_{000}, \\ \rho c_{100} &= \kappa_{100}, \\ \rho c_{110} &= \kappa_{110}, \\ \rho c_{111} &= \kappa_{111}, \\ \rho c_{210} &= \kappa_{210}, \end{aligned} \tag{2.75}$$

and so on. Third and fourth order cumulants are computed via:

$$\begin{aligned}
\rho c_{211} =& \kappa_{211} - (\kappa_{200}\kappa_{011} + 2\kappa_{110}\kappa_{101})/\rho, \\
\rho c_{220} =& \kappa_{220} - (\kappa_{200}\kappa_{020} + 2\kappa_{110}^2)/\rho, \\
\rho c_{122} =& \kappa_{122} - (\kappa_{002}\kappa_{120} + \kappa_{020}\kappa_{102} + 4\kappa_{011}\kappa_{111} + 2(\kappa_{101}\kappa_{021} + \kappa_{110}\kappa_{012}))/\rho, \\
\rho c_{222} =& \kappa_{222} - (4\kappa_{111}^2 + \kappa_{200}\kappa_{022} + \kappa_{020}\kappa_{202} + \kappa_{002}\kappa_{220} + 4(\kappa_{011}\kappa_{211} + \kappa_{101}\kappa_{121} + \kappa_{110}\kappa_{112}) \\
&+ 2(\kappa_{120}\kappa_{102} + \kappa_{210}\kappa_{012} + \kappa_{201}\kappa_{021}))/\rho \\
&+ (16\kappa_{110}\kappa_{101}\kappa_{011} + 4(\kappa_{101}^2\kappa_{020} + \kappa_{011}^2\kappa_{200} + \kappa_{110}^2\kappa_{002}) + 2\kappa_{200}\kappa_{020}\kappa_{002})/\rho^2,
\end{aligned} \tag{2.76}$$

and so forth by permuting indices. The back transformation, as well as the construction of equilibrium values can be found in [62]. External forces are applied symmetrically before and after collision. Half the force is added to central moments before transformation to cumulants and the other half is added after transforming cumulants back to central moments. In this way, the first order central moments entering the collision is zero $\kappa_{100}^S = 0$.

Some properties of the cumulant method are preferential compared to the standard MRT. Cumulants are mutually independent and be relaxed with individual relaxation rates, providing more (real) degrees of freedom to adjust stability and accuracy. By design, cumulants are Galilean invariant, i.e. independent of the reference frame. The equilibrium value of cumulants is zero, except for conserved quantities like density and momentum. It should be noted, that the transformation from populations to cumulants is non-linear.

2.3.5 Smagorinsky subgrid scale model

In many practical engineering applications it is not possible to numerically resolve all flow scales via DNS because of the high computational cost. A subgrid scale (SGS) model reduces the cost by applying a low-pass filter to the NSE. It is an essential ingredient in most CFD codes and it can be introduced in LBM [64]. While large turbulent structures are computed, the small scale flow features will be modeled instead. This idea is represented in Fig. 2.2, where k_Δ denotes the filter cutoff frequency. It is typically chosen, such that subgrid scales are not resolved and must be modeled.

A spatial filtering operation can be written as [65]

$$\overline{\phi}(\boldsymbol{x}) = \int_{-\infty}^{+\infty} \phi(\boldsymbol{\psi})\, G(\boldsymbol{x} - \boldsymbol{\psi})\, d^3\boldsymbol{\psi}, \tag{2.77}$$

where G is the filter function and ϕ can be any physical quantity. Applying the filter operation to the incompressible NSE yields the filtered continuity and momentum equations

$$\partial_i \overline{u}_i = 0, \tag{2.78a}$$

$$\partial_t \overline{u}_i + \overline{u}_j \partial_j \overline{u}_i = -\partial_i \overline{p} - \partial_j \tau_{ij} + \partial_j \left(\nu \left(\partial_j \overline{u}_i + \partial_i \overline{u}_j\right)\right). \tag{2.78b}$$

The Reynolds stress tensor

$$\tau_{ij} = \overline{u_i u_j} - \overline{u}_i \overline{u}_j \tag{2.79}$$

involves influence from unresolved scales and thus is the part which needs to be modeled. The Smagorinsky model [66] relates the anisotropic stress tensor to the strain rate tensor

$$\tau_{ij} - \frac{\delta_{ij}}{3}\tau_{kk} = -2\nu_t \overline{S}_{ij} = -2C_S\Delta^2 |\overline{S}| \overline{S}_{ij}, \tag{2.80}$$

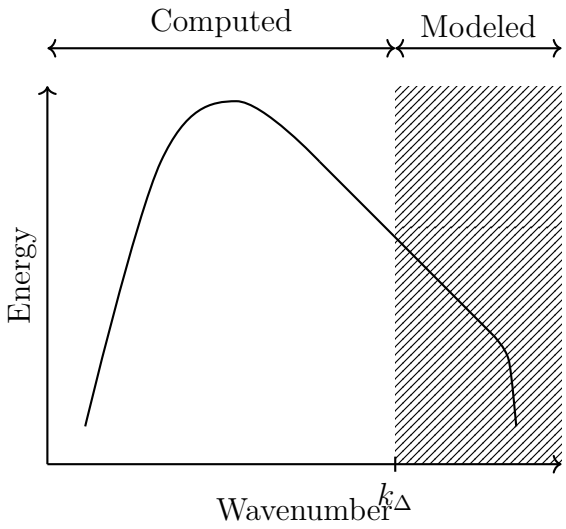

Figure 2.2 – Energy spectrum in SGS turbulence modeling

where C_S denotes the Smagorinsky constant, $\Delta \sim 1/k_\Delta$ is the filter cutoff length and $|\overline{S}| = \sqrt{2\overline{S}_{ij}\overline{S}_{ij}}$ is the Frobenius norm of the strain rate tensor. The turbulent viscosity ν_t is introduced to account for the additional energy dissipation of vortices at small scale.

Strictly speaking, there is no SGS model in LBM for turbulent flows. In LB methods, the strain rate tensor can be computed locally as

$$\overline{S}_{ij} = \frac{1}{2}(\partial_i \overline{u}_j + \partial_j \overline{u}_i) = -\frac{3\omega}{2\rho}\overline{\Pi}^{\text{neq}}_{ij}, \tag{2.81}$$

where Π^{neq}_{ij} is the second order moment tensor of the non-equilibrium part defined by

$$\overline{\Pi}^{\text{neq}}_{ij} = \sum_\alpha c_{\alpha i} c_{\alpha j} \left(\overline{f}_\alpha - \overline{f}^{\text{eq}}_\alpha\right). \tag{2.82}$$

The additional subgrid viscosity depends on the local shear rate such that

$$\nu_t = (C_S\Delta)^2|\overline{S}|, \tag{2.83}$$

where the filter width is set to the lattice grid size $\Delta = 1$ and C_S should be chosen in the range of 0.1 to 0.2. Finally, the turbulent viscosity is added to the fluid viscosity ν_0 in every grid cell to obtain the total viscosity

$$\nu_{total} = \nu_0 + \nu_t, \tag{2.84}$$

which is now used for the LB collision step. We use this turbulence model in combination with the BGK collision operator, but it can also be used with other collision schemes like MRT or cumulants.

In LBM like in classical LES codes, the necessity of using a SGS model such as Smagorinsky remains a controversial issue since any numerical dissipation can play a similar role. This will be tested in Chap. 4.

2.3.6 Entropic stabilization

The entropic relaxation scheme is an extension to the classic LBM, which is particularly useful for turbulent, high Reynolds number flows. The physically motivated idea is that the entropy of a system must increase during a collision process. By maximizing the entropy of the post-collision state, the numerical scheme is stabilized without explicitly adding artificial dissipation. Here, we do not refer to the entropic Lattice-Boltzmann method (ELBM) but rather to its successor - the family of KBC models developed by Karlin, Bösch and Chikatamarla [67]. Neither of the two models feature an explicit turbulence model, but they adapt the relaxation parameter locally according to some entropy condition. While the ELBM adaptation affects the fluid viscosity, the KBC model only modifies higher order moments, which have no direct influence on hydrodynamic terms.

In order to avoid introducing mirror states, we follow the notation of *lbmpy*. Let us split the populations in the PDF set according to their moments, such that

$$f_\alpha = k_\alpha + s_\alpha + h_\alpha, \tag{2.85}$$

where k_α is the kinematic part, s_α is the shear part and h_α is the higher-order part. The kinematic moments are conserved quantities (which are not relaxed), the shear moments are connected to the stress tensor of the NSE and the remaining moments are contained within the higher-order part. Consequently, the post-collision state of the LB scheme can be written as

$$\tilde{f}_\alpha = f_\alpha - \omega_s \Delta s_\alpha - \omega_h \Delta h_\alpha, \tag{2.86}$$

with the shear relaxation rate ω_s, the higher-order relaxation rate ω_h and the deviations from equilibrium $\Delta s_\alpha = s_\alpha - s_\alpha^{\mathrm{eq}}$ and $\Delta h_\alpha = h_\alpha - h_\alpha^{\mathrm{eq}}$. The main idea of the KBC model is to maximize the entropy of the post-collision state of the LB scheme

$$S(\tilde{f}) = -\sum_\alpha \tilde{f}_\alpha \ln\left(\frac{\tilde{f}_\alpha}{f_\alpha^{\mathrm{eq}}}\right). \tag{2.87}$$

in every cell by adjusting ω_h, while keeping ω_s constant. Hence, we need to take the first derivative of the entropy with respect to ω_h and set it to zero:

$$\sum_\alpha \Delta h_\alpha \left(\ln\left(\frac{\tilde{f}_\alpha}{f_\alpha^{\mathrm{eq}}}\right) + 1\right) = 0 \tag{2.88}$$

Eq. (2.88) could be solved by applying Newton's method, which would be computationally costly. Instead the logarithm is approximated by a first order Taylor expansion around 1 ($\ln(x) \approx x - 1$), since $\tilde{f}$ is expected to be close to f^{eq}. The simplified condition for the point of maximum entropy is

$$\sum_\alpha \Delta h \frac{\tilde{f}_\alpha}{f_\alpha^{\mathrm{eq}}} = 0. \tag{2.89}$$

Introducing the entropic scalar product

$$\langle X|Y\rangle = \sum_\alpha \frac{X_\alpha Y_\alpha}{f_\alpha^{\mathrm{eq}}} \tag{2.90}$$

allows us to write the optimal relaxation rate for higher-order moments as

$$\omega_h^* = 1 + (1 - \omega_s)\frac{\langle \Delta s|\Delta h\rangle}{\langle \Delta h|\Delta h\rangle}. \tag{2.91}$$

This formulation maximizes the entropy in every cell in a computational efficient manner without the need for an iteration process.

As discussed in [68], there are several definitions s_α leading to the different variants of the KBC model. Tab. 2.1 gives an example of the moments and their corresponding equilibrium values and relaxation rates of an orthogonalized D2Q9 MRT model. The zeroth and first order moments, i.e. the first three entries in the table, relate to conserved quantities and are thus not relaxed. Second order moments are split into two groups: the moments responsible for shear viscosity and the moments responsible for bulk viscosity and they can be relaxed individually with $\omega^{2,s}$ and $\omega^{2,b}$, respectively. Third and Fourth order moments are relaxed with ω^3 and ω^4, respectively. The shear part s_α of the entropic formulation can be composed of the moments corresponding to the shear viscosity plus an arbitrary combination of the moments related to the bulk viscosity, third and fourth order moments. The remaining moments are attributed to the higher-order part h_α.

For our simulations of turbulent flows in Sec. 3.8 we configure the relaxation model such that shear and bulk moments compose the shear part, i.e. $\omega^{2,s}, \omega^{2,b} = \omega_s$, whereas third and fourth order moments compose the higher-order part, i.e. $\omega^3, \omega^4 = \omega_h^*$.

Moment	Equilibrium value	Relaxation rate
$\sum_\alpha f_\alpha$	ρ	0
$\sum_\alpha f_\alpha c_{\alpha,x}$	ρu_x	0
$\sum_\alpha f_\alpha c_{\alpha,y}$	ρu_y	0
$\sum_\alpha f_\alpha c_{\alpha,x} c_{\alpha,x} - f_\alpha c_{\alpha 1} c_{\alpha 1}$	$\rho u_x^2 - \rho u_y^2$	$\omega^{2,s}$
$\sum_\alpha f_\alpha c_{\alpha,x} c_{\alpha,y}$	$\rho u_x u_y$	$\omega^{2,s}$
$\sum_\alpha 3 f_\alpha c_{\alpha,x} c_{\alpha,x} + 3 f_\alpha c_{\alpha,y} c_{\alpha,y} - 2 f_\alpha$	$3\rho u_x^2 + 3\rho u_y^2$	$\omega^{2,b}$
$\sum_\alpha 3 f_\alpha c_{\alpha,x} c_{\alpha,x} c_{\alpha,y} - f_\alpha c_{\alpha,y}$	0	ω^3
$\sum_\alpha 3 f_\alpha c_{\alpha,x} c_{\alpha,y} c_{\alpha,y} - f_\alpha c_{\alpha,x}$	0	ω^3
$\sum_\alpha 9 f_\alpha c_{\alpha,x} c_{\alpha,x} c_{\alpha,y} c_{\alpha,y} - 3 f_\alpha c_{\alpha,x} c_{\alpha,x} - 3 f_\alpha c_{\alpha,y} c_{\alpha,y} + f_\alpha$	0	ω^4

Table 2.1 – Exemplary relaxation scheme of an orthogonalized D2Q9 MRT model.

2.3.7 Inclusion of external forces

When simulating flows that are driven by a pressure gradient, such as flows in a periodic channel (see Sec. 3.6 and Sec. 3.8) , an external force term F_α has to be added to Eq. (2.24)

$$\tilde{f}_\alpha(\boldsymbol{x}, t) = f_\alpha(\boldsymbol{x}, t) + \Omega_\alpha(\boldsymbol{x}, t) + F_\alpha. \tag{2.92}$$

This force term has to satisfy the condition that its first order moment

$$\sum_\alpha \boldsymbol{c}_\alpha F_\alpha = \rho \boldsymbol{a} \tag{2.93}$$

is equal to the product of density and external acceleration $\boldsymbol{a}$, acting on the fluid [69]. The simplest way of constructing the force term is

$$F_\alpha = \frac{w_\alpha}{c_s^2} \rho \boldsymbol{c}_\alpha \cdot \boldsymbol{a}, \tag{2.94}$$

which is only suitable for strictly incompressible flows with constant external acceleration. This is because the second order moment

$$\sum_\alpha c_{\alpha,i} c_{\alpha,j} F_\alpha = 0 \tag{2.95}$$

is equal to zero for the form term in Eq. (2.94). Moreover, the calculation of the macroscopic velocity has to be adjusted by adding the force term, such that

$$\boldsymbol{u}^* = \frac{1}{\rho} \left(\sum_\alpha \boldsymbol{c}_\alpha f_\alpha + \frac{\Delta t}{2} \sum_\alpha F_\alpha \right). \tag{2.96}$$

Luo force model

Luo [69, 70] proposed an advanced approach of specifying the force term:

$$F_\alpha = w_\alpha \rho \left(\frac{\boldsymbol{c}_\alpha - \boldsymbol{u}}{c_s^2} + \frac{\boldsymbol{c}_\alpha \cdot \boldsymbol{u}}{c_s^4} \boldsymbol{c}_\alpha \right) \cdot \boldsymbol{a}. \tag{2.97}$$

It can be used for weakly compressible flows since the second order moment is nonzero, i.e.

$$\sum_\alpha c_{\alpha,i} c_{\alpha,j} F_\alpha = \rho (a_i u_j + a_j u_i). \tag{2.98}$$

The macroscopic velocity shift is equivalent to Eq. (2.96).

Guo force model

In addition to adjusting the macroscopic velocity, the equilibrium velocity is modified (in the same manner) to obtain the force term

$$F_\alpha = \left(1 - \frac{\omega}{2}\right) w_\alpha \rho \left(\frac{\boldsymbol{c}_\alpha - \boldsymbol{u}}{c_s^2} + \frac{\boldsymbol{c}_\alpha \cdot \boldsymbol{u}}{c_s^4} \boldsymbol{c}_\alpha \right) \cdot \boldsymbol{a} \tag{2.99}$$

proposed by Guo [71]. The second order moment of this force term is nonzero.

Further force models have been suggested by Schiller [72] or Buick [73].

2.3.8 Boundary conditions

No-slip

The no-slip condition is required to impose zero normal and tangential velocity at a boundary. For LB schemes, it is also called *bounce-back* because populations are reflected back in the opposite incoming direction. The missing populations can be obtained by applying

$$f_{\bar{\alpha}}(\boldsymbol{x}) = \tilde{f}_{\alpha}(\boldsymbol{x}) \tag{2.100}$$

after the collision and before the streaming step. Fig. 2.3 offers a visual representation of the Eq. (2.100). It is generally first order accurate in space [74] and viscosity depended when used in combination with the BGK collision operator. For straight walls, where the exact wall location is half-way ($\Delta x/2$) outside the boundary node it is second order accurate.

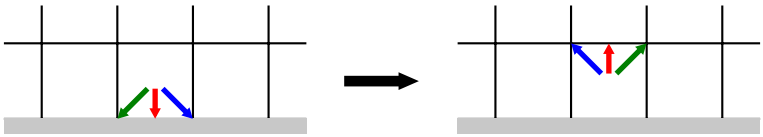

Figure 2.3 – Treatment of PDFs during no slip boundary handling

Free-slip

A free-slip boundary is achieved by the reflection scheme illustrated in Fig. 2.4. It enforces zero normal velocity while preserving the tangential velocity component. Located half-way outside the boundary node along a straight wall it is second order accurate, otherwise first-order.

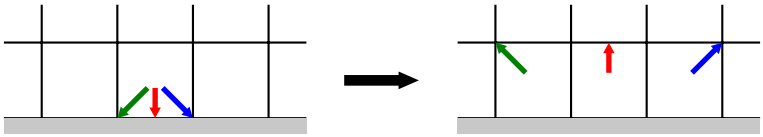

Figure 2.4 – Treatment of PDFs during free-slip boundary handling

Velocity bounce-back

This boundary condition was introduced by Ladd [75] and is used to prescribe a velocity value at the boundary. It is similar to the bounce-back scheme but has an additional term, that is responsible for the momentum transfer from the boundary to the fluid:

$$f_{\bar{\alpha}}(\boldsymbol{x}) = \tilde{f}_{\alpha}(\boldsymbol{x}) - 2\rho\frac{w_{\alpha}}{c_s^2}\boldsymbol{c}_{\alpha} \cdot \boldsymbol{u}_b. \tag{2.101}$$

This additional term includes the velocity at the boundary $\boldsymbol{u}_b$ and is constructed such that the boundary behaves like a bounce-back condition when the fluid velocity equals the boundary velocity.

Constant pressure boundary

To impose the pressure at an outflow type boundary condition missing populations are obtained by applying the *anti-bounce-back* method [61] and adding an equilibrium term for the pressure as follows:

$$f_{\bar{\alpha}}(\boldsymbol{x}) = -\tilde{f}_{\alpha}(\boldsymbol{x}) + 2w_{\alpha}\rho\left(1 - \frac{\boldsymbol{u}\cdot\boldsymbol{u}}{2c_s^2} + \frac{(\boldsymbol{c}_{\alpha}\cdot\boldsymbol{u})^2}{2c_s^4}\right). \tag{2.102}$$

Similar to the *bounce-back*, this pressure condition is second-order accurate if the boundary is considered half-way outside the boundary. Second-order error terms can be removed by introducing an additional correction term, see [57].

Periodic

Periodic boundary conditions are used to approximate an infinitely large domain in the given direction. Two opposite ends of the domain are connected with each via communication other as if they were neighboring patches. Populations of the PDF, that are directed towards the boundary are streamed to the corresponding other side of the domain, as shown in Fig. 2.5.

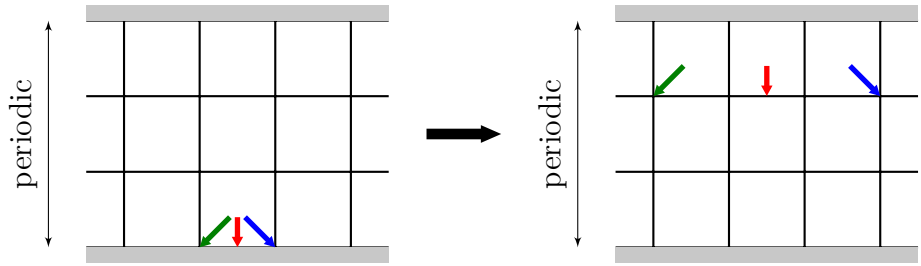

Figure 2.5 – Treatment of PDFs during periodic boundary handling

2.4 Moving obstacle boundary conditions

Due to the kinetic nature of the LBM, momentum exchange between fluid and solid phases can be computed in a straightforward manner. The underlying idea is that mass components streaming into the boundary causes a momentum influx, while mass components streaming out of the boundary causes a momentum outflux. At the same time a no-slip condition has to be satisfied at the solid surface. The interface coupling is based on [75] and has been improved by [76]. In our configuration, solid particles, as well as the stationary cylinder, are explicitly mapped into the domain as solid obstacles. The boundary treatment is executed for every discrete direction or link between fluid and solid nodes. The missing population $f_{\bar{\alpha}}$ of the distribution function set at the moving fluid-solid interface is derived from a bounce back (BB) scheme

$$f_{\bar{\alpha}}(\boldsymbol{x}, t+\Delta t) = \tilde{f}_{\alpha}(\boldsymbol{x}, t) - \varphi\frac{w_{\alpha}}{c_s^2}\rho_0\boldsymbol{u}(\boldsymbol{x}_b, t)\cdot\boldsymbol{c}_{\alpha}, \tag{2.103}$$

which is extended by a term that takes the velocity $\boldsymbol{u}(\boldsymbol{x}_b, t)$ on the exact boundary location $\boldsymbol{x}_b = \boldsymbol{x} + \delta_{\alpha}\boldsymbol{c}_{\alpha}\Delta t$ into account. The variable δ_q is the relative distance between the cell center and the exact surface position. To achieve second order accuracy, we use the central linear interpolation (CLI) [57] given by

$$f_{\bar{\alpha}}(\boldsymbol{x}, t+\Delta t) = \kappa_1\tilde{f}_{\alpha}(\boldsymbol{x}, t) + \kappa_0\tilde{f}_{\alpha}(\boldsymbol{x} - \boldsymbol{c}_{\alpha}\Delta t, t) + \kappa_{-1}\tilde{f}_{\bar{\alpha}}(\boldsymbol{x}, t) - \varphi\tfrac{w_{\alpha}}{c_s^2}\rho_0\boldsymbol{u}(\boldsymbol{x}_b, t)\cdot\boldsymbol{c}_{\alpha}, \tag{2.104}$$

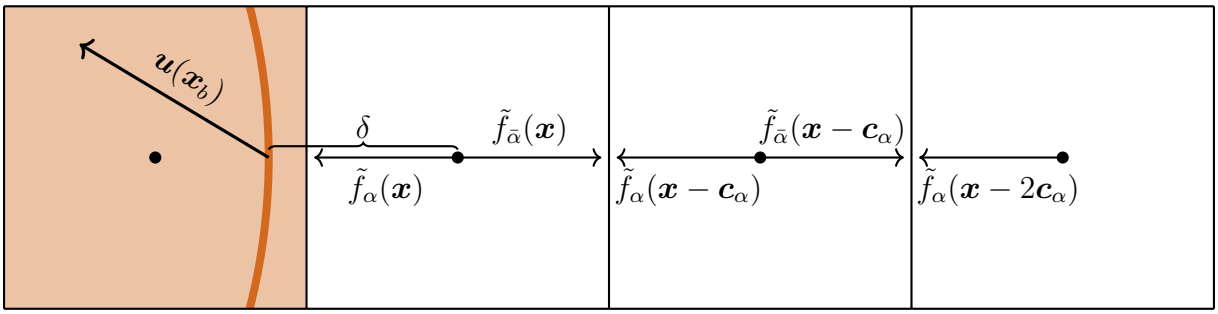

Figure 2.6 – Distribution functions used in the fluid-solid coupling scheme. Fluid cells are white, solid cells are colored and particle surface is represented by the arc.

with the coefficients κ_1, κ_0, κ_{-1} and φ found in Tab. 2.2. This interpolation scheme uses subgrid information to smoothen the staircase approximation of the particle shape. It also involves the population at the node $\boldsymbol{x}-\boldsymbol{c}_\alpha\Delta t$, which is located one cell further away from the boundary. To achieve even higher accuracy the multi-reflection (MR) scheme can be employed:

$$\begin{aligned} f_{\bar{\alpha}}(\boldsymbol{x},t+\Delta t) =& \kappa_1\tilde{f}_\alpha(\boldsymbol{x},t)+\kappa_0\tilde{f}_\alpha(\boldsymbol{x}-\boldsymbol{c}_\alpha\Delta t,t)+\kappa_{-1}\tilde{f}_\alpha(\boldsymbol{x}-2\boldsymbol{c}_\alpha\Delta t,t) \\ &+\bar{\kappa}{-}1\tilde{f}_{\bar{\alpha}}(\boldsymbol{x},t)+\bar{\kappa}_{-2}\tilde{f}_{\bar{\alpha}}(\boldsymbol{x}-\boldsymbol{c}_\alpha\Delta t,t) \\ &-\varphi\tfrac{w_\alpha}{c_s^2}\rho_0\boldsymbol{u}(\boldsymbol{x}_b,t)\cdot\boldsymbol{c}_\alpha+f_\alpha^{pc}. \end{aligned} \tag{2.105}$$

The coefficients are given in Tab. 2.2 and the correction term f_α^{pc}, which is necessary to eliminate the second-order error, is available from [57]. This quadratic interpolation incorporates the PDF populations depicted in Fig. 2.6. BB, CLI and MR schemes are designed in such a way, that they produce viscosity independent solutions in porous media and Poiseuille flows when used in combination with the TRT collision operator. A detailed comparison of the accuracy of presented algorithms was done by Rettinger [26]. We will apply the CLI boundary condition during the following simulations as a compromise between accuracy and computational efficiency.

	κ_0	κ_{-1}	$\bar{\kappa}_{-1}$	$\bar{\kappa}_{-2}$	φ
BB	0	0	0	0	2
CLI	$\frac{1-2\delta_\alpha}{1+2\delta_\alpha}$	0	$-\kappa_0$	0	$\frac{4}{1+2\delta_\alpha}$
MR	$\frac{1-2\delta_\alpha-2\delta_\alpha^2}{(1-\delta_\alpha)^2}$	$\frac{\delta_\alpha^2}{(1-\delta_\alpha)^2}$	$-\kappa_0$	$-\kappa_{-1}$	$\frac{4}{(1+2\delta_\alpha)^2}$

Table 2.2 – Coefficients for the the bounce-back (BB), central linear interpolation (CLI) and multi-reflection (MR) schemes. The last coefficient is always $\kappa_1 = 1-\kappa_0-\kappa_{-1}-\bar{\kappa}_{-1}-\bar{\kappa}_{-2}$.

The interaction force is the difference between instreaming and outstreaming mass components multiplied with the relative velocity between fluid and solid phases. It is calculated as

$$\boldsymbol{F}^{\alpha_{\mathrm{f-s}}}(\boldsymbol{x}_b,t)=\tfrac{(\Delta x)^3}{\Delta t}\left[(\boldsymbol{c}_{\alpha_{\mathrm{f-s}}}-\boldsymbol{u}(\boldsymbol{x}_b,t))\tilde{f}_{\alpha_{\mathrm{f-s}}}(\boldsymbol{x},t)-(\boldsymbol{c}_{\bar{\alpha}_{\mathrm{f-s}}}-\boldsymbol{u}(\boldsymbol{x}_b,t))f_{\bar{\alpha}_{\mathrm{f-s}}}(\boldsymbol{x},t+\Delta t)\right] \tag{2.106}$$

for every direction $\alpha_{\mathrm{f-s}}$ that links a fluid with a solid cell [75, 77]. Summing up the contributions over all fluid-solid links gives us the total force

$$\boldsymbol{F}_{\mathrm{f-s}}(t)=\sum_{\boldsymbol{x}_b}\sum_{\alpha_{\mathrm{f-s}}}\boldsymbol{F}^{\alpha_{\mathrm{f-s}}}(\boldsymbol{x}_b,t) \tag{2.107}$$

and torque

$$\boldsymbol{T}_{\mathrm{f-s}}(t) = \sum_{\boldsymbol{x}_b} \sum_{\alpha_{\mathrm{f-s}}} (\boldsymbol{x}_b - \boldsymbol{X}_p) \times \boldsymbol{F}^{\alpha_{\mathrm{f-s}}}(\boldsymbol{x}_b, t), \tag{2.108}$$

acting on an obstacle with its center at position $\boldsymbol{X}_p$. This implementation is based on the previous work of Götz [23] and Bartuschat [25]. There are alternative approaches available, i.e. different formulations of the boundary condition and algorithms for reconstructing missing distribution function of empty cells [78, 79].

2.4.1 PDF refilling schemes

Due to the motion of a particle through the static computational grid, the domain mapping has to be adjusted. When a cell that was filled with fluid in the previous time step is now occupied by a particle, the cell status is simply changed to solid. In the case of a solid cell turning into a fluid cell, the missing distribution functions need to be refilled. The simplest approach to reconstruct missing PDFs of a newly created fluid cell $\boldsymbol{x}_{\mathrm{new}}$ is to set them equal to the equilibrium distribution

$$f_\alpha(\boldsymbol{x}_{\mathrm{new}}) = f_\alpha^{\mathrm{eq}}(\bar{\rho}_f, \boldsymbol{u}_b) \tag{2.109}$$

using the local boundary velocity $\boldsymbol{u}_b$ and an average density $\bar{\rho}_f$ of available adjacent fluid cells [80].

This scheme only considers the equilibrium part of the unknown PDF. A non-equilibrium contribution can be included by adding the non-equilibrium part [81] of the PDF from the cell in normal direction to the solid surface

$$f_\alpha(\boldsymbol{x}_{\mathrm{new}}) = f_\alpha^{\mathrm{eq}}(\bar{\rho}_f, \boldsymbol{u}_b) + f_\alpha^{\mathrm{neq}}(\boldsymbol{x}_{\mathrm{new}} + \boldsymbol{c}_{\alpha_n}\Delta t). \tag{2.110}$$

The approximate normal direction $\boldsymbol{c}_{\alpha_n}$ is the lattice direction that is found by maximizing $\boldsymbol{n}\cdot\boldsymbol{c}_\alpha$, with $\boldsymbol{n}$ being the particle's surface normal.

Another refilling strategy is to perform a linear extrapolation [82]

$$f_\alpha(\boldsymbol{x}_{\mathrm{new}}) = 2f_\alpha(\boldsymbol{x}_{\mathrm{new}} + \boldsymbol{c}_{\alpha_n}\Delta t) - f_\alpha(\boldsymbol{x}_{\mathrm{new}} + 2\boldsymbol{c}_{\alpha_n}\Delta t) \tag{2.111}$$

if two fluid cells in normal direction are available or a quadratic extrapolation

$$f_\alpha(\boldsymbol{x}_{\mathrm{new}}) = 3f_\alpha(\boldsymbol{x}_{\mathrm{new}} + \boldsymbol{c}_{\alpha_n}\Delta t) - 3f_\alpha(\boldsymbol{x}_{\mathrm{new}} + 2\boldsymbol{c}_{\alpha_n}\Delta t) + f_\alpha(\boldsymbol{x}_{\mathrm{new}} + 3\boldsymbol{c}_{\alpha_n}\Delta t), \tag{2.112}$$

if three fluid cells are available. None of the above formulations strictly respect the no-slip boundary condition at the newly created fluid node. By making use of the MRT formulation, the velocity can be constrained to the wall velocity without modifying moments that contribute to different physical quantities like pressure and shear stress [83]. The moments $\boldsymbol{m}$ are obtained by applying the transfer matrix $\boldsymbol{M}$ to the previously extrapolated PDF set $\hat{f}$:

$$\mathrm{m}(\boldsymbol{x}_{\mathrm{new}}) = \mathbf{M}\hat{f}(\boldsymbol{x}_{\mathrm{new}}). \tag{2.113}$$

In moment space the momentum

$$\boldsymbol{j} = \rho_0 \boldsymbol{u}_b \tag{2.114}$$

is constrained to enforce the no-slip condition at the particle boundary. Applying the inverse transfer to the adjusted moments m^* gives the new set of PDFs

$$f_\alpha(\boldsymbol{x}_{\mathrm{new}}) = \mathbf{M}^{-1}\mathrm{m}^*(\boldsymbol{x}_{\mathrm{new}}). \tag{2.115}$$

This method of constraining the fluid velocity to the local particle velocity in moment space has been shown to reduce fluctuations in the fluid-solid interaction [78]. If there are insufficient fluid nodes available in normal direction, the previous refill schemes can serve as a fallback solution.

2.5 Granular collision modeling

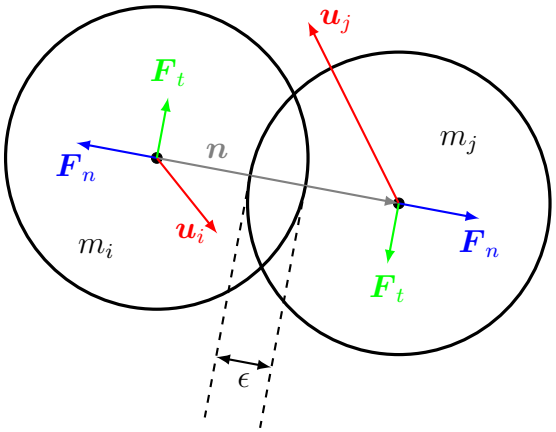

Figure 2.7 – Scheme showing two colliding spherical particles

Whenever an overlap between particles is detected, a collision response needs to be modeled. A well established method for resolving collisions is the discrete element method (DEM) [84, 85]. There are many variants of the DEM with complex physics modeling. Here, a so-called soft-sphere approach is used to compute the repulsive force for two spheres or a sphere and a wall. The penetration distance ϵ should be kept small in comparison to the particle diameter to ensure numerical stability and physical relevance [86]. The normal contact force

$$F_c^n = \max(0, k_n \epsilon - \gamma_n u_n) \tag{2.116}$$

is modeled based on a linear spring-dashpot system with normal spring stiffness k_n, normal damping coefficient γ_n and relative velocity in normal direction $u_n = \frac{\boldsymbol{n}}{\|\boldsymbol{n}\|} \cdot (\boldsymbol{u}_i - \boldsymbol{u}_j)$. Here, $\boldsymbol{u}_i$ and $\boldsymbol{u}_j$ correspond to the velocity of particle i and particle j, respectively. F_c^n is restricted to positive values to avoid attractive forces and added to all interacting objects through positive summation. The computation of friction laws is specific for static and dynamic friction. Coulomb's friction law $F_c^t = \mu F_c^n$ is only applicable for two particles in contact, moving with a substantial relative tangential velocity. In the model of Haff and Werner [87] the force component F_c^t at low tangential velocity is interpreted as a shear damping model

$$F_c^t = -\min(\mu F_c^n, \gamma_t u_t) \tag{2.117}$$

with μ denoting the Coulomb friction parameter, γ_t denoting the tangential damping coefficient and $u_t = \| (\boldsymbol{u}_i - \boldsymbol{u}_j) - u_n \frac{\boldsymbol{n}}{\|\boldsymbol{n}\|} \|$ denoting the relative velocity in tangential direction. The Coulomb friction sets the upper limit for friction forces in this approach. Contact parameters, such as spring stiffness k_n and damping coefficient

$$\gamma_n = -2\sqrt{m_{ij} k_n} \frac{\ln e}{\sqrt{\pi^2 + \ln^2 e}} \tag{2.118}$$

are related to the coefficient of restitution e and the effective mass $m_{ij} = \frac{m_i m_j}{m_i + m_j}$ between particle i and particle j [88]. The time span of a typical collision

$$T_c = \frac{2\pi m_{ij}}{\sqrt{4 m_{ij} k_n - \gamma_n^2}} \tag{2.119}$$

can be estimated following [89].

The particle motion is integrated in time with a first-order semi-implicit Euler method. The particle velocity $\dot{v}_p = \frac{F}{m_p}$ is updated by using the total force F, which is obtained from fluid-solid interaction and collision. The angular acceleration $\dot{w}_p = \frac{T}{I}$ depends on the total torque T and the moment of inertia of a sphere $I = md^2/10$.

The coefficient of restitution is a material property related to the elasticity of a collision between two objects. The values for the materials used in this study are found in Tab. 5.1. Normal and tangential damping coefficients are assumed equal $\gamma_t = \gamma_n$. When interacting with a fixed obstacle, corresponding to the cylinder in Chap. 5, the effective mass m_{ij} is equal to the particle mass only. Choosing a value for T_c will determine stiffness and damping coefficients via eq. (2.118). In order to accurately resolve a solid collision, the granular time step Δt_G is commonly set about an order of magnitude smaller than the time step of the fluid solver Δt. We use a sub-stepping strategy to reduce the computational cost, where hydrodynamic force and torque are kept constant for a number $N_{sub} = \Delta t / \Delta t_G$ of sub-intervals.

2.6 Implementation

2.6.1 General description of waLBerla

waLBerla[2] is an extreme scale, open-source, C++ multiphysics software framework, that can be used as a tool box for designing various types of applications such as the LBM computation performed in [90]. It was designed from the ground up for high-performance computing (HPC) on massively parallel clusters [22, 91] and GPU-based systems [92], so that it is used as a reference implementation for LBM performance studies [93].

waLBerla uses automatic code generation to ensure excellent execution performance on a wide range of different architectures. This meta-programming paradigm allows to start the application development from a high-level description of the LBM method. All steps to derive the LBM kernel codes can be performed automatically: the code is not only optimized for specific architectures, but also becomes easier to change to test variants of the LBM methods.

The framework is based on a block-structured domain partitioning in order to achieve extreme scalability and node level performance [94, 21]. The full domain is divided into equally sized cuboids that can only be refined as a whole at a size ratio of 2:1 with direct neighbors. Load balancing is achieved on the level of such *blocks*, not individual cells. Every process can hold several blocks, but a block can only be assigned to one single process. Data from blocks is only available to the block that it has been assigned to. This structure allows code parallelization by the Message Passing Interface (MPI) or using hybrid MPI/OpenMP to guarantee optimal scalability on a wide range of different supercomputer architectures. In complex geometries, the meshing algorithm will loop over all blocks and all cells to determine if they are inside or outside the surface mesh and accordingly set them as fluid or empty cells. Blocks that

[2] `https://www.walberla.net`

hold no fluid cells can be discarded, but blocks that hold one or more fluid cells will be kept and stocked with the same set of data. This is necessary because the LBM kernel iterate over all cells equally, irrespective of whether they are fluid cells or not.

Code generation is handled by the *pystencils*[3] and *lbmpy*[4] packages [27]. It uses symbolic manipulation with the *sympy* algebra system to symbolically derive a stencil formulation from the continuous LBM collision operator. During this procedure several optimization techniques, such as common subexpression elimination and vectorization can be applied to generate highly efficient C/C++ code. Additionally, optimized code for GPUs can be generated. Thus waLBerla with *lbmpy* can achieve performance portabiliy to a wide range of different architectures.

2.6.2 Single node performance

This section demonstrates, that is possible to execute the collision models presented earlier at a performance close to the roofline model [95] when exploiting all available optimization techniques. A detailed reference on the optimization of LB kernels is [96]. Our LB kernels are generated in *lbmpy* and embedded in waLBerla , which handles communication and boundary conditions.

All benchmarks were run on a single node of the Kraken cluster[5], which is equipped with 36 cores on a dual socket Intel Xeon Gold 6140 Skylake configuration. The CPU frequency was fixed to 2.30 GHz during all tests. Each block holds $64 \times 64 \times 64$, which is large enough to ensure that data is stored in cache. The domain is fully periodic.

Performing one cell update of DdQq discretized LBM requires the transfer of $2 \cdot q \cdot 8$ bytes to and from memory when computing in double precision. We are interested in the D3Q19 model, which has a loop balance L of 304 $\frac{\text{B}}{\text{LUP}}$. The memory bandwidth $B = 164.82$ GB/s on a single node of Kraken was measured using *TheBandwidthBenchmark*[6]. The maximum attainable performance $P_{\max}$ is estimated according to the roofline model

$$P_{\max} = \frac{B}{L} = 164.82 \ \frac{\text{GB}}{\text{s}} \ / \ 304 \ \frac{\text{B}}{\text{LUP}} = 555.2 \text{ MLUPS}. \tag{2.120}$$

All LBM kernels are optimized by reducing the number of operations via common subexpression elimination in the formulation of the collision operator and the classic. Moreover, the collision and stream steps are fused into a single step stream-collide pattern. There are two different data structures available: the "Array of Structures" (AoS), where all PDFs of one cell are stored consecutively in memory and the "Structure of Arrays" (SoA), where all PDFs of the same direction are stored consecutively. To push the performance close to $P_{\max}$, one must make use of SIMD vectorization (here: AVX512) and non-temporal stores, which are only available for the SoA layout.

Fig. 2.8 and 2.9 show the measured performance for all collision operators used throughout this manuscript: BGK, TRT, MRT, BGK with SGS turbulence model, MRT with entropic stabilization and cumulants. When using SoA, the stream & collide kernel performs close to the predicted maximum performance and we reach circa 60% of $P_{\max}$ when including communication and the periodic boundaries. In contrast, the AoS stream & collide performs significantly worse

[3] `https://pypi.org/project/pystencils/`
[4] `https://pypi.org/project/lbmpy/`
[5] `https://cerfacs.fr/en/cerfacs-computer-resources/`
[6] `https://github.com/RRZE-HPC/TheBandwidthBenchmark`

and circa 40% of $P_{\max}$ are reached when executing the full LB scheme. All kernels can be run at similar computational efficiency, which means no CPU is lost when activating the SGS turbulence model or the entropic stabilization.

While the SoA data structure is employed for uniform grids (Sec. 3.8), the AoS data structure performed better for non-uniform refined grids like the swirler geometry in Chap. 4. As we will see later, the performance per node for this complex geometry is only 125 MLUPS (95 MFLUPS) per node. This is a point to be addressed in the future code development.

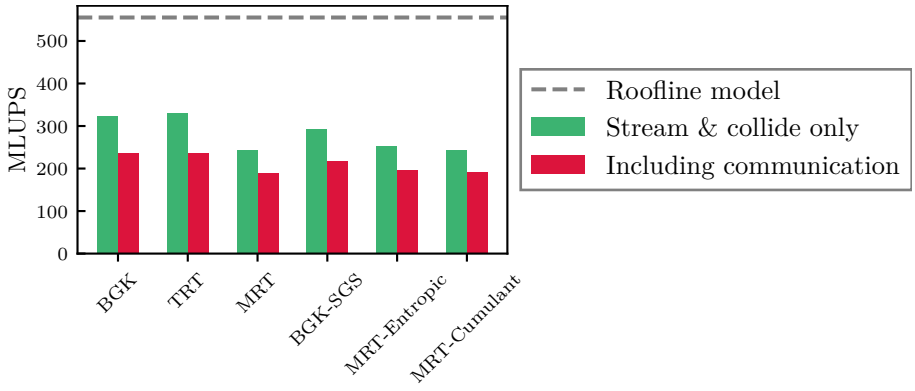

Figure 2.8 – Single node performance of different collision operators using the AoS data structure compared to the roofline model on Kraken.

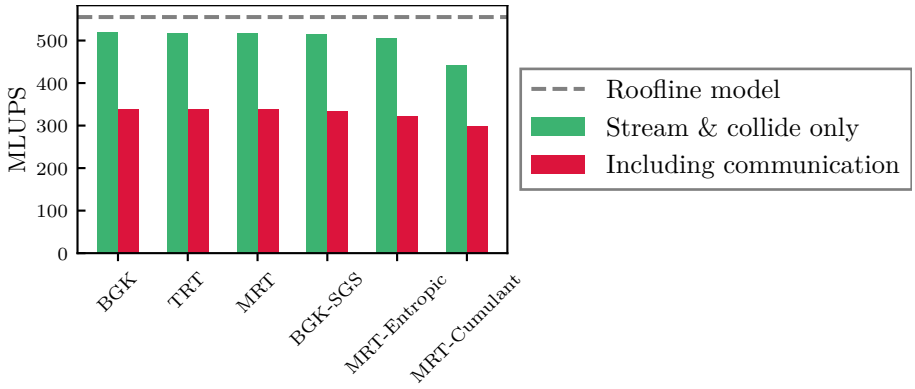

Figure 2.9 – Single node performance of different collision operators using the SoA data structure compared to the roofline model on Kraken.

2.6.3 Mesh creation

The refinement strategy for block structured grid used in waLBerla follows the approach by [97]. Blocks are refined at the ratio 2:1 with respect to their grid spacing. To maintain a constant speed of sound c_s when passing from level L to the finer level $L+1$, the timestep Δt is halved

$$\Delta x^{L+1} = \Delta x^{L}/2 \quad , \quad \Delta t^{L+1} = \Delta t_L/2. \tag{2.121}$$

The kinematic viscosity must remain constant on all levels, hence the lattice relaxation frequency is adjusted

$$\omega^{L+1} = \frac{1}{\frac{2}{\omega^L} - \frac{1}{2}}. \tag{2.122}$$

Since waLBerla runs on a block structured mesh, only whole blocks can be refined. Each block has the same shape and holds the same number of grid cells. The algorithm for treating the transition between blocks of different refinement levels requires a minimum block size is $16 \times 16 \times 16$ cells. Additionally the block size has to be divisible by two. Further information on the the time stepping algorithm and communication patterns can be found here [24].

Complex geometries with arbitrary shapes are meshed by covering the fluid domain with equally sized blocks of the coarsest level. Blocks that have been marked for refinement are divided into eight finer blocks. This process continues recursively until the desired refinement level is reached throughout the domain. Blocks that contain reside entirely outside the geometry, i.e. hold zero fluid cells, are discarded. Note that this meshing mechanism can be executed during the initialization phase of each simulation since it is very fast and does not require a volume mesh as input. The workload is balanced by distributing blocks among available processes. A fully distributed data structure means that each process only has knowledge of its own blocks and neighboring blocks on other processes. Because processes allocate cell data exclusively for their own blocks ,the memory consumption of a process does not depend on the entire simulation but only on the number of assigned blocks . Finally fluid cells are marked by computing the signed distance to the surface mesh and boundary cells are set as a hull to the fluid cells.

Fig. 2.10 illustrates the mesh creation procedures on the example of the swirler from Chap. 4. The block size is $32 \times 16 \times 16$ cells and four refinement levels are used.

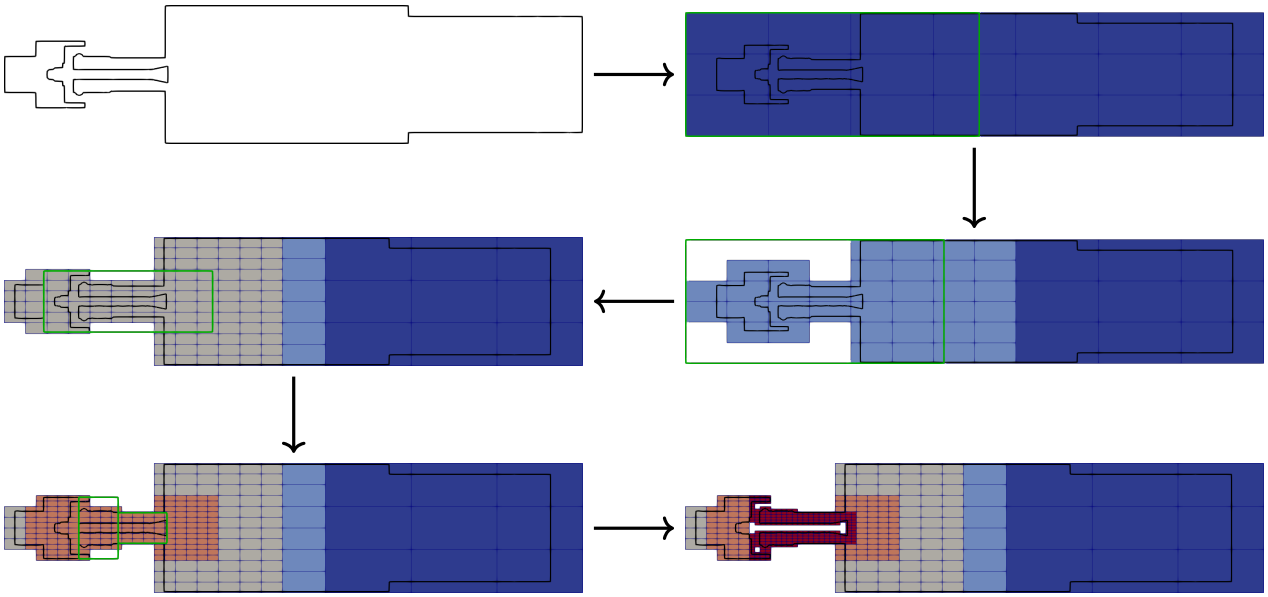

Figure 2.10 – Intermediate steps in the mesh creation process of waLBerla. The surface mesh is colored black and the refinement level is indicated from blue to red. Green rectangles mark the refinement zones on the corresponding level. Each block holds the same number of grid cells ($32 \times 16 \times 16$).

2.6.4 Fluid-solid coupling algorithm

Successfully simulating particulate flows requires the execution of presented methods in the correct order. We start by initializing the fluid and placing the particles in the domain. Grid cells that reside inside the particle radius are marked solid cells, the remaining cells are fluid. All fluid cells in the direct vicinity of a solid are additionally marked as boundary cells, that have to be treated during the treatment of boundary conditions.

As the particles move through the domain, this mapping of fluid and solid cells has to be repeated at the beginning of each timestep. In the event that a cell, which was marked as solid in the previous timestep, turns into a fluid cell the PDF refilling mechanism has to be called (Sec. 2.4.1). Next, we perform the LB collision (Eq. (2.24)), communicate PDFs on the outer cell layer of each block to its neighbors, apply the boundary condition for moving obstacles (Sec. 2.4) and execute the LB streaming (Eq. (2.25)). Hydrodynamic forces and torque are computed during the boundary treatment locally on each block and synchronized in the next step to obtain the total force (Eq. (2.107)) and torque (Eq. (2.108)) acting on each particle.

Ladd [98] proposed to average force and torque on particles during two consecutive timesteps because the bounce back type boundary conditions cause oscillation in the hydrodynamic interaction at the frequency of two timesteps. To dampen these undesired oscillations we store force and torque at the current timestep t before averaging them with the values from the previous timestep $t-1$.

Now the granular solver is called for N_{sub} sub-intervals during which hydrodynamic force and torque are kept constant. Particle overlaps are detected and resolved as collisions (Eq. (2.116), (2.117)), their position and velocity is integrated in time and synchronized between blocks. The evaluation of different inter-particle forces, such as a lubrication correction, can be inserted here. The number of required sub-intervals depends on collision parameters.

Algorithm 1: Pseudocode of the LBM-DEM coupling approach

```
Initialize fluid and particles; map particles into the domain
for every time step t do
    Update particle mapping
    Refill PDF in empty fluid cells
    Perform LB collision step
    Communicate PDFs between blocks
    Apply boundary conditions
    Perform LB stream step
    Compute total hydrodynamic force and torque on particle and average them
    for every sub-interval N_sub do
        Evaluate inter-particle forces (e.g. lubrification correction)
        Detect and resolve particle collisions
        Integrate particle position and velocity in time
        Synchronize particles between blocks
    end
end
```

Chapter 3

Validation

Contents

This chapter presents restrictions of the LBM approach in various Navier-Stokes problems, where analytic or high fidelity numerical solutions are available. Most cases are unsteady in order to stress the method more and allow us to verify its limits. We will investigate the interaction of fluid and solid walls, the particle response to sudden velocity changes in the carrier fluid and oscillating external forces in the Stokes limit. Furthermore, the Segré-Silberberg effect and the granular drag coefficient of a cylinder are validated. Finally, we compare three different strategies (BGK-SGS, entropic stabilized MRT, cumulants) for modeling the turbulent flow between two parallel plates. Verifying the accuracy of these basic fluid flow problems gives us the confidence to continue with more complex configurations.

3.1 First Stokes problem

The first Stokes problem, also known as Rayleigh problem, is one of the few unsteady flows for which we can find an exact solution of the Navier-Stokes equations [99]. Consider an infinitely long plate at $y = 0$, that is at rest at $t = 0$ and abruptly starts moving at constant velocity $u(y = 0, t > 0) = u_0$ in tangential (x) direction. Initially, the fluid is at rest throughout the domain $u(y > 0, t = 0) = 0$ and is driven only by the plate motion, not by any external pressure gradient. A no-slip boundary condition is applied on the wall, causing the fluid in direct vicinity of the plate to move at velocity

$$u(0, t > 0) = u_0.$$

This condition does not influence the fluid at infinity, where $u(y = \infty, t) = 0$. Under these assumptions, the incompressible Navier-Stokes equations can be reduced to the one-dimensional diffusion equation

$$\frac{\partial u}{\partial t} = \nu \frac{\partial^2 u}{\partial y^2}. \tag{3.1}$$

The self-similar solution is found by introducing the variable

$$\eta = \frac{y}{\sqrt{\nu t}},$$

such that $u = f(\eta)$. Substitution into Eq. (3.1) reduces the partial differential equation to an ordinary differential equation

$$f" + 1/2\eta f' = 0.$$

Integrating the function

$$f' = Ae^{-\eta^2/4}$$

yields

$$f = B + A \int_0^\eta e^{-k^2/4} dk,$$

with the integration constants A and B. Considering the boundary condition mentioned earlier, the solution to the initial problem is [29]

$$\frac{u}{u_0} = 1 - \mathrm{erf}\left(\frac{y}{2\sqrt{\nu t}}\right), \tag{3.2}$$

with the error function

$$\mathrm{erf}(x) = \frac{2}{\sqrt{\pi}} \int_0^x e^{-k^2} dk \quad \text{and} \quad \mathrm{erf}(+\infty) = 1.$$

The wall shear stress between plate and fluid is obtained by [100]

$$\tau_w = \mu \left(\frac{\partial u}{\partial y}\right)_{y=0} = -\frac{u_0 \sqrt{\rho \mu}}{\sqrt{\pi t}}. \tag{3.3}$$

We choose

$$\tau_t = \frac{\nu}{u_0^2}$$

as the characteristic time scale. The motion of the plate is progressively transported through vorticity diffusion to the outer fluid regions. But the velocity profile is geometrically similar at

different points of time and always a function of η. Fig. 3.1 depicts the velocity profiles in terms of η obtained from our simulations with $u_0 = 0.1$ in lattice units. We present the results for a lattice relaxation frequency of $\omega_{\mathrm{LBM}} = 0.4$, because problems in the Stokes regime are typically run at the lower limit of lattice relaxation frequency. At high relaxation rates $\omega_{\mathrm{LBM}} \to 2$ the convergence towards the analytic solution takes longer in terms of characteristic time scale. The simulation domain spans 60 cells in the direction of the plate motion (x) and 120 in wall normal direction (y). The domain is periodic in x and the velocity is imposed via no-slip condition at the bottom and top boundaries. We observe that the numerical results deviate

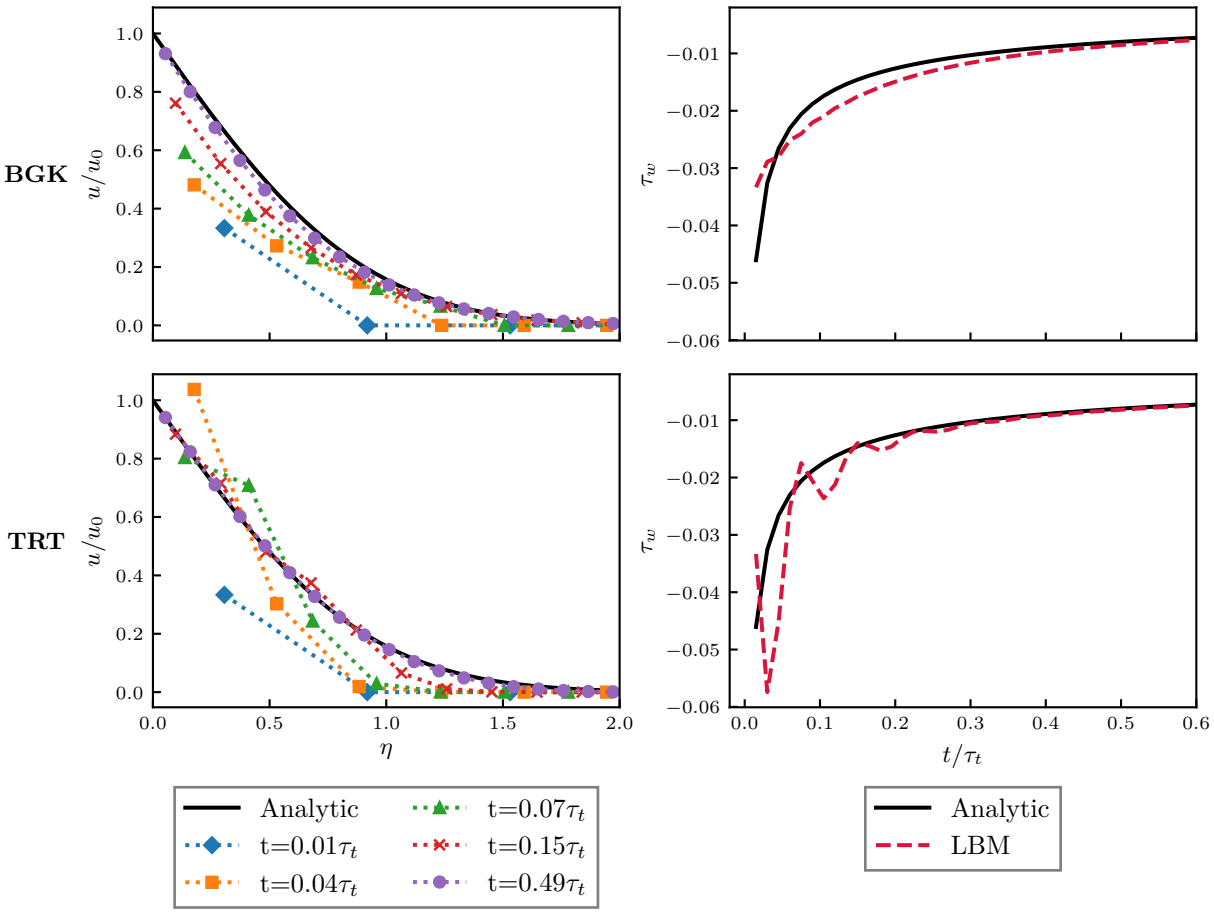

Figure 3.1 – Left: velocity profiles of LBM and theory for different timesteps (characteristic time scale $\tau = 66.7$); Right: Wall shear stress; Top: BGK; Bottom: TRT ($\Lambda = 3/16$)

.

considerably from the analytic solution at the initial phase of the simulation but approach the correct velocity profile after $t = \frac{1}{2}\tau_t$. The LBM requires approximately half a characteristic time scale to react to the sudden change in velocity at the boundary. The BGK collision model underestimates the velocity profile during the initial transient period, while the TRT model ($\Lambda = 3/16$) under- and overestimates for different times (see Fig. 3.1 left).

3.2 Second Stokes problem

The second Stokes problem is similar to the first one, except that the plate is not moving with constant velocity but oscillating at frequency ω_t/π. The Navier-Stokes equations can be simplified in the same manner as Eq. (3.1). The motion of the plate is prescribed as

$$u(0,t) = u_0 \cos(\omega_t t)$$

and the fluid is quiescent at infinite distance from the wall $u(\infty,t) = 0$ [28]. The velocity is expressed as the real part of the complex function

$$u = u_0 \Re\left(e^{i\omega_t t} f(y)\right)$$

Substitution into the partial differential equation yields

$$f'' - \frac{i\omega_t}{\nu} f = 0.$$

Considering the boundary conditions, the function

$$f(y) = \exp\left(\frac{1+i}{\sqrt{2}}\sqrt{\frac{\omega_t}{\nu}}y\right)$$

is a solution to the differential equation and leads to the fluid velocity profile [29, 100]:

$$\frac{u}{u_0} = \exp\left(-\sqrt{\frac{\omega_t}{2\nu}}y\right)\cos\left(\omega_t t - \sqrt{\frac{\omega_t}{2\nu}}y\right). \tag{3.4}$$

The penetration depth

$$\delta = \sqrt{\frac{2\nu}{\omega_t}}$$

is a measure of how far the oscillating motion of the plate reaches into the fluid. It decreases with frequency for a fluid at constant kinematic viscosity. We choose the characteristic timescale

$$\tau_t = \frac{L^2}{\nu}$$

and the longitudinal displacement as characteristic lengthscale

$$L = 2u_0 \int_0^{\frac{\pi/2}{\omega_t}} \cos(\omega_t t) = \frac{2u_0}{\omega_t}$$

for this problem. The wall shear stress

$$\tau_w = \mu\left(\frac{\partial u}{\partial y}\right)_{y=0} = \mu u_0 \sqrt{\frac{\omega_t}{\nu}}\cos\left(\omega_t t - \frac{3\pi}{4}\right) \tag{3.5}$$

has a phase lag of $3\pi/4$ relative to the wall velocity [28].

The simulation domain spans 60 cells in the direction of the plate motion (x) and 120 in wall normal direction (y). The domain is periodic in x and the velocity is imposed via no-slip condition at the bottom and top boundaries. All simulations are conducted at lattice relaxation frequency $\omega_{\mathrm{LBM}} = 0.4$ and the wall velocity amplitude is determined by satisfying

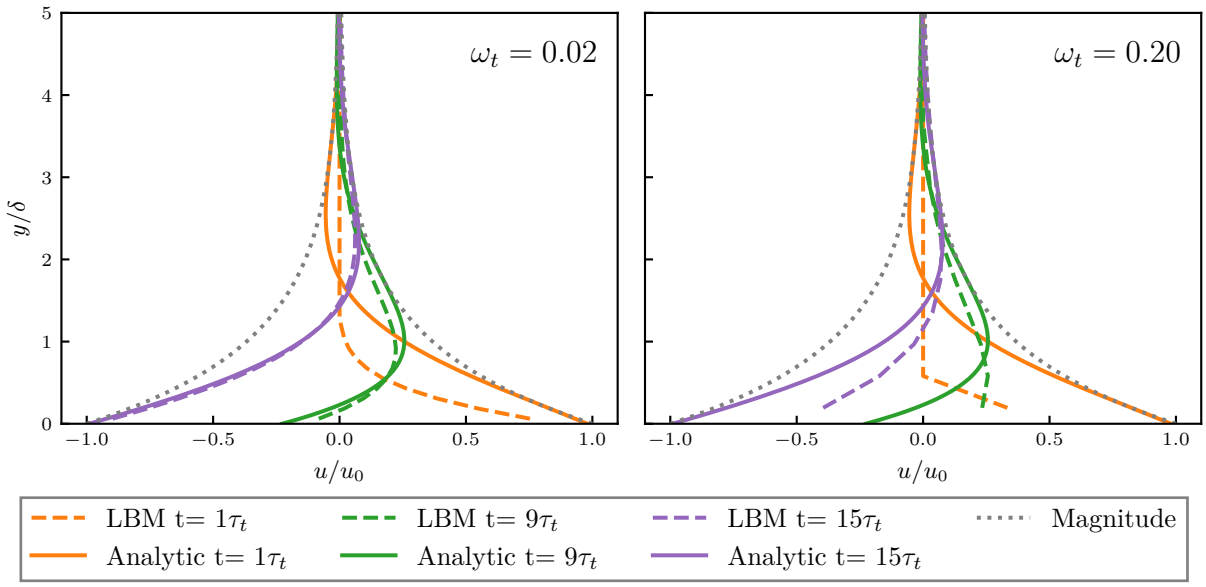

Figure 3.2 – Numeric and analytic velocity profiles for plate oscillation $\omega_t = 0.02$ ($\delta/\Delta y = 8.2$) and $\omega_t = 0.2$ ($\delta/\Delta y = 2.6$) after $\tau_t = 1, 9, 15$ characteristic timescales. The dotted line is the magnitude of the analytic solution.

$\mathrm{Re} = \frac{u_0 L}{\nu} = 0.1$. Analytic velocity profiles along the wall normal direction for three exemplary times are presented in Fig. 3.2, along with the numerical solution using the BGK collision model . The analytic solution does not consider the initial transient but the simulation is initialized with zero fluid velocity throughout the domain. Hence, there is a deviation between LBM and theory at the beginning of simulation. At later times the LBM approaches the predicted velocity profile, but will always lag behind the analytic solution. The phase shift between numerical and analytic solution in terms of the force exerted on the plate increases with the plate oscillation frequency as illustrated on the right side of Fig. 3.3. At $\omega_t = 0.5$ the penetration is of the same order of magnitude as the lattice grid size $\delta/\Delta y = 1.6$ and thus the boundary layer is not sufficiently resolved. The ratio of wall shear stress amplitude between LBM and analytic is shown on the left side of Fig. 3.3. Results are presented for the BGK and the TRT collision model ($\Lambda = 3/16$). TRT consistently delivers better results than BGK, especially in terms of the amplitude at high plate oscillation frequencies.

3.3 Particle response

A spherical particle immersed in a viscous fluid experiences a force that seeks to diminish the relative velocity between the two phases. In order to verify our numerical approach we need to check if the particle reacts accurately to the surrounding fluid. The typical momentum response time, or particle time scale is [88, 101]

$$\tau_p = \frac{(\rho_p + \rho_f/2)d^2}{18\mu_f}, \tag{3.6}$$

with the fluid viscosity μ_f, fluid density ρ_f and particle density ρ_p. This is the characteristic time over which a particle responds to a change of velocity of the carier fluid. The term $\rho_f/2$ is due to the added-mass effect. Heavy and large particles need a longer time to adapt to the

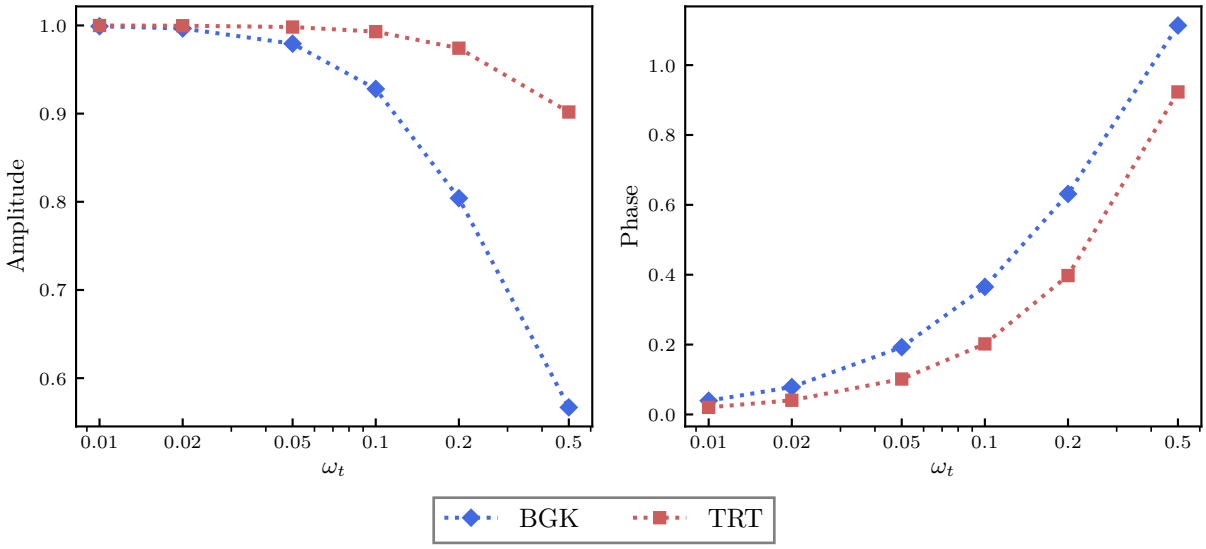

Figure 3.3 – Wall shear stress amplitude ratio of LBM to analytic solution $A_{\mathrm{LBM}}/A_{\mathrm{Analytic}}$ and phase lag $\phi_{\mathrm{LBM}} - \phi_{\mathrm{Analytic}}$ for the second Stokes problem.

fluid phase and increasing the fluid viscosity leads to faster response. Not considering gravity and assuming that the Reynolds number $\mathrm{Re} = \frac{d\rho_f w}{\mu_f} \ll 1$ is low, the total force acting on the sphere is

$$F(t) = \underbrace{3\pi\mu_f d w(t)}_{\text{steady drag}} + \underbrace{3\pi\mu_f d \int_0^t \frac{dw}{dt'} K_\mu(t-t')dt'}_{\text{history force}} + \underbrace{\frac{1}{12}\rho_f \pi d^3 \frac{dw}{dt}}_{\text{added-mass effect}}, \tag{3.7}$$

where $w(t) = u_f(t) - u_p(t)$ is the slip velocity between uniform fluid flow and particle and K_μ is the memory kernel [102, 103]. It can be computed for solid spherical particles ($\mu^* = \infty$) as

$$K_\mu\left(t, \mu^* = \infty\right) = \frac{1}{\sqrt{\pi t/\tau_\nu}}, \tag{3.8}$$

with the viscous time scale $\tau_\nu = d^2/4\nu_f$.

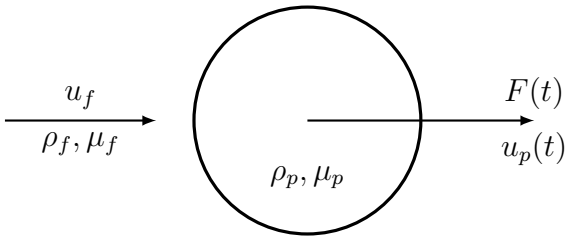

Figure 3.4 – Sphere immersed in a carrier fluid with slip velocity $w = u_f - u_p$

The first term, also called Stokes' law, is the drag, which is mainly caused by the viscosity of the fluid and pressure distribution. We will comment on the second term - the history force - in detail in Sec. 3.4. As the sphere accelerates, it moves into the physical space that is occupied by fluid. The additional inertia of the fluid that is pushed away by the particle is the added mass, also called virtual mass. It has been shown for incompressible fluid, that it is equivalent

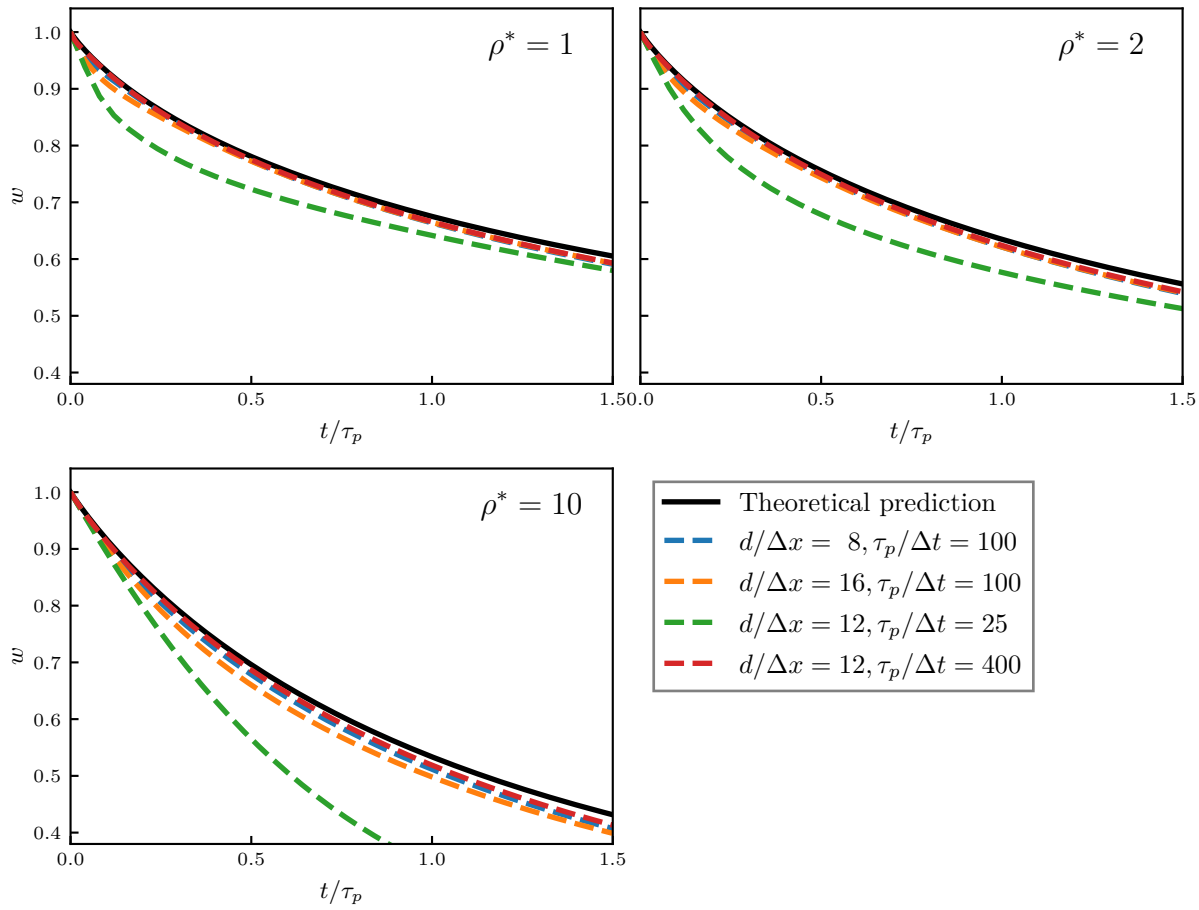

Figure 3.5 – Relative velocity of a particle that is subject to a sudden change in velocity of the carrier fluid. Particle is being kept fixed until the flow has converged and the particle is released at $t = 0$. Numerical prediction takes steady drag, added-mass effect and history force into account. Simulations conducted with varying spatial $d/\Delta x$ and temporal resolutions $\tau_p/\Delta t$.

to half the mass the fluid would obtain within the particle volume [101]. It is further assumed that the sphere is rigid and therefore has no viscosity $\mu^* = \mu_p/\mu_f = \infty$.

For our simulation a single sphere is placed in the center of a domain, which spans 20 particle diameters d in every spatial direction. A uniform and constant velocity $u_{in} = u_f$ is imposed at the inlet and a constant pressure at the outlet. The domain is periodic in cross-stream direction. During the initial phase of the simulation, the sphere is kept fixed in space until the drag force has converged to the steady Stokes drag. Then the sphere is released and its velocity is recorded. Fig. 3.5 shows the slip velocity between fluid and particle for neutrally buoyant ($\rho^* = \rho_p/\rho_f = 1$), slightly inertial ($\rho^* = 1$) and highly inertial ($\rho^* = 10$) particles. The fluid viscosity μ_f and fluid velocity u_f are adjusted to ensure a constant Reynolds number $\mathrm{Re} = 0.05$ for all simulations. We employed the TRT collision model with $\Lambda = 1/4$. The particle's trajectory is compared to theoretical predictions that are computed by integrating Eq. (3.7) in time.

We examine the influence of resolution for this flow problem in space $d/\Delta x$ and time $\tau_p/\Delta t$. The particle acceleration is well captured by the LBM simulation except when the particle has to respond quickly ($\tau_p/\Delta t$ is low). This deviation intensifies with increasing relative particle

density ρ^*. The influence of lattice cells per sphere diameter is small in the investigated range ($8<d/\Delta x<16$) compared to the influence of the particle time scale.

3.4 Basset history force

The so-called Basset history force, also known as Boussinesq–Basset force [30, 31], is a consequence of the unsteady diffusion of vorticity as the particle starts accelerating. The Basset force arises from viscous effects and depends on the particle's acceleration history, from the beginning $t = 0$ to the present time t hence the name "history" force:

$$F(t) = 3\pi\mu_f d \int_0^t \frac{dw}{dt'} K_\mu(t - t', \mu^*) dt'. \tag{3.9}$$

For the definition of the memory kernel, see Eq. (3.8). To examine the history term in particular, we fix the sphere in space and expose it to a sudden change in velocity of the carrier fluid. In this case the slip velocity is constant $w(t) = w_0$, which eliminates the added-mass term and

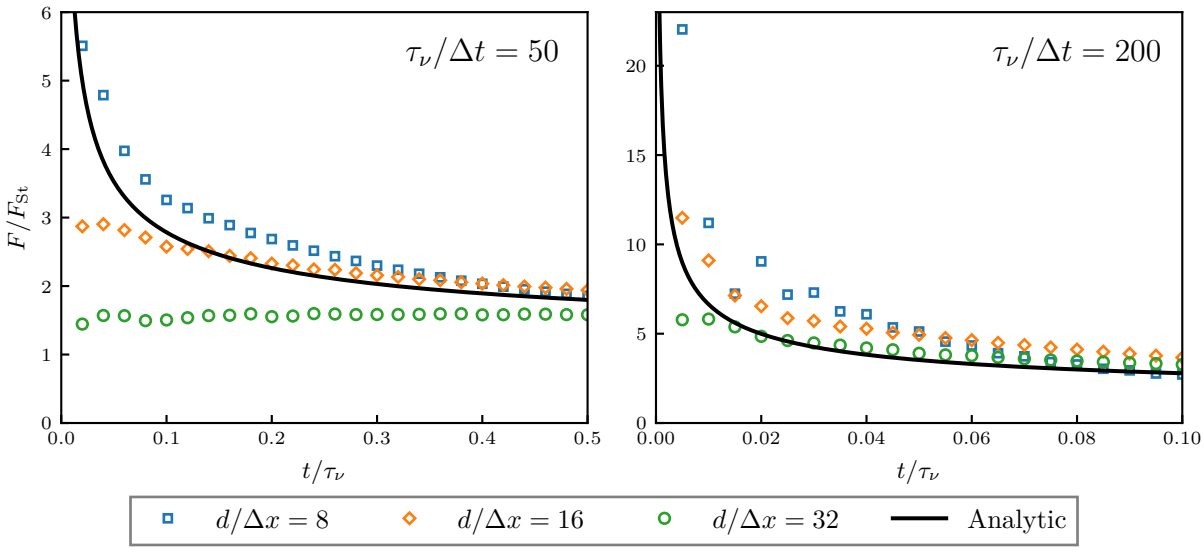

Figure 3.6 – Hydrodynamic force F (consisting of steady drag F_{St} and history force F_{BH}) acting on a fixed sphere as reaction to a sudden change in the carrier fluid velocity. Simulations conducted with varying spatial $d/\Delta x$ and temporal resolutions $\tau_\nu/\Delta t$.

leads to the total force on the particle

$$F(t) = \underbrace{3\pi\mu_f d w_0}_{\text{steady drag}} + \underbrace{3\pi\mu_f d K_\mu(t) w_0}_{\text{history force}}. \tag{3.10}$$

The simulation setup is identical to the one in the previous chapter: the domain spans 20 particle diameter, the Reynolds number is fixed to $\mathrm{Re} = 0.05$ and TRT with $\Lambda = 1/4$ is used. The forces in figure Fig. 3.6 are normalized by the steady drag force F_{St}. The history force is clearly present in the LBM simulations, but can deviate from the theoretical prediction depending on spatial and temporal resolution. We observe that for the smaller characteristic time scale $\tau_\nu = 50$, the history force is underestimated for resolutions greater than $d/\Delta\mathrm{x} \geq 16$ during the first few time steps of the simulation. This error is even bigger at resolution $d/\Delta\mathrm{x} = 32$.

At time scale $\tau_\nu/\Delta t = 200$ the force during the first few iterations is underestimated for $d/\Delta \mathrm{x} = 32$ and overestimated for $d/\Delta \mathrm{x} = 8$. All computations at $\tau_\nu/\Delta t = 50$ and $\tau_\nu/\Delta t = 200$ roughly converge to the analytic prediction after $t/\tau_\nu = 0.5$ and $t/\tau_\nu = 0.1$, respectively. Small viscous time scales and high spatial resolutions lead to dangerously low lattice relaxation frequencies ω_{LBM}. This behavior demonstrates that increasing the spatial resolution does not always improve the accuracy when using the LBM because it will decrease the lattice relaxation frequency even further.

3.5 Oscillating particle

We now investigate the particle's unsteady response to an external oscillatory force $\boldsymbol{F}_{\mathrm{ext}} = 3\pi\mu d\boldsymbol{u}_0 \sin(\omega t)$, where $\omega/2\pi$ is the oscillation frequency, $\boldsymbol{u}_0$ is a constant vector and μ is the dynamic viscosity. A single sphere is embedded in a fluid at rest with no gravity. The theoretical particle velocity can be obtained by solving the Maxey-Riley equation [103]

$$\begin{aligned} m_p \frac{d\boldsymbol{u}_p}{dt} =& -3\pi d\rho_f \nu \left(\boldsymbol{u}_p - \boldsymbol{u}_f\right) + m_f \frac{D\boldsymbol{u}_f}{Dt} + \frac{m_f}{2}\left(\frac{D\boldsymbol{u}_f}{Dt} - \frac{d\boldsymbol{u}_p}{dt}\right) \\ & - \frac{3}{2} d^2 \rho_f \sqrt{\pi\nu} \int_{t_0}^{t} \frac{1}{\sqrt{t-\tau}} \left(\frac{d\boldsymbol{u}_p}{d\tau} - \frac{d\boldsymbol{u}_f}{d\tau}\right) d\tau, \end{aligned} \tag{3.11}$$

following the approach of Wang et al. [104]. Eq. (3.11) is only valid for the Stokes regime ($\mathrm{Re} \ll 1$) and does not incorporate the Faxén terms in added mass, drag and history force contributions.

The resulting oscillating motion of the particle is expressed as

$$\boldsymbol{u}_p(t) = \alpha \boldsymbol{u}_0 \sin(\omega t + \varphi), \tag{3.12}$$

with amplitude α and phase shift φ. When the particle is embedded in a quiescent fluid, the analytical solution gives a relation between the amplitude of external oscillatory forcing (written as $F(t) = \widehat{F} e^{i\omega t}$) and the particle velocity as

$$\widehat{F} = \widehat{u}_p \left[(m_p + \frac{1}{2} m_f) i\omega + 3\pi\mu d (1 + \delta e^{i\pi/4}) \right] e^{i\varphi}. \tag{3.13}$$

The terms on the right hand side of eq. (3.13) correspond respectively to particle inertia, added mass, steady and unsteady drag forces. The contribution of Basset history force is important for neutrally buoyant particles and when the particle-to-fluid density ratio is low to moderate. The amplitude and phase shift of the particle velocity are presented in Fig. 3.7 for particle-fluid density ratios up to $\rho^* = 5$ with $\psi^2 = \omega d^2/\nu$. The purely viscous contribution of the hydrodynamic force (in the absence of added mass term) is also plotted. This dimensionless frequency ψ^2 can be interpreted as a Stokes number corresponding to the ratio of the particle relaxation time to the fluid oscillation time scale. It is also the square of the ratio of the particle diameter to the Stokes layer thickness. The cubic simulation domain spans 10 particle diameters and is periodic in all directions. The BGK and TRT collision operator with $\Lambda = 1/4$ are compared for this setup.

Additionally, numerical results from the JADIM code [105] are depicted, which is a incompressible finite volume method solver. It employs the Force-Coupling method (FCM) [106, 107, 108], which is a numerical model for the simulation of suspension flows, which is able to couple

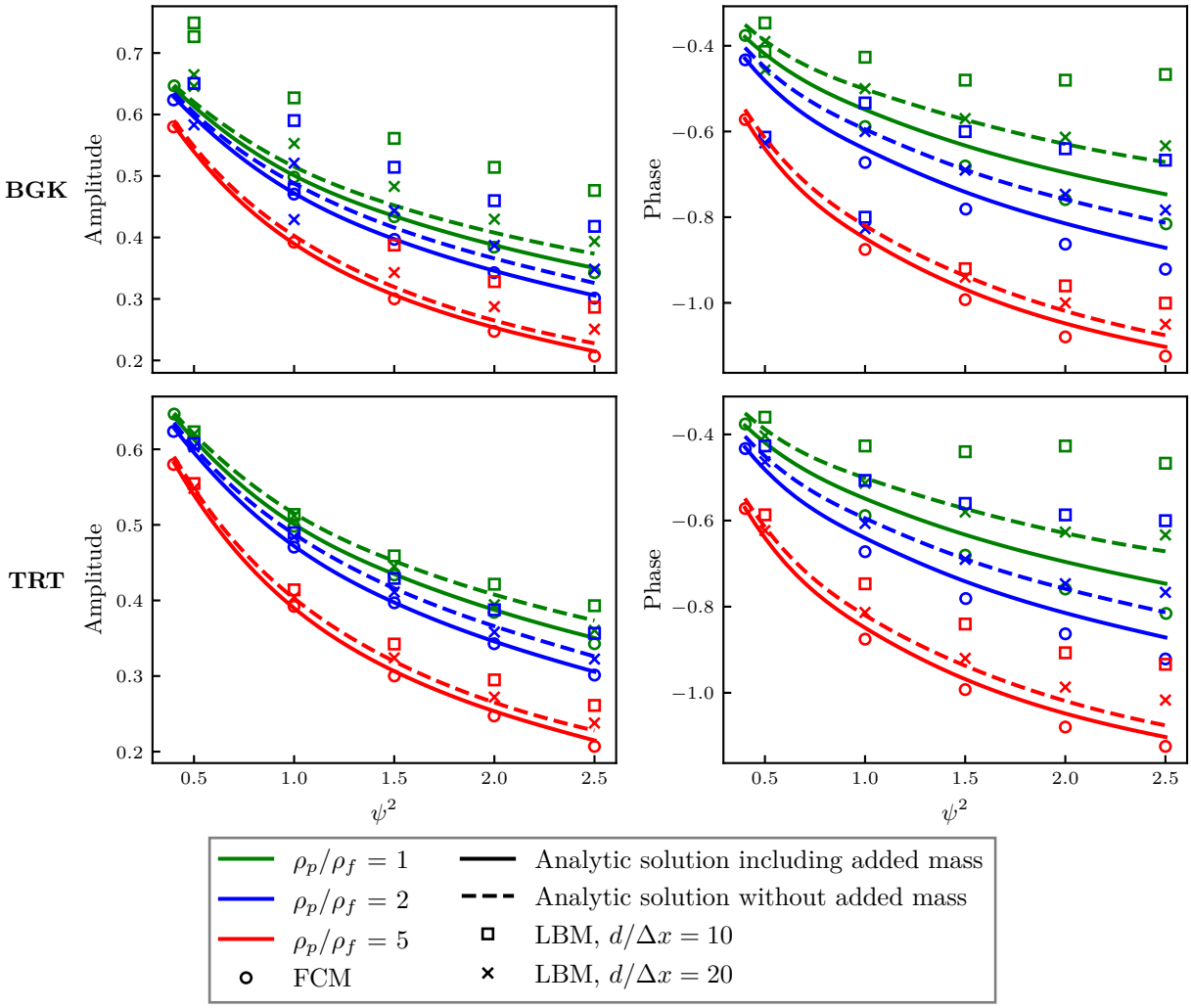

Figure 3.7 – Amplitude and phase shift of external force to particle velocity. $\psi^2 = \omega d^2/\nu$ is the dimensionless frequency. The resolution is given by the number of lattice cells per particle diameter d/Δx.

simultaneously the solution of the fluid flow equations and the Lagrangian tracking of the particles. The FCM is based on a low-order, finite multipole expansion of the velocity disturbance induced by the presence of the particles. FCM results are found in [104].

Our fluid-solid-coupling approach delivers good results for a resolution of d/Δx $= 20$, but exhibits a slight overestimation of amplitude and significant underestimation of the phase shift for d/Δx $= 10$ because for high ψ^2, the Stokes layer is too thin to be accurately resolved. The deviation is stronger for smaller particle density and faster oscillation. It is clear that LBM predictions become gradually closer to the theoretical prediction while particle density is increased because the relative contribution of unsteady Basset drag reduces. The TRT model produces significantly better outcome than the BGK model, especially in terms of the amplitude. This is consistent with the earlier results from the second Stokes problem (Fig. 3.3). Since the FCM was especially designed for particulate simulations at low Reynolds numbers, it is not surprising that it yields more accurate results.

3.6 Segré-Silberberg effect

The Segré-Silberberg [32] effect is another relevant way to test implementation of the fluid solid coupling strategy. A neutrally buoyant sphere is immersed in a steady laminar flow between two parallel plates. The fluid exerts a drag force which carries the sphere in streamwise direction and the parabolic flow field generates a lift force making the sphere migrate towards one of the channel walls. Close to the wall a hydrodynamic interaction between the two objects acts counter to the lift force and eventually the sphere will reach an equilibrium position relative to the wall. This phenomenon depends on the ratio between the sphere diameter and the channel width, as well as the Reynolds number. Fig. 3.8 depicts the lateral migration of the particle towards the equilibrium state.

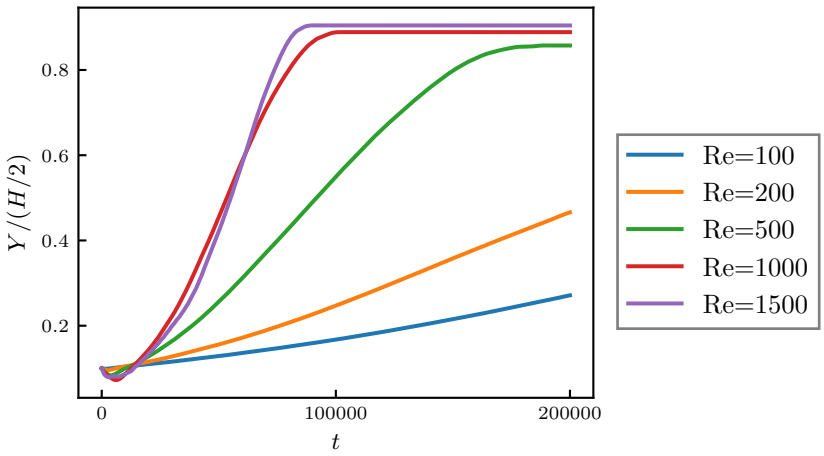

Figure 3.8 – Lateral position Y of a particle with $d/\Delta x = 8$ over 200000 timesteps in a laminar parallel channel flow. Reynolds number $\mathrm{Re} = \frac{\bar{u}H}{\nu}$ is based on the mean fluid velocity $\bar{u}$, the channel height H and the kinematic fluid viscosity ν. Y is equal to 0 at the channel center and $H/2$ at the wall.

The Guo force model (Eq. (2.99)) is used to drive the flow with an acceleration corresponding to the pressure gradient

$$a = -\frac{dp}{dx} = \frac{\tau_w}{H/2}, \tag{3.14}$$

where the wall shear stress is equivalent to $\tau_w = 6\nu\bar{u}/H$. We need to use the TRT collision model with $\Lambda = 3/16$ to obtain the correct Poiseuille velocity profile in this flow configuration. The channel is $16d$ high, $14.4d$ long and $6d$ wide. Different resolutions, i.e. number of lattice cells per particle diameter $d/\Delta x$, of our computations are compared to the prediction of Asmolov [109] from matched asymptotic theory.

Fig. 3.9 shows the particle's relative position inside the channel when reaching an equilibrium state. The underlying physical mechanism is well recovered, but error increases at higher resolutions. This behavior seems arbitrary, but it has been shown for TRT with $\Lambda = 3/16$ that the drag force acting on spheres packing is underestimated below $d/\Delta x = 10$ and overestimated above. It is converging to the expected value at much higher resolution $d/\Delta x > 60$ [111]. With the number of lattice cells per diameter $d/\Delta x = 10$ that is chosen for the following simulations the accuracy is better than 4%.

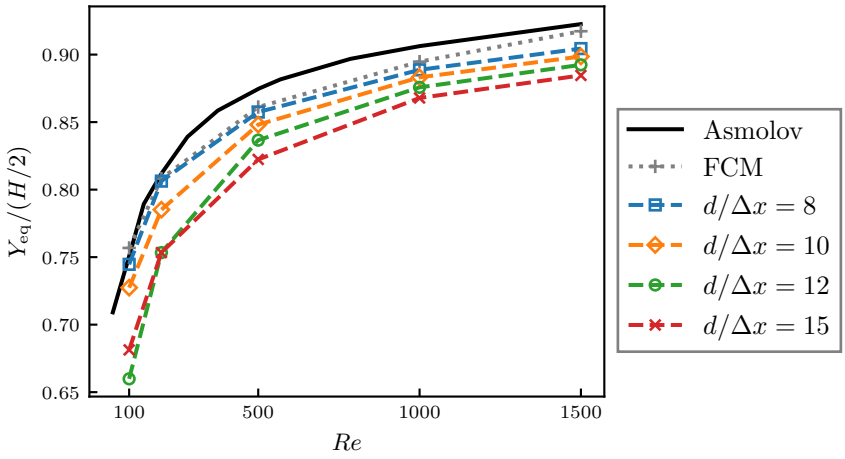

Figure 3.9 – Equilibrium position Y_{eq} of a sphere in a laminar parallel channel flow. Asmolov reference values are taken from [109]. FCM results are found in [110]

3.7 Granular drag coefficient

Granular drag, unlike fluid drag, depends mainly on the Knudsen number

$$\mathrm{Kn} = \frac{d}{6\sqrt{2}\Theta_\infty D} \tag{3.15}$$

but also on material properties. The drag coefficient of a granular system on a cylinder of diameter D

$$c_{D,G} = \frac{F_{D,p}}{1/2\rho_p \Theta_\infty u_\infty^2 (D+d) L_z} \tag{3.16}$$

is calculated from the drag force $F_{D,p}$, which is made dimensionless by using the particle density ρ_p and diameter d, the upstream solid volume fraction Θ_∞ and velocity u_∞.

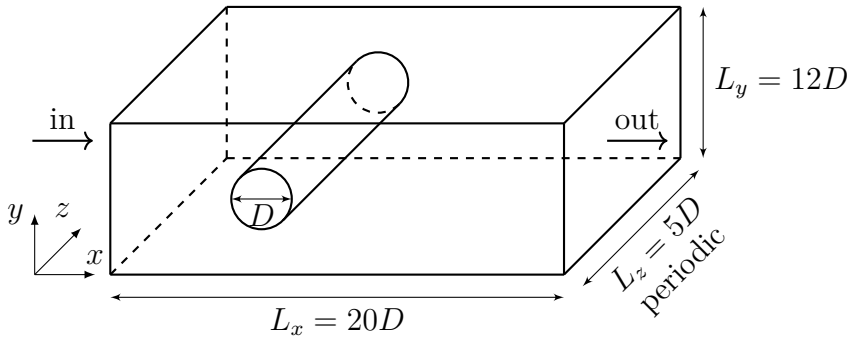

Figure 3.10 – Schematic presentation of the simulation domain.

We perform simulations of purely granular flows - without the presence of a fluid - to compare the value of granular drag coefficient to experiments from literature. The computational domain spans 20 cylinder diameters in streamwise direction, 12 cross-stream, and 5 spanwise and is periodic in spanwise direction (see Fig. 3.10). At initialization the domain is empty but particles will be injected at the inlet at random location with velocity $u_x = u_\infty$. They are removed from the simulation once they leave the domain. No velocity fluctuations are added

to the particles, so that the upstream granular temperature is $T_\infty = (u_y^2 + u_z^2)/2$ [112]. The simulation duration is equal to six flow-through times $\tau_t = L_x/u_\infty$ and the initial transient phase, which is not considered for the computation of the average drag force, is $t_{\text{init}} = 1\tau_t$. We will test particles of two different sizes: $d = D/5$ and $d = D/10$.

Snapshots of the instantaneous particle position in Fig. 3.11 reveal the formation of a bow shock in front of the cylinder, which is typical of granular flows [113].

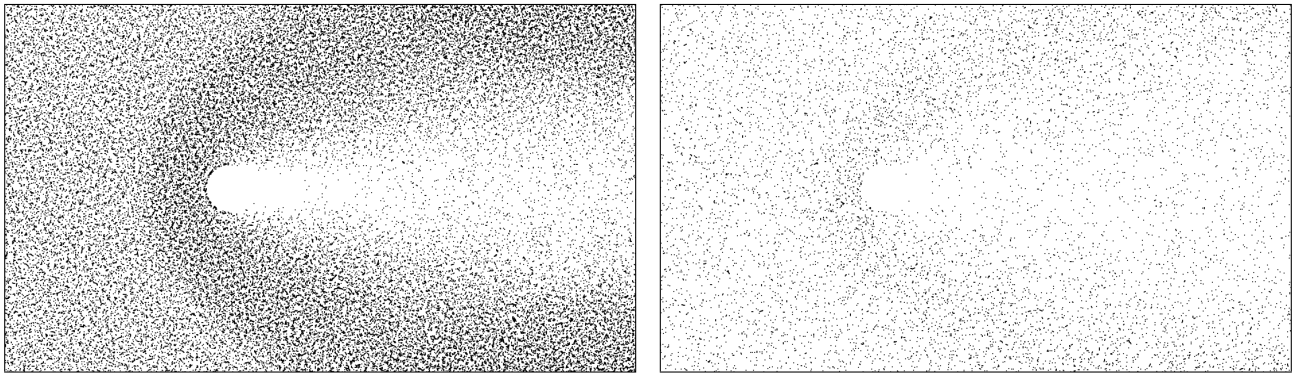

Figure 3.11 – Instantaneous snapshot of particle positions of size $d = D/5$ at Kn = 0.1 (left) and Kn = 0.5 (right).

Wassgren et al. [112] presented a theoretical derivation of the expected drag coefficient for different coefficients of restitution e. Their prediction for a uniform, non-interacting stream of particles $c_{D,G} = 4\,(e+1)\,/3$ is depicted in Fig. 3.12 (left) together with our simulations of frictionless particles.

The prediction becomes more accurate as the Knudsen number increases, due to fewer inter-particle collisions taking place. The relation between drag coefficient and Knudsen number has been examined by Boudet & Kellay [114]. In their experiments, they used an aluminum cylinder in combination with steel spheres ($e = 0.93$), for cylinder to particle diameter ratios $D/d = 27, 110$ and glass beads at $D/d = 92$. The line in Fig. 3.12 (right) represents their best fit over all experimental results. Our simulations do not follow the curve exactly but show the same trend. Simulations with and without friction do not show a notable difference. Even though these experiments were conducted with very small particles compared to the cylinder size $d \ll D$, we did not find a significant difference between size ratio 5 and 10 in our computations including friction. No dependence of the upstream particle velocity on the drag coefficient has been observed.

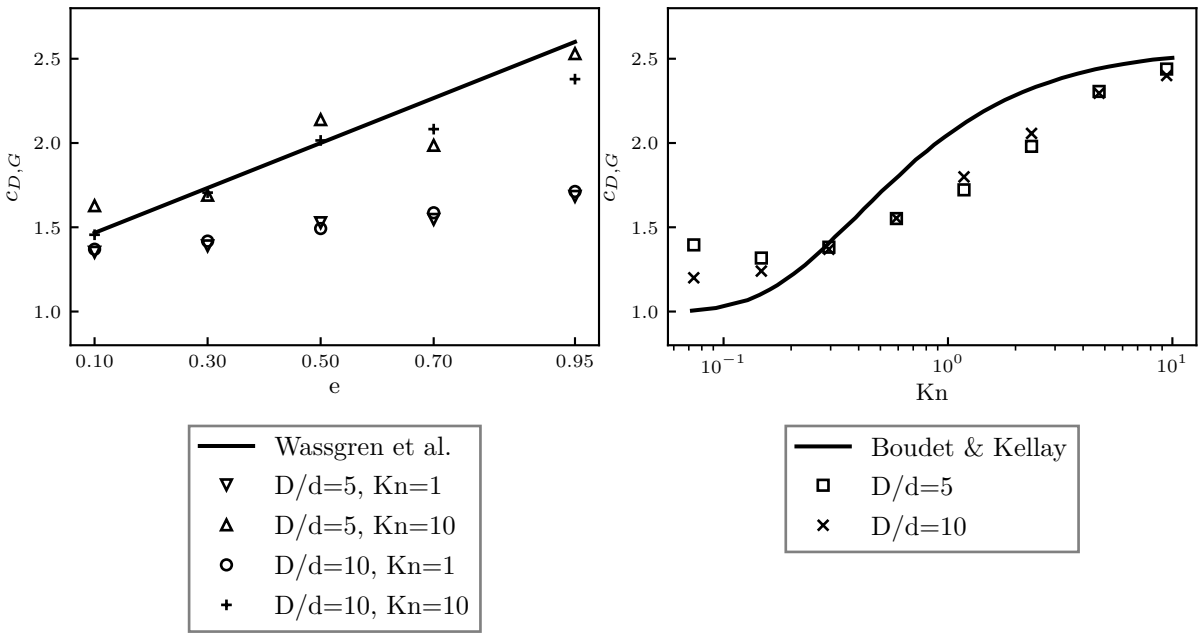

Figure 3.12 – Left: granular drag coefficient as function of coefficient of restitution e for non-interacting particles; solid line: prediction by Wassgren et al. [112]. Right: Granular drag coefficient as function of Kn for steel spheres (e=0.93); solid line: best fit of experiments by Boudet & Kellay [114].

3.8 Turbulent flow between two parallel plates

Finally, we need to validate turbulent flow properties for later computation of the swirled flow in Chap. 4. Turbulent flows are inherently more complex than laminar flows due to their chaotic nature. This is a difficulty in the main part of the flow, where turbulence models are needed. It is an even bigger difficulty near walls, where spatial resolution becomes an issue.

To check how our LBM approach behaves, we perform a wall resolved LES of the channel flow between two infinite plates at distance H. Even though this is a turbulent flow, this case is a classical test for all LES CFD codes and the expected solutions are well known [115, 116]. First we introduce the dimensionless wall distance and velocity

$$y^+ = \frac{yu_\tau}{\nu}, \quad u^+ = \frac{\bar{u}}{u_\tau}, \tag{3.17}$$

where y is the normal distance to the wall and u the mean velocity in flow direction. The skin friction velocity

$$u_\tau = \sqrt{\frac{\tau_w}{\rho}} \tag{3.18}$$

is defined by the wall shear stress τ_w. In the viscous sublayer, which is close to the wall, $y^+ < 5$, the flow is dominated by viscous stresses and turbulent stresses are negligibly small [33]. The dimensionless velocity is equal to the dimensionless wall distance

$$u^+ = y^+ \tag{3.19}$$

Further away from the wall, in the so-called log-law region $y^+ > 30$ the Reynolds shear stresses become dominant and we find the logarithmic relationship

$$u^+ = \frac{1}{\kappa} \log y^+ + C \tag{3.20}$$

with the von Kármán constant $\kappa = 0.41$ and $C = 5.0$. In between lies the buffer layer, which marks the transition between viscous and turbulence dominated regions. The high fidelity numerical data from Moser et al. [117] will be used as a reference to our simulations in this part of the flow. They also provide the different components of the Reynolds stresses tensor.

There are two characteristic Reynolds numbers for this problem - the bulk Reynolds number

$$\mathrm{Re}_{bulk} = \frac{\bar{u}(H/2)}{\nu}, \tag{3.21}$$

which measures the mean flow velocity $\bar{u}$ and the friction Reynolds number

$$\mathrm{Re}_\tau = \frac{u_\tau(H/2)}{\nu}, \tag{3.22}$$

which considers the wall shear stress. Furthermore, the skin friction coefficient

$$c_f = \frac{\tau_w}{\frac{1}{2}\rho\bar{u}^2}, \tag{3.23}$$

describes the dimensionless drag force exerted by the fluid onto the solid walls.

The grid spacing $\Delta y^+ = \frac{\Delta y^{\mathrm{LBM}} u_\tau}{\nu}$ in the LBM simulations is uniform throughout the domain except at the walls, where the boundary is placed in between two grid cells such that the first

fluid node is found at $\frac{1}{2}\Delta y^+$. This is different from finite volume codes, which continuously refine the mesh near the walls because smaller eddies appear at walls, requiring increased resolution. Such wall adapted meshes can not be used in waLBerla due to the block-structured mesh (see Sec. 2.6.3).

The flow is driven by an external fluid acceleration corresponding to the pressure gradient

$$a = -\frac{dp}{dx} = \frac{\tau_w}{H/2}, \tag{3.24}$$

which is imposed via the Luo force model (Eq. (2.97)). The simulation domain size is $\pi H/2, H, 0.289\pi H/2$ in streamwise, cross-stream and spanwise direction, respectively with periodic boundary conditions in x, z directions. Time averaging is performed over one turnover period $T = H/u_\tau$ and the initial transient time is $8\,T$. The flow is initialized with a one-seventh power-law velocity profile

$$u = u_{\max}\left(1 - \frac{|y - H|}{H}\right)^{1/7} \tag{3.25}$$

with random perturbation added to the mean velocity at time $t = 0$.

We examine three different LBM models for turbulent flows:

- The single relaxation time collision operator with a Smagorinsky type sub-grid scale turbulence model (BGK-SGS)
- The multi relaxation time collision operator, which is stabilized by relaxing third and fourth order moments according to the entropy condition (see Sec. 2.3.6)
- The cumulant relaxation model (see Sec. 2.3.4)

The biggest difference between these models is that BGK-SGS employs an explicit sub-grid turbulence model in the sense that the local shear viscosity is adjusted. In contrast, entropic and cumulant models do not modify the shear viscosity, but achieve increased stability by adjusting the higher order moments (entropic) or the relaxation of statistical independent quantities (cumulant). One might interpret these methods as "implicit" turbulence models.

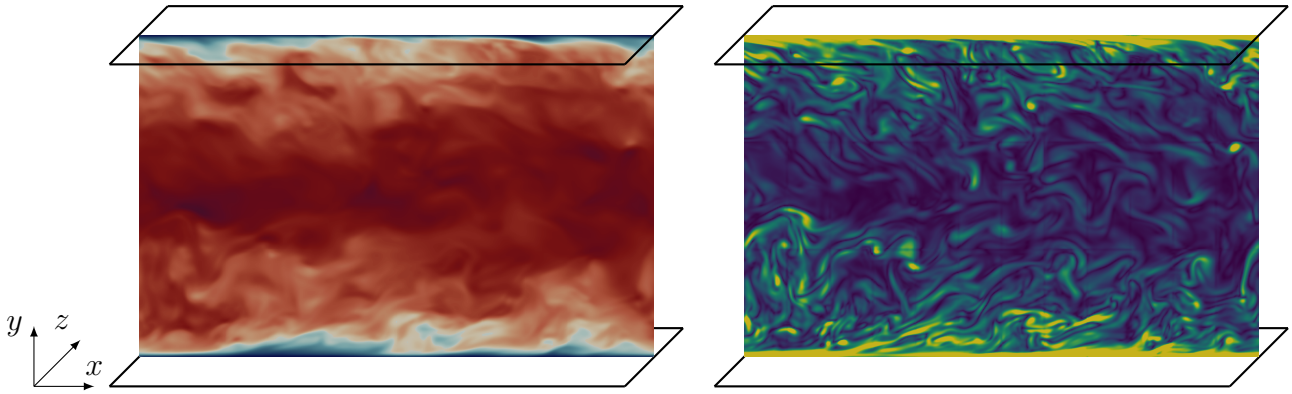

Figure 3.13 – Instantaneous snapshot of the velocity (left) and vorticity (right) magnitude of the turbulent flow between two parallel plates.

The dimensionless velocity and components of the Reynolds stress tensor are presented for a wall resolved grid spacing of $\Delta y^+ = 1$ in Fig. 3.14 and an underresolved grid with $\Delta y^+ = 6$.

v is the velocity component normal to the wall and w is the velocity component in spanwise direction. All simulation results are normalized by the friction velocity u_τ obtained from Moser et al.

At grid spacing $\Delta y^+ = 1$ all three methods recover the correct mean velocity profiles and Reynolds stresses. Deviation in the simulated bulk velocity and wall shear stress are below 1% and 3%, respectively compared to the reference from Moser et al. This is a remarkable result considering that the LBM code does not use mesh refinement near walls. Results deteriorate for the coarser grid spacing $\Delta y^+ = 6$. Nonphysical stresses appear for the BGK-SGS model and the bulk velocity is significantly underestimated for the entropic model. The cumulant method presents good velocity profiles but the predicted wall shear stress is too low. At even coarser grid resolution the fluctuations in the BGK-SGS model cause the simulation to become unstable, whereas the entropic and cumulant methods were able to robustly simulate turbulence up to a grid spacing of $\Delta y^+ = 6$.

		$\Delta y^+ = 1$			$\Delta y^+ = 6$		
	Reference	BGK-SGS	Entropic	Cumulant	BGK-SGS	Entropic	Cumulant
Re_{bulk}	10000	10039	10042	10057	10329	9047	10174
Re_τ	543	551	555	557	454	512	456
$c_f \times 10^{-3}$	5.908	6.020	6.011	6.131	3.991	6.432	4.046

Table 3.1 – Comparison of bulk Reynolds number Re_{bulk}, friction Reynolds number Re_τ and friction coefficient c_f for different resolutions against numerical data from Moser et al. [117]

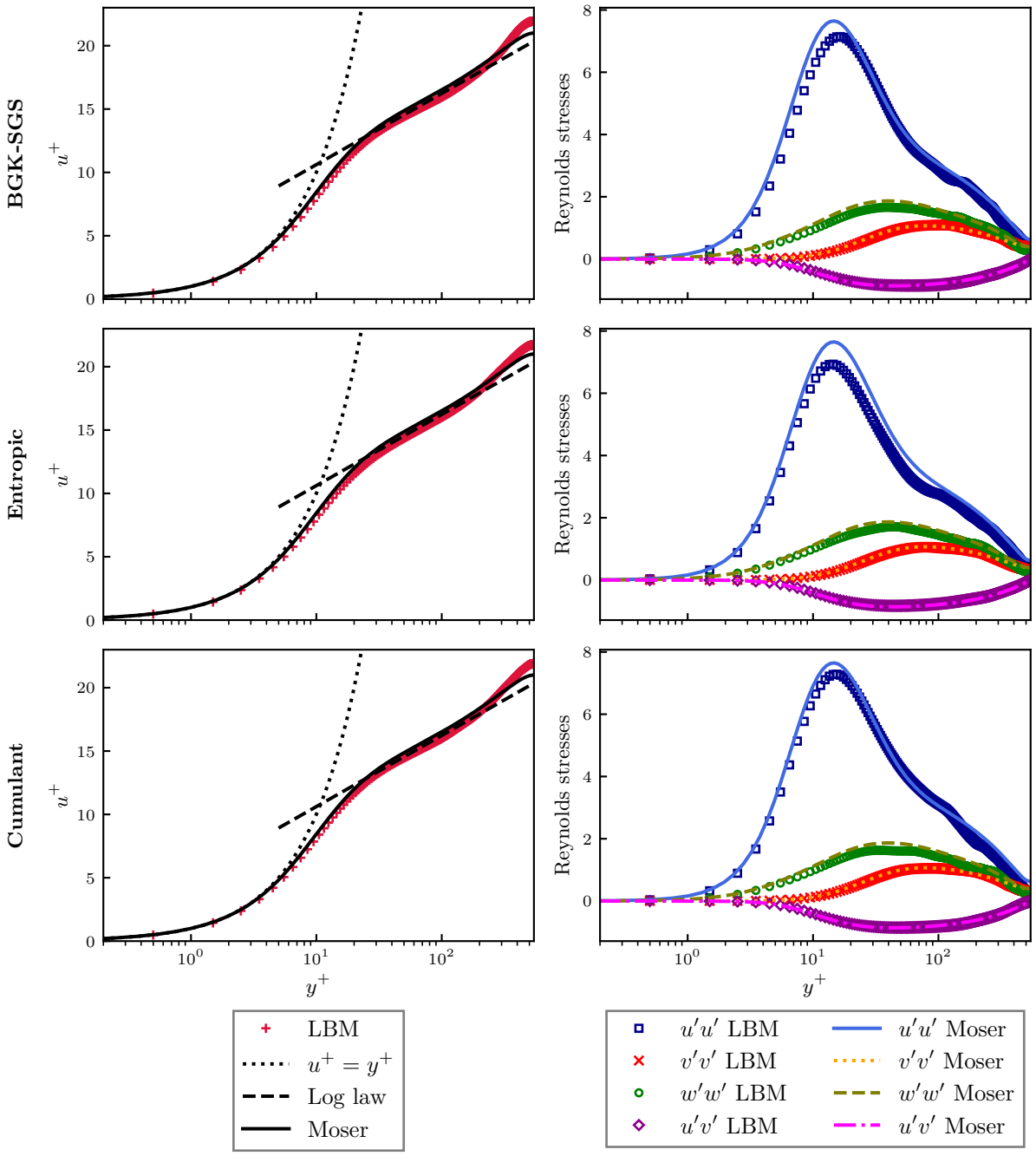

Figure 3.14 – Velocity profile and Reynolds stresses for a flow between two infinite parallel plates at $\mathrm{Re}_\tau = 543$ and uniform grid size $\Delta y^+ = 1$. The BGK collision operator with Smagorinsky sub-grid model, entropic stabilized MRT and the cumulant relaxation method are compared to high fidelity numerical results from Moser et al. [117]

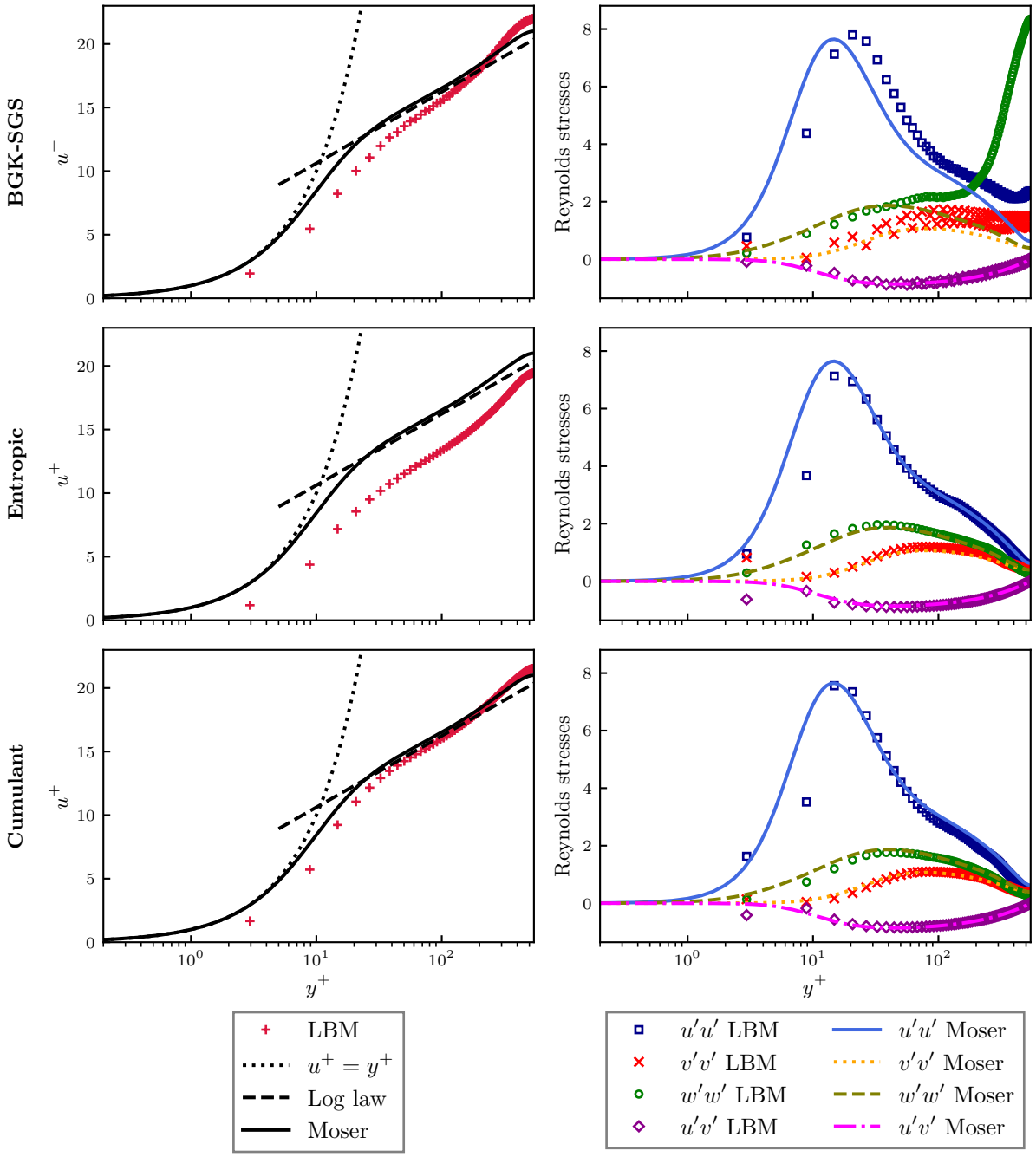

Figure 3.15 – Velocity profile and Reynolds stresses for a flow between two infinite parallel plates at $\mathrm{Re}_\tau = 543$ and uniform grid size $\Delta y^+ = 6$. The BGK collision operator with Smagorinsky sub-grid model, entropic stabilized MRT and the cumulant relaxation method are compared to high fidelity numerical results from Moser et al. [117]

3.9 Conclusion

We have presented the capabilities of the LBM to solve fluid problems from the Stokes regime up to turbulent flows, even near walls. In the realm of low Reynolds numbers the LBM has difficulties maintaining high accuracy, especially when characteristic time scales are small. We observed that a fine resolution is necessary to compete with methods like the FCM, which is designed to deliver high accuracy especially in the Stokes regime. Attention needs to be taken to ensure that the lattice relaxation frequency does not approach zero. Generally values lower than $\omega = 0.4$ should be avoided. The TRT model shows an advantage over th BGK model in terms of accuracy for most of the tested configurations. We use $\Lambda = 3/16$ to find the correct velocity profile in channel flows and $\Lambda = 1/4$ for highest stability.

The particle response to a sudden change in fluid velocity is well captured by the LBM except when the particle time scale is small and the relative density is high. Similarly, the unsteady response to an oscillatory force becomes worse for higher frequencies. The Basset-History force is present, but difficult to recover accurately. Increasing the spatial resolution improves the results for the oscillating particle, but has little impact on the response to a sudden change in velocity. The Segré-Silberberg effect is well predicted for a spatial resolution of 10 grid cells per sphere diameter.

Three different LBM approaches in waLBerla have been generated using lbmpy (BGK-SGS, entropic and cumulant relaxation) for computing turbulent flows using an LES-type approach. The turbulent flow between two parallel plates has been tested and compared to the DNS of Moser et al. [117], which is the reference in this field. All three are able to accurately predict mean velocity and turbulent flow quantities with a fine resolution of the viscous sublayer. For underresolved grids the entropic and cumulant methods exhibit better stability.

Chapter 4

Comparison among Lattice Boltzmann and finite volume solvers for swirled flows

Contents

This chapter corresponds to a common CERFACS / IMFT / EM2C work on a swirler developed and tested at EM2C. It was submitted to Computer and Fluids in 2020 under the reference [118]. We will present the experimental setup and briefly introduce the solvers AVBP, ProLB and waLBerla*. The numerical results are compared to mean and RMS velocities of PIV measurements and their power spectrum is compared to LDV measurements for the confined flow. The three codes are benchmarked in terms of their computational efficiency and parallel scalability. Lastly, we perform some additional simulation with* waLBerla *to check the mesh convergence and find the velocity profile of the unconfined configuration.*
All experimental data presented in this chapter have been provided by EM2C at the start of this study. Numerical simulations using AVBP were conducted by Andrea Aniello and simulations using ProLB were conducted by Paul Werner, whereas my main contribution was to perform simulation using waLBerla*. The choice of numerical methods, mesh resolution and the physical interpretation have been carved out together as a team.*

4.1 Introduction

The question of the efficiency of CFD solvers is an issue which has virtually disappeared for classical RANS (Reynolds Averaged Navier-Stokes) methods but remains essential when it comes to Large Eddy Simulation approaches [119, 120] as pointed out recently by Löhner [17]. Arguing that a certain class of CFD methods is the fastest to solve LES critical problems is a game played by multiple teams worldwide: in most cases, these discussions focus on the theoretical reasons which should make such or such approach faster than others for LES. However, the actual speed of CFD solvers for LES does not depend only on the theoretical efficiency of the method: in most cases, the mesh management, the boundary conditions, the sub models, the parallel implementation of the method also play critical roles so that the determination of an exact CPU efficiency is difficult before running real simulations. Furthermore, when simulations are run, the comparison itself between methods becomes difficult: in many cases, each author runs his or her own code and does not try to compare fully with competing methods. Workshops are commonly organized to compare methods but their conclusions are rarely clear because the collaboration to ensure a proper comparison remains difficult to set up (see for example [121] for such a workshop on compressible methods for LES of turbomachinery).

This chapter compares three LES solvers (Tab. 4.1) which were all run by the same group of people at IMFT and CERFACS: an incompressible finite volume solver: AVBP_{pgs} and two Lattice Boltzmann (LB) codes: ProLB and waLBerla. All computations were performed on the same machines, with the same number of processors and a systematic comparison was organized to ensure a fair evaluation of methods. The target configuration was the internal turbulent flow in a swirling burner but all cases correspond to a non reacting situation. Unlike many previous studies, the present one focuses on an internal flow, at moderate Reynolds numbers, as found in combustion chambers and not on external flows as found in aerodynamic and aeracoustic studies. Experiments were performed by the EM2C laboratory and include enough detailed data to evaluate the precision of the solvers in terms of pressure losses and full mean and RMS velocity fields.

Code	**Formulation**	**Method**
AVBP_{pgs}	Incompressible	Finite volume (Galerkin)
ProLB	Athermal	Lattice Boltzmann
waLBerla	Athermal	Lattice Boltzmann

Table 4.1 – Presentation of solvers used for LES simulations

Of course, the first difficulty in such an exercise is the definition of the rules of the game. In the present case they can be explained as follows: "for each code, build a numerical setup which provides a minimal accuracy in terms of flow field resolution (pressure loss as well as mean and RMS velocity profiles within experimental accuracy levels) and compare the CPU efficiency". Since multiple solvers are used, with different meshes, different algorithms and different submodels, the notion of minimal accuracy remains arbitrary: here, long discussions between CFD and experimental teams members have lead to a minimum quality which was expected from the match between experimental and LES results in terms of average and RMS velocity fields for multiple locations. This was used for the three solvers to determine the mini-

mum grid size required to reach this sufficient level of agreement. Once all solvers were found to provide comparable agreement with the experimental data (taking into account experimental uncertainties), CPU efficiencies were determined. This procedure still contains a clear level of arbitrariness that authors do not want to deny. The error bars expected on the results are certainly significant and of the order of tens of percents.

4.2 Experimental setup

The configuration (Fig. 4.1) was designed to analyze the response of swirled flames to flow rate modulations in [122, 123].

Dry air is injected from two diametrically opposed apertures at the bottom of a plenum. The flow crosses a grid and a honeycomb to break the largest turbulent scales. A convergent section produces a top-hat laminar velocity profile with a boundary layer of about 1 mm thickness that was characterized by a hot wire probe (Dantec Dynamics - Probe 55P16 with a mini-CTA 54T30). The diameter of this section is $D = 22$ mm and the bulk flow velocity is fixed to $u_b = 5.44 \pm 0.05$ m s^{-1} corresponding to a Reynolds number $\mathrm{Re}_D = 7\,620$ at room temperature $T = 300$ K. The pressure drop with respect to ambient conditions is recorded in front of the hot wire probe with a differential pressure gauge and indicates $\Delta p = 335 \pm 15$ Pa. The setup was originally designed to analyze effects of geometrical modifications of the injector on flame dynamics and the burner replaceable components are represented in Fig. 4.1. In the configuration explored, the radial swirling vane consists of $n = 6$ cylindrical tangential inlets of diameter $D_s = 6$ mm with an offset $H = 6$ mm as indicated in Fig. 4.1c. The flow leaves the swirler into a central injection tube. The diameter of this tube is $D = 22$ mm, over a first section of length $\delta_1 = 16$ mm, followed by a central insert of length $\delta_2 = 34$ mm and diameter $D_0 = 20$ mm. A central rod of diameter $d = 6$ mm ending with a cone of diameter at the top $C = 10$ mm is inserted in the injection tube. The distance between the swirler exit and the combustion chamber back plane is here fixed at $\delta = \delta_1 + \delta_2 = 50$ mm. The central rod protrudes inside the combustion chamber and the distance between the top of the cone and the backplane is 1.5 mm. The combustion chamber, made of 4 transparent quartz windows, has a 82 mm squared cross-section and length 150 mm. It is extended by a nozzle with a square inlet section and a circular outlet section of diameter 70 mm. Transition between this square to circular sections is made over a 104 mm length. This device ensures that there is no reverse flow at the setup outlet. The cartesian system of reference used through the paper is presented in Fig. 4.2: z corresponds to the symmetry axis of the injector, while the plane defined by axes x and y corresponds to the backplane of the combustion chamber ($z = 0$ mm).

Particle Image Velocimetry (PIV) is used to measure the cold flow velocity fields. For these measurements, the flow is seeded with small oil droplets of diameter 1-3 μm. PIV data are gathered on both axial and transverse planes within the combustion chamber. The first is identified by z and x directions ($y = 0$ mm), while the second one is parallel to the burner backplane and located at $z = 3.5$ mm. No PIV data is available at lower axial coordinates. The PIV system consists of 2×400 mJ Nd:YAG laser doubled at 532 nm operated at 10 Hz and a 2048×2048 pixels CCD camera (Dantec Dynamics, FlowSense EO 4M). Two different optical setups are used with a time interval between the two laser pulses $\Delta t = 10$ μs and a pixel pitch of 27.88 pixels mm^{-1} for measurements in the axial plane and $\Delta t = 25$ μs and a pixel pitch of 40.14 pixels mm^{-1} for measurements in a transverse plane. Eight hundred images are taken to assure the convergence of the mean and RMS values of the velocity field, which is computed from the cross-correlation of the PIV images by a three passes window deformation technique

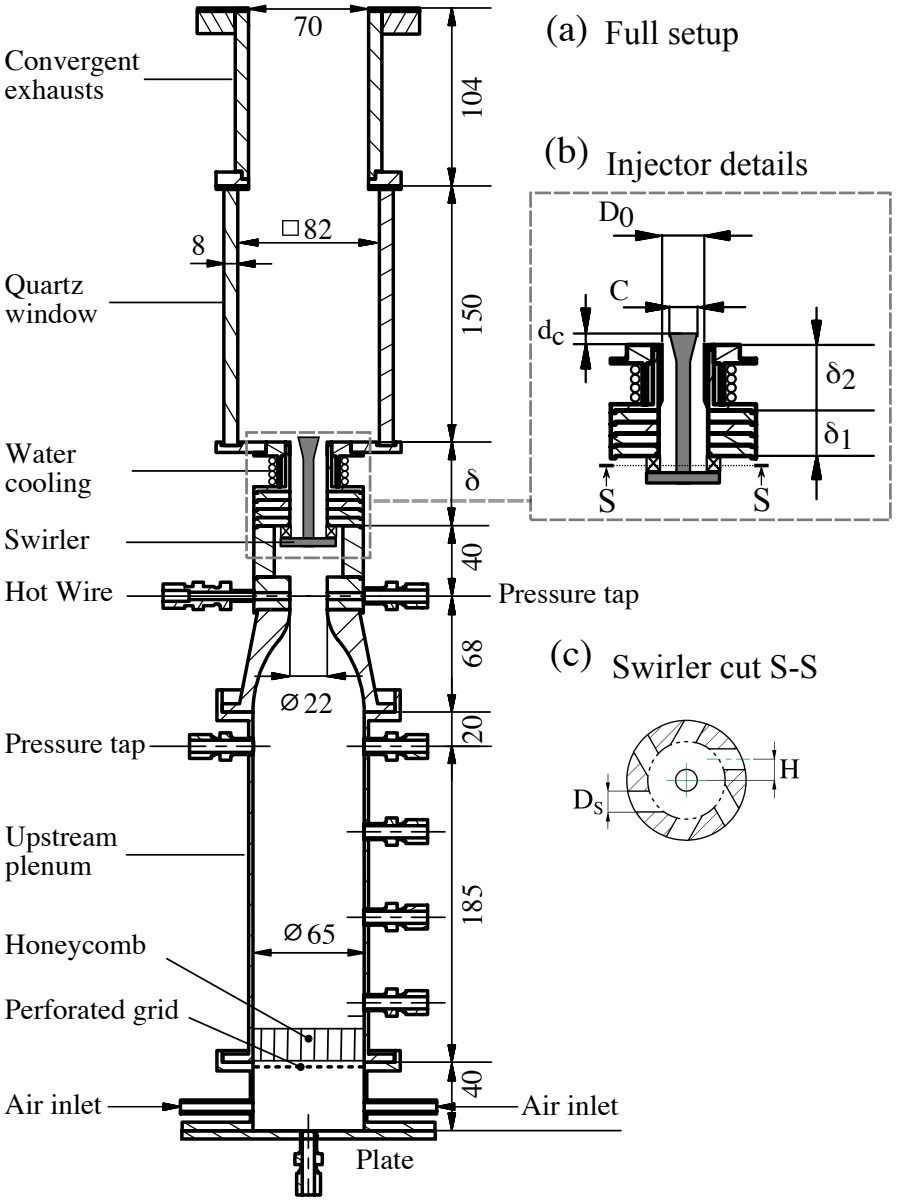

Figure 4.1 – Experimental setup with detailed representation of the injector region and swirler geometry. All dimensions in mm.

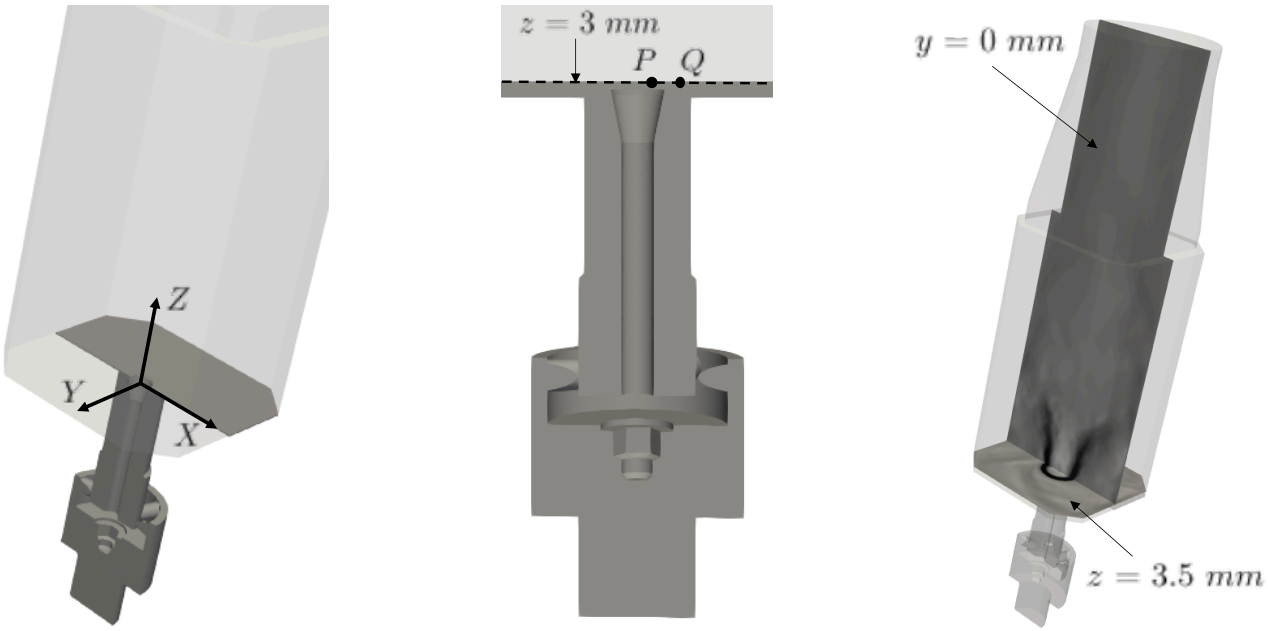

Figure 4.2 – Presentation of cartesian system of reference (left). Identification of points P and Q used for modal analysis (center) and representation of PIV transverse and axial planes of investigation (right)

(from 64×64 pixels to 16×16 pixels interrogation areas), with an uncertainty of 0.1 pixels on the calculated displacement.

The measurements are completed by Laser Doppler Velocimetry (LDV) to capture the time resolved velocity profiles at $z = 3$ mm above the top central insert (see Fig. 4.2). The Power Spectral Density (PSD) of the axial velocity is calculated to detect the presence of potential hydrodynamic or acoustic modes. To ease optical access the combustion chamber is removed for those latter measurements and LDV data are collected in unconfined configurations. Two laser beams at $\lambda = 514.5$ nm (green) allow to probe the axial velocity. Two other beams at $\lambda = 488$ nm (blue) are used to measure the velocity component along x direction. The data collection rate is always greater than 10000 s^{-1} and for each measurement point at least 250000 particles are considered, in order to obtain fully converged mean and RMS values for all components of velocity. The statistical bias is corrected by the transit time of each particle. The analysis of time traces and PSD of these signals does not reveal any specific coherent structures associated to helical flow instabilities.

4.3 Presentation of solvers

4.3.1 High-order finite volume solver

AVBP is a multi-species LES explicit solver for Navier-Stokes compressible equations developed at CERFACS (www.cerfacs.fr/avbp7x). This Cell-Vertex (CV) high-order Finite Volume (FV) code [124, 125] is able to handle structured, unstructured and hybrid grids in both two and three space dimensions. It is a world standard code to compute turbulent reacting flows in combustion chambers [126] or explosions in confined domains [127]. A critical aspect of compressible codes is the treatment of numerical boundary conditions where acoustic reflections must be controlled

to avoid spurious phenomena. In order to fulfill those requirements, AVBP exploits Navier-Stokes Characteristic Boundary Conditions (NSCBC) [128, 129, 130, 131].

Like any explicit compressible code, AVBP tends to be less efficient for low Mach number simulations. The problem arises from the large disparity between time scales associated to sound waves propagation and convection: the CFL stability condition imposed by the sound speed is uselessly severe with respect to the limit established by convection alone, resulting in an unnecessarily small time step. In order to overcome this limitation and to be representative of another class of FV solvers, which use incompressible or low-Mach number formulations, a modified version of AVBP, called here AVBP_{pgs} is used to remove the acoustic time step limitation: the governing equations solved are manipulated according to the Pressure Gradient Scaling (PGS) technique [132]. PGS rescales the pressure gradient in the momentum equations to reduce the computational sound speed, so that the time step is not limited by the true sound speed which is irrelevant. The PGS methodology is limited to low-speed incompressible flows like the present configuration. Overall, the procedure is equivalent to the α-transformation developed in [133], but with the advantage of both easier implementation and wider applicability. Since the Lattice Boltzmann solvers are used here in their athermal weakly compressible form, it seems reasonable to utilise AVBP_{pgs} which uses similar assumptions.

4.3.2 Lattice-Boltzmann solvers

A key difference between FV and LBM algorithms is that the FV solver uses the same time step in the whole computational domain, whereas in LBM the time step depends on the level of refinement. A cell on the coarser grid level has twice the size but also the time step is two times bigger compared to the finer level. To take this effect into account we generally use the term Equivalent Fine Nodes (EFN) which counts cells on coarser levels L as a fraction of the finest level (Eq. (4.1)). This quantity reflects the workload equivalent of a mesh using only the minimal mesh size $\min(\Delta x)$ and is therefore more suitable for comparison between the codes.

$$\text{EFN} = \sum_{L} N_{\text{nodes on L}} \left(\frac{1}{2}\right)^{L-1} \tag{4.1}$$

Another consequence is that the main part of the workload is generated by the finest level in the domain. In order to do a fast computation it is essential to minimize the regions with minimal cell size. The differences between the two LBM meshes are summarized in Tab. 4.2. The ProLB algorithm typically needs fewer EFN to accurately resolve a given problem, whereas the approach of waLBerla generates a non negligible amount of excess cells, that are not part of the fluid domain but are computed anyway.

ProLB

ProLB is a commercial suite of tools which emerged from LaBS and CLIMB [134] French research projects carried out by a consortium of industrial companies, universities, research laboratories and institutes. Its inherent massively-parallel solver includes an octree mesher which efficiently handles both complex geometries [135] and multi-resolution refinement layers [136].

In the present case, a modified version of the commercially available ProLB software is used. The numerical resolution of the Lattice-Boltzmann equation is performed through the D3Q19 lattice with a Hybrid Recursive Regularized (HRR) collision operator proposed by Jacob *et al.*

Code	ProLB	waLBerla
Number of nodes [M]	26.3	39.3
Number of fluid nodes [M]	26.3	30.2
Octree level distribution fluid nodes [%]	[67, 25, 5, 3, 0, 0]	[59, 24, 13, 1.9, 1.5]
Equivalent Fine Nodes [M]	21.4	29.8
Equivalent Fluid Fine Nodes [M]	21.4	22.6

Table 4.2 – Total number of nodes and level distribution of fluid nodes in LBM solvers is determined by grid size and spatial layout of refinement zones.

[137] which enhances better accuracy, stability and convergence for high-turbulent flows than the classical Bhatnagar-Gross-Krook (BGK) collision model [3] by filtering out the spurious and non-hydrodynamic components that could be amplified at grid transitions. Moreover, to accurately handle mesh refinement, a Direct-Coupling (DC) algorithm is employed instead of the classical overlapping method [138]. By ensuring mass and momentum conservation at the transition nodes, a singular equilibrium distribution function is computed to recover the missing distributions at both coarse and fine sides. This combination of the HRR collision model and the DC algorithm offers better accuracy and locality in complex configurations.

The boundary nodes need a specific treatment in LBM approaches: since the mesh is completely cartesian, an immersed boundary condition is implemented to handle the solid walls [139] allowing first the automatic generation of the mesh and second to flag the interface nodes. Then, a Grad's approximation algorithm combined with a Dirichlet condition is chosen to treat the walls nodes and to recover the missing populations at the boundary nodes. This yields a more stable and accurate approach than the well-known interpolated bounce-back [140].

Thanks to the octree multi-resolution mesher, the ultimate grid is built upon a static adaptive refinement strategy [141] where the considered sensor is the dissipation of kinetic energy [142]. From an initial coarse simulation, the time-averaged field of this sensor is computed. Therefore, a smoothed iso-volume based on a lower case-dependent threshold of the sensor yields a finer resolution domain which is directly reintroduced in the octree mesher. Thereby, this process is repeated twice in order to predict pressure losses and optimize the number of fluid nodes by refining only the relevant areas and minimizing computational costs.

4.3.3 Numerical setups

The three solvers were applied to the same swirler geometry of EM2C but they employ different meshes (Tab. 4.3): AVBP_{pgs} uses body-fitted unstructured tetrahedral mesh with 18.1 M cells in total, while ProLB relies on cartesian unstructured mesh, offering a local refinement possibility but requiring up to 26.3 M grid elements, which amounts 21.4 M EFN to represent the same geometry. This tendency is exacerbated in waLBerla, where the structured cartesian mesh is only able to refine whole blocks of the mesh, which leads to 39.3 M, or 22.6 M EFN cells overall.

A detailed representation of each grid, including swirler, injector and near-backplane region, is displayed in Fig. 4.3. It exhibits an axial cut for each code to show the local mesh structure: the swirler region has the highest resolution to predict the correct velocity field and pressure

Code	Topology	Cell type	min(Δx) [µm]	Total elements [M]
AVBP_{pgs}	Unstructured	Tetrahedral	80	18.1
ProLB	Unstructured	Cubic	110	26.3 (21.4*)
waLBerla	Structured	Cubic	110	39.3 (22.6*)

Table 4.3 – Overall description of mesh parameters for the three solvers (* *marks the number of Equivalent Fine Fluid Nodes (EFFN))*

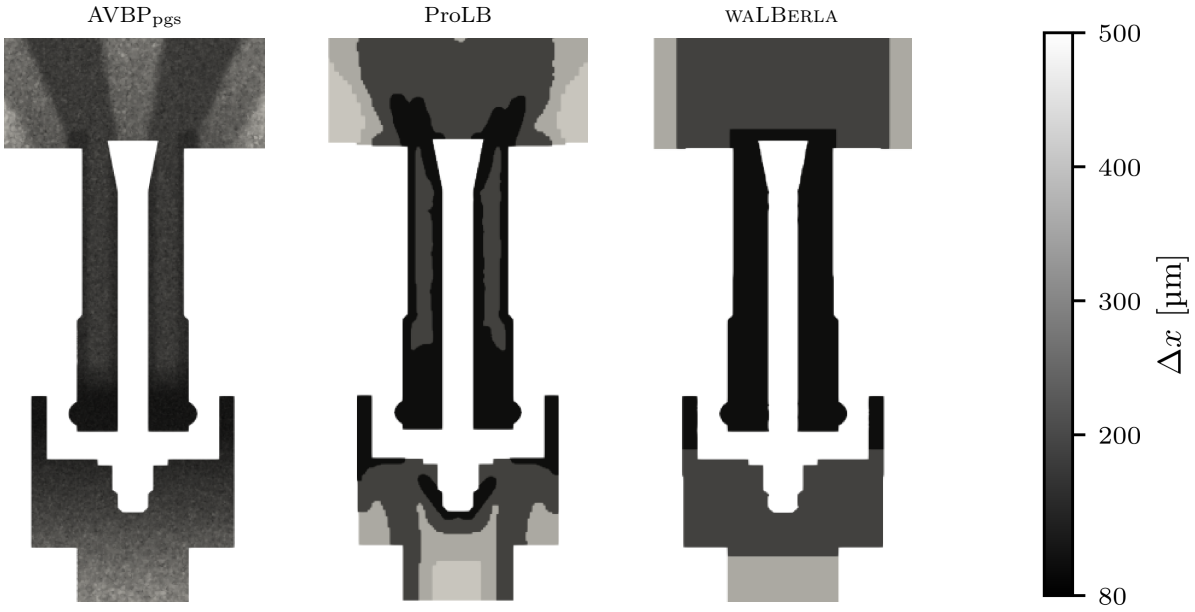

Figure 4.3 – Mesh comparisons via Δx contour maps for the three solvers: AVBP_{pgs}, ProLB, waLBerla. Differences among structured and unstructured grids, as well as between cubic and tetrahedral elements are highlighted.

losses.

In this region AVBP_{pgs} adopts a minimum cell parameter (Δx) of 80 µm that increases along z up to the burner backplane with an average $\Delta x \approx 180$ µm. While ProLB mesh is refined through adaptive unstructured blocks of minimal mesh size $\Delta x = 110$ µm, waLBerla uses a block of constant $\Delta x = 110$ µm in both swirler and injector. With these meshes, the time steps are adjusted to obtain CFL numbers based on the maximum convective velocity of the order of 0.1 for all codes.

AVBP_{pgs} adopts Lax-Wendroff scheme [143], second-order in both space and time. The CFL number (based on the modified sound speed) is set to 0.9. Temperature and volumetric flow rate are fixed at the inlet, while ambient pressure (101325 Pa) with a proper relaxation coefficient is imposed at the outlet. Although the temperature equation is solved in AVBP_{pgs}, the impact on its computational speed is assumed to be marginal. The SIGMA model is used for subgrid Reynolds stresses [144]. Both turbulent Prandtl number Pr and Schmidt number Sc are fixed to 0.6 and only one inert species representative of air is computed. The PGS parameters are set to obtain a maximum computational Mach number of 0.3.

While ProLB employs a HRR collision operator combined with a DC mesh transition algorithm, waLBerla is using a classical BGK collision model. Both solvers impose a one-seventh power law velocity profile at the inlet to match the experimental flow rate and a constant pressure of 1 bar at the outlet. The geometry is extended in axial direction at inlet and outlet to dampen non-hydrodynamic reflection waves inside the domain. Walls are treated differently: ProLB uses a Grad's approximation and waLBerla a bounce-back scheme to treat the "missing populations".

Since acoustics do not contribute significantly to the flow behavior, the non-dimensionalized Newtonian sound speed c_s^* is artificially minimized by being cautious that the maximal Mach Number does not exceed the critical value of 0.4 [145]:

$$\mathrm{Ma}_{\max} = \frac{u_{\max}}{c_s^*}\frac{\Delta t}{\Delta x} < 0.4. \tag{4.2}$$

This requirement is similar to the CFL condition for classical Navier-Stokes numerical schemes [146]. This process intends to increase the time step to its maximal value and therefore allows to lower the computational time while the accuracy is still conserved.

LES in ProLB are performed using a Shear-Improved Smagorinsky turbulence model (LES-SISM) [147] which accounts for the dissipation of the unresolved turbulent scales through an eddy viscosity. waLBerla relies on the SGS turbulence model described in Sec. 2.3.5.

4.4 Comparison with experimental data

This section presents a comparison of experimental and numerical results to validate the entire set of simulations. The results of all three codes are averaged over a minimum of 12 flow-through times (τ_t) to obtain fully converged averaged solutions which are time-independent in terms of mean and RMS results. The flow-through time, i.e. the physical time taken for a flow element to travel through the chamber in the high velocity zone at 8 $\mathrm{m\,s^{-1}}$, equals $\tau_t = 10$ ms for this configuration.

The first quality indicator for swirler flows is the pressure loss Δp through the swirler (Tab. 4.4) which controls its performances in a real engine. Δp is calculated between the pressure tap location (see Fig. 4.2) and the outside ambient pressure.

	Δp (Pa)
Experiment	335 ± 15
$\mathrm{AVBP_{pgs}}$	330
ProLB	368
waLBerla	313

Table 4.4 – Injector head pressure losses due to swirler

The agreement of $\mathrm{AVBP_{pgs}}$ with the experiment is slightly better than for LBM codes, as expected for a code which uses body-fitted meshes. ProLB and waLBerla predict a Δp of 368 Pa and 313 Pa, respectively above and below the experimental confidence interval. To qualify codes, measuring the pressure loss is not sufficient, however, and the next sections focus on a detailed analysis of the velocity fields.

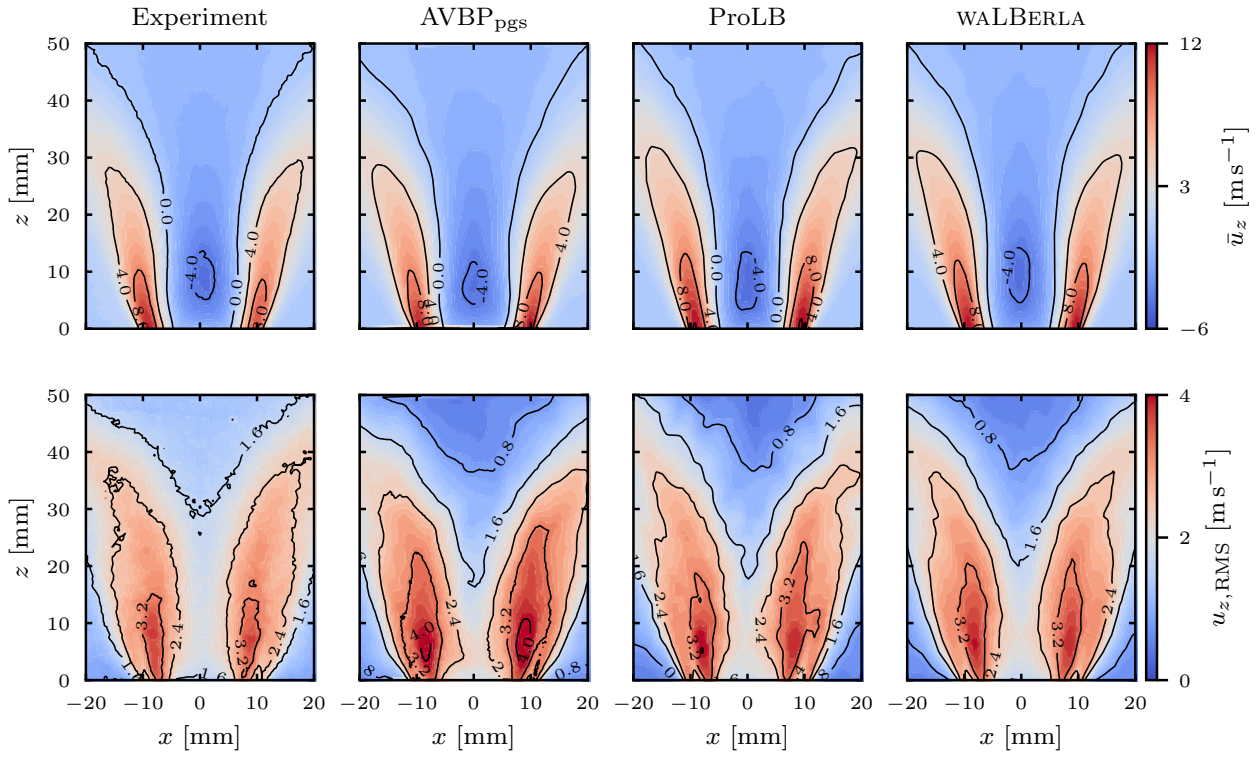

Figure 4.4 – Contour map comparison of experimental and numerical results of the axial (z) component of the velocity on the axial plane. First row exhibits the mean velocity field $\bar{u}_z$, while second row displays the RMS distributions $u_{z,\mathrm{RMS}}$

4.4.1 PIV

Velocity profiles are compared on two planes: the axial zx plane and the transverse plane $z = 3.5$ mm (see Fig. 4.2). In the first case data are displayed over a 40×50 mm^2 rectangular window symmetrically located with respect to the z axis. For the second, results are presented over a 40×40 mm^2 squared area centered in the middle of the combustion chamber with sides oriented along x and y directions.

Furthermore local one-dimensional, velocity profiles extracted at constant z are also retrieved from both PIV data and simulations.

Axial plane

Fig. 4.4 exhibits two rows of images: the top row shows the mean axial velocity component $\bar{u}_z$. The second one shows its RMS noted $u_{z,\mathrm{RMS}}$. From left to right experimental data and numerical results are displayed, as specifically reported on top of each plot.

The experimental mean velocity contour map of Fig. 4.4 highlights a large Inner Recirculation Zone (IRZ), typical of high swirling flows. This region of negative axial velocity is created by the vortex breakdown and is delimited by iso-velocity lines at $\bar{u}_z = 0$ m s^{-1}. Moreover two high velocity branches develop in the wake of the injector annular channel, identified by isolines at 8 m s^{-1}.

The comparison with numerical results show that the three solvers properly capture the flow characteristics, for both width and intensity of the IRZ. Minor differences can be highlighted:

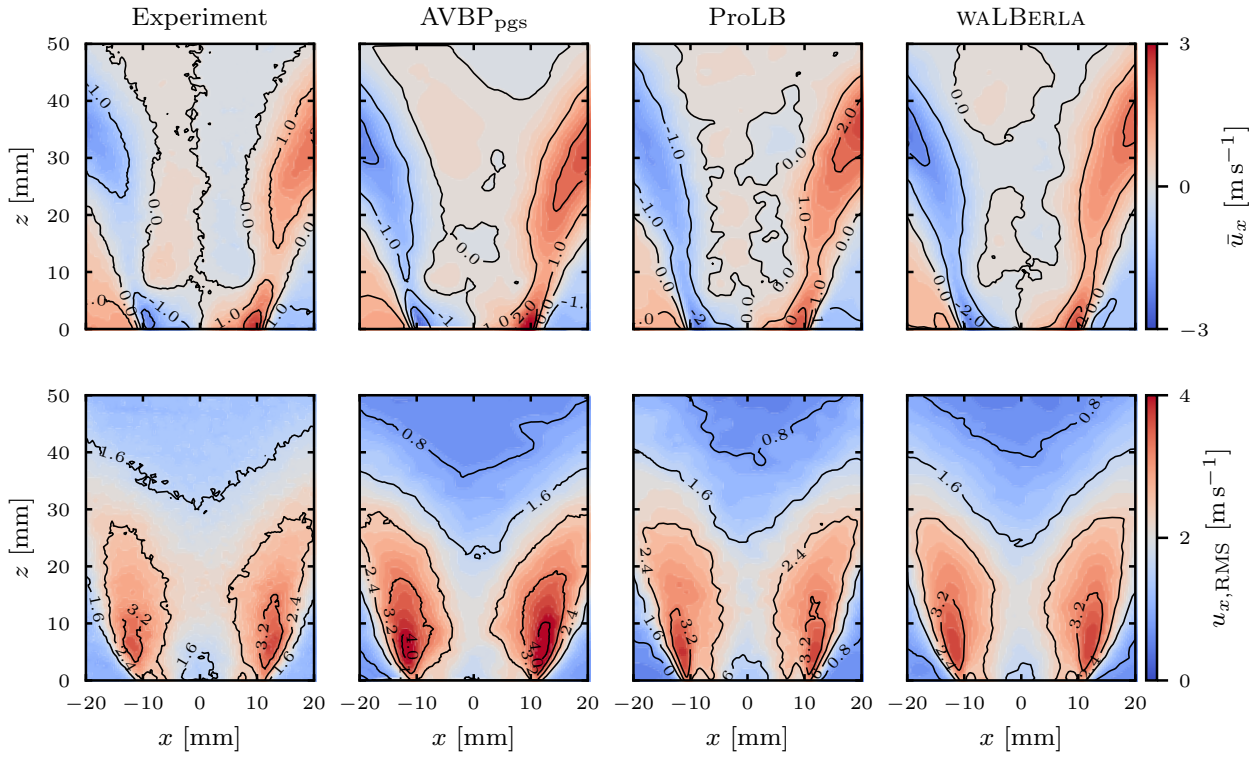

Figure 4.5 – Contour map comparison of experimental and numerical results of the horizontal (x) component of the velocity on the axial plane. First row exhibits the mean velocity field $\bar{u}_x$, while second row displays the RMS distributions $u_{r,\mathrm{RMS}}$

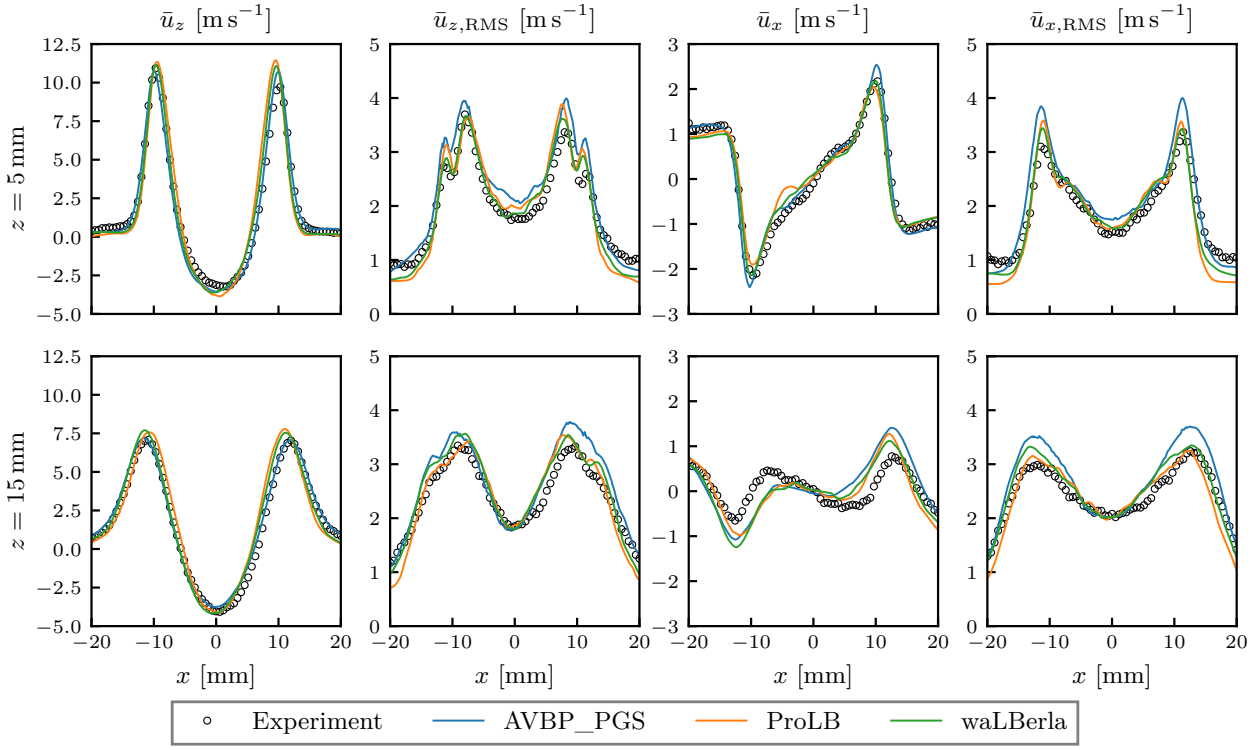

Figure 4.6 – Mean velocity profiles and related RMS of $\bar{u}_z$ and $\bar{u}_x$ for different solvers with. Obtained at constant axial coordinate on the axial plane. First and second rows correspond to $z = 5$ mm and $z = 15$ mm, respectively.

the extension of the high mean velocity regions is slightly overestimated by LBM codes, where 8 m s^{-1} and 4 m s^{-1} isolines develop further downstream than in experimental data. In addition, RMS maps obtained with the three solvers highlight less regular contour plots, potentially linked to averaging times which are much smaller in the LES than in the experiment. AVBP$_{\mathrm{pgs}}$ shows slightly higher RMS with respect to other codes and experiment, especially in the high velocity region.

The horizontal component (x) results (Fig. 4.5) confirm the axial component conclusions of Fig. 4.4: the three solvers are able to match the experimental results and all solvers provide results which are within the experimental range of precision for PIV results (typically 0.3 m/s here). However Fig. 4.4 and 4.5 are not sufficient to provide an appropriate evaluation of the precision: it is worth considering one-dimensional profiles showing local $\bar{u}_z$ and $\bar{u}_x$ velocity profiles sectioning the axial plane at specific z locations.

Fig. 4.6 displays mean and RMS profiles of $\bar{u}_z$ and $\bar{u}_x$, where in the first row profiles are extracted at $z = 5$ mm and in the second one at $z = 15$ mm.

First, the $\bar{u}_z$ profile reveals that experimental data are not exactly symmetric with respect to the z axis: the left-hand velocity peak is higher than the other, while simulations do not show the same differences. Numerical predictions show that at both z coordinates, the slope and the minimum of the axial velocity profile, which define the IRZ structure, are correctly represented. On the other hand the maximum axial velocity values at $z = 15$ mm are slightly overestimated by LBM codes by roughly 0.5 m s^{-1}, which corroborates the little discrepancy highlighted in Fig. 4.4. $\bar{u}_x$ profiles are generally hard to match in swirled flows since the mean velocity intensity is comparable to its RMS values. This emphasizes the fidelity of all simulations put

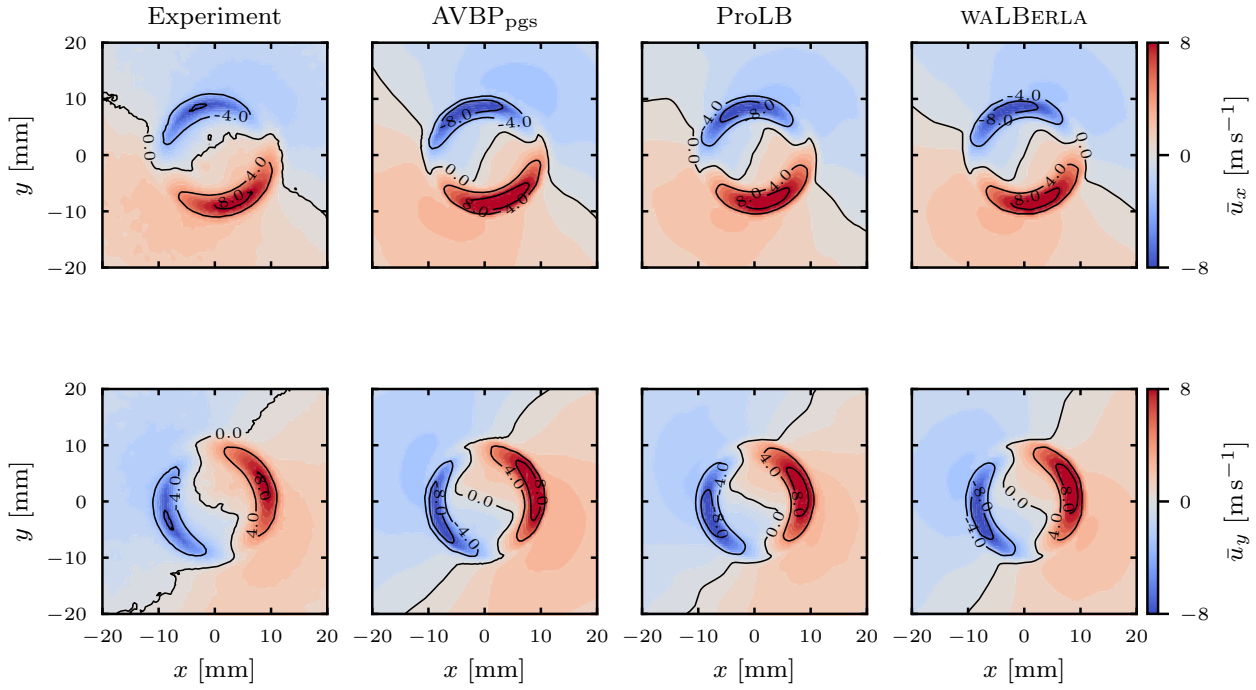

Figure 4.7 – Contour map comparison among experimental and numerical results on transverse plane. The first row exhibits mean velocity component $\bar{u}_x$, while second row displays the mean velocity component $\bar{u}_y$

in place. In fact the maximum difference between experimental data and simulations is only of the order of few tenths of meters per second. Furthermore, the RMS profiles for both $\bar{u}_z$ and $\bar{u}_x$ at both z coordinates confirm the AVBP$_{pgs}$ little overestimation at peak velocity locations, which in any case remains largely within the experimental accuracy margin.

Transverse plane

Fig. 4.7 displays $\bar{u}_x$ and $\bar{u}_y$ mean velocity profiles on the transverse plane $z = 3.5$ mm.

The good agreement between computational and experimental velocity fields confirms the previous findings. Only a slight overestimation of absolute maximum and minimum for both $\bar{u}_x$ and $\bar{u}_y$ can be pointed out looking at iso-velocity lines of ± 8 m s^{-1}.

Furthermore the two high/low velocity symmetric patches result slightly counterclockwise-rotated due to the square shape of the combustion chamber. Remarkably, the flow field is correctly captured by numerical computations.

4.4.2 Power Spectral Density (PSD) of axial velocity

In addition to the mean and RMS values, it is also interesting to look at axial velocity spectra and compute Power Spectral Density (PSD) from local time signals: PSD are obtained experimentally from LDV velocity signals acquired along the x axis: from $x = -15$ mm to $x = 15$ mm with 0.5 mm step. It is worth mentioning that in contrast with simulations, measurements have been performed without combustion chamber. However it has been verified that experimental mean and RMS axial velocity are comparable with both PIV data the numerical

predictions obtained in confined configuration. This feature is attributed to the weak impact of the confinement on the flow structure close to the injector outlet, at $z = 3$ mm.

Simulations and experimental signals are extracted for axial velocity over a span of 120 ms in order to share the same numerical frequency resolution of 8.3 Hz. Even though the upper-limiting frequency of the spectra is mathematically fixed by the sampling frequency, this limit could be misleading since oil particles used to seed the flow act like a low-pass filter, not responding to high perturbation frequencies. In the present case, the cut-off frequency of the small oil particles is of the order of 4 kHz: above this value, experimental spectra can not be physically considered.

Fig. 4.8 displays the PSD at two locations (values in *mm*): $P = (3,\ 0,\ 3)$ is located in the wake of the central bluff-body and $Q = (7,\ 0,\ 3)$ lies in the shear layer of the swirling jet (Fig. 4.2). The gray scale marks the fact that at high frequencies only numerical results can be interpreted.

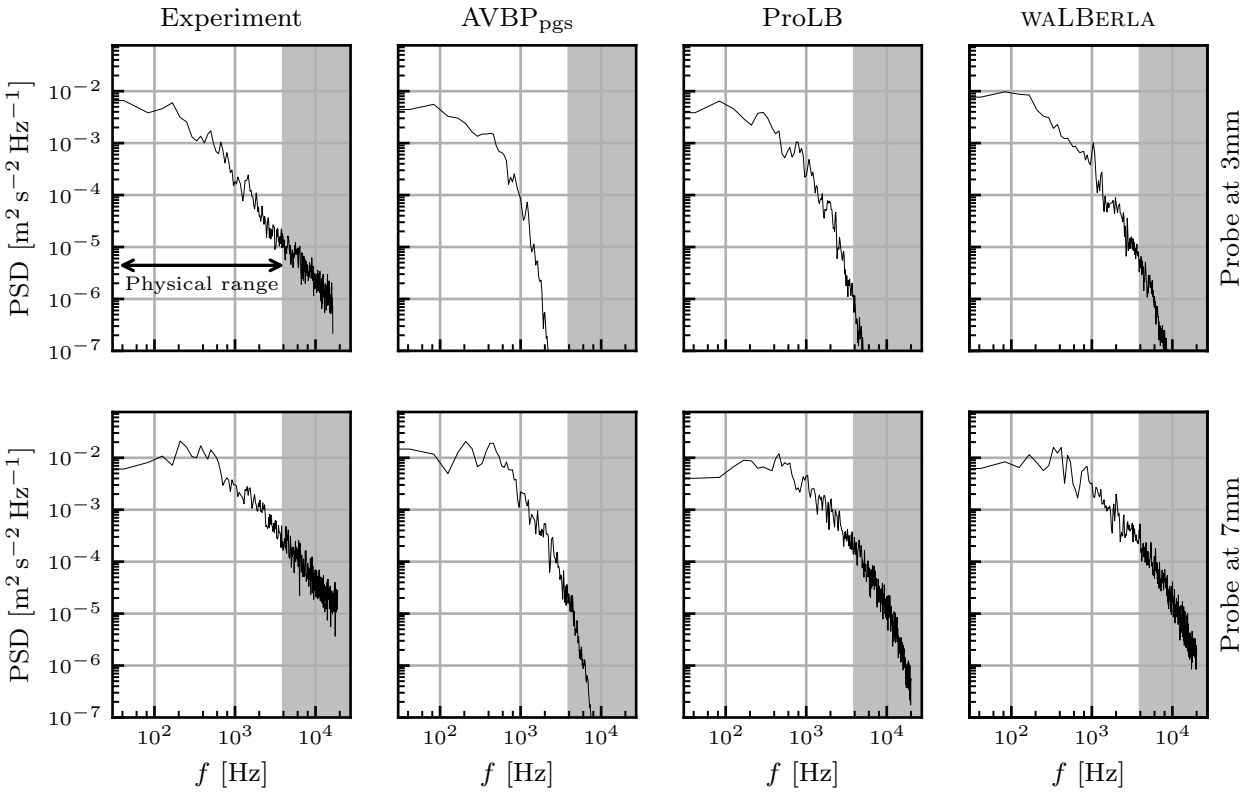

Figure 4.8 – Axial velocity spectra of kinetic energy for the different solvers at $P = (3,\ 0,\ 3)$ (top row) and $Q = (7,\ 0,\ 3)$ (bottom row)

For the present flow rate, experimental PSD results (left column in Fig. 4.8) do not exhibit peaks associated to coherent structures such as Precessing Vortex Cores (PVC) which are frequently found in swirling flows [148, 149, 150, 151]. Similarly all three simulations do not reveal any peak related to hydrodynamic modes. The PSD decay above 1 kHz shows that calculations exhibit a higher dissipation with respect to experimental results, maybe due to the LES subgrid model used in the three codes. Limited differences are observed among codes at point P. For point Q, a difference emerges in the high frequency range: the two LBM codes introduce less dissipation than the finite volume solver but it is difficult to say if this is physically right or not.

4.5 Comparison of computational costs

The code performances are given by Tab. 4.5. A first parameter, which is independent of mesh size and time step is the reduced computational time, i.e. the time required to perform one cell update. The last line of Tab. 4.5 displays a second parameter which is the most important one for the user: the total CPU time required by each code to compute 1 ms of physical time.

Code	**AVBP$_{\mathbf{pgs}}$**	**ProLB**	**waLBerla**
Time step [s]	4.4×10^{-7}	8.5×10^{-7}	7.1×10^{-7}
Equivalent Fine Fluid Nodes [M]	18.1	21.4	22.6
CPU time per iteration [ms]	83	90	24
Reduced computational time [μs iteration^{-1} cell^{-1} core]	1.67	1.50	0.38
Cost 1 ms physical time [CPUh]	19.1	10.6	3.4

Table 4.5 – Comparison of computational efficiency of the three different solvers on a 360 of the Kraken cluster[1]

All outputs and post-processing routines are disabled: only the fluid solver itself is considered. The earlier discussed performance measure MFLUPS is the inverse of the here presented reduced computational time. All codes run on 360 processes on the Kraken cluster[1], which uses a Intel Xeon Gold 6140 Skylake chipset.

Tab. 4.5 shows that the LBM solvers are faster than the finite volume solver but the speed ratios are not different by orders of magnitude: the fastest code waLBerla goes 5 times faster than the AVBP$_{\text{pgs}}$ solver.

4.5.1 Scaling

In addition to the computational cost at a fixed number of cores, scalability is an important question in HPC: the strong scaling behaviour of the three codes was tested here from 36 to 900 cores. We measure the parallel efficiency E by relating the the computational time per iteration T_P on a given number of cores N_P to the time per iteration T_{36} on 36 cores, which is equivalent one full node on the utilized architecture.

$$E = \frac{36}{N_P} \frac{T_{36}}{T_P} \tag{4.3}$$

Fig. 4.9a shows that AVBP scales almost ideally over the whole range of cores, while the LBM solvers efficiencies drop by 30-40% when increasing the number of cores by a factor of 25. In this particular configuration, parallel scalability is controlled by the spatial distribution of grid cells to achieve an even workload balance among all processes. In AVBP there are few constraints on the decomposition of the computational domain as long as the surface area between subdomains is kept at a minimum. Moreover, AVBP remains efficient even when only a few thousand mesh nodes are handled by each core.

[1] `https://cerfacs.fr/en/cerfacs-computer-resources/`

ProLB preserves performance up to 72 cores but then loses efficiency beyond 144 cores because of an increase in waiting time: the solver has an optimum scalability estimated between 10^5 and 10^6 fluid elements per core to efficiently manage industrial configurations that require much larger grids. In other words, while weak scaling works well in ProLB, the present strong scaling exercise is more difficult since the order of magnitude of fluid elements per core is 10^4 at 900 cores.

Whole blocks are assigned to processes in waLBerla . When using an excessive amount of cores, there are not enough blocks per process to construct an even workload distribution. On the other hand waLBerla exhibits excellent weak scaling until almost half a million cores [21, 94]. Furthermore in the LBM scheme the different levels of refinement have to be executed sequentially. This is an inherent obstacle to achieving even workload distribution and it limits strong scaling capabilities. The strong scaling limit of the LBM codes may affect the overall conclusion: at 900 cores, ProLB becomes less efficient than AVBP. waLBerla maintains the lowest computation time over the whole range of cores (Fig. 4.9 right).

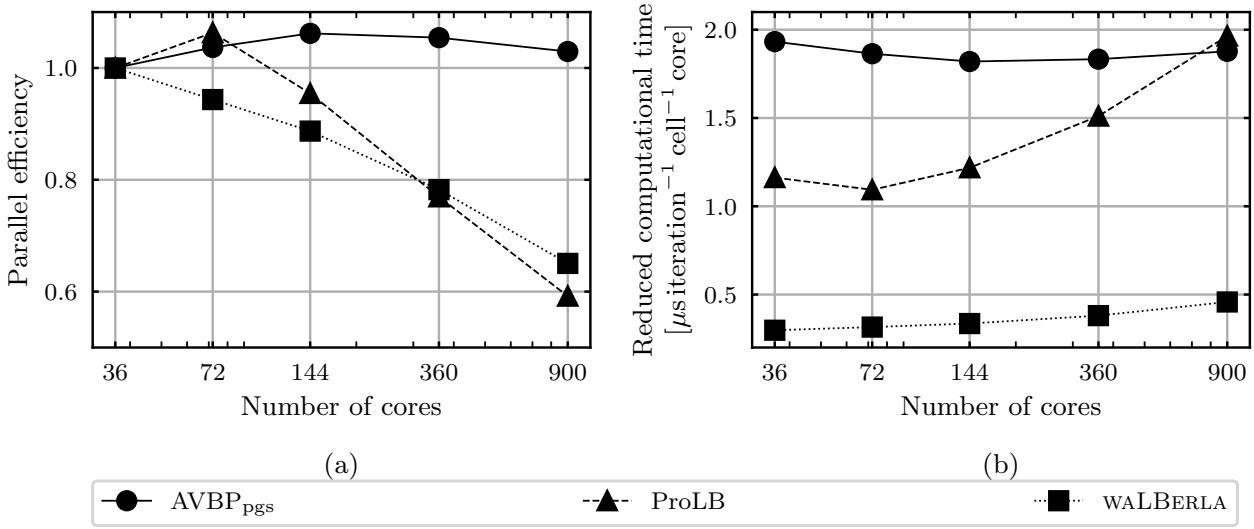

Figure 4.9 – Parallel performance of the three codes up to 900 cores, normalized by the performance at 36 cores.

4.6 Additional computations with waLBerla

4.6.1 Mesh convergence

The influence of mesh resolution on the quality of the results obtained by the waLBerla solver is investigated by repeating earlier simulations with varying minimum grid cell size. By only changing the grid size and keeping refinement zones constant, the resulting meshes hold the same block layout. Tab. 4.6 presents the number of EFFN and the pressure loss of simulations conducted with $\min(\Delta x) = 440, 220, 110$ and 55 μm minimum grid cell size. The corresponding velocity profiles at constant axial coordinate on the axial plane are depicted in Fig. 4.10.

At finer resolution, the prediction of pressure loss deviates further from the experimental value, highlighting once again the difficulty of finding the correct pressure loss with non-body-fitted meshes. A strong deterioration of simulated velocity profiles becomes apparent at a grid

min(Δx) [µm]	440	220	110	55
EFFN [M]	1.0	3.8	22.6	169.4
Cost 1 ms physical time [CPUh]	0.058	0.41	3.4	51
Δp (Pa)	345	316	313	307

Table 4.6 – Number of EFFN, CPU cost and pressure drop for different mesh resolutions using waLBerla

resolution of 440 µm. Most significant are the differences of different grid sizes for $u_{z,\mathrm{RMS}}$, $\bar{u}_x$ and $u_{x,\mathrm{RMS}}$ at $z = 5$ mm. Velocity peaks at $x \pm 10$ mm are more pronounced at high grid resolution and even overestimated compared to experimental results at $\min(\Delta x) = 55$ µm. The selected grid size of $\min(\Delta x) = 110$ µm is a reasonable compromise between capturing the experimental results and keeping CPU cost low.

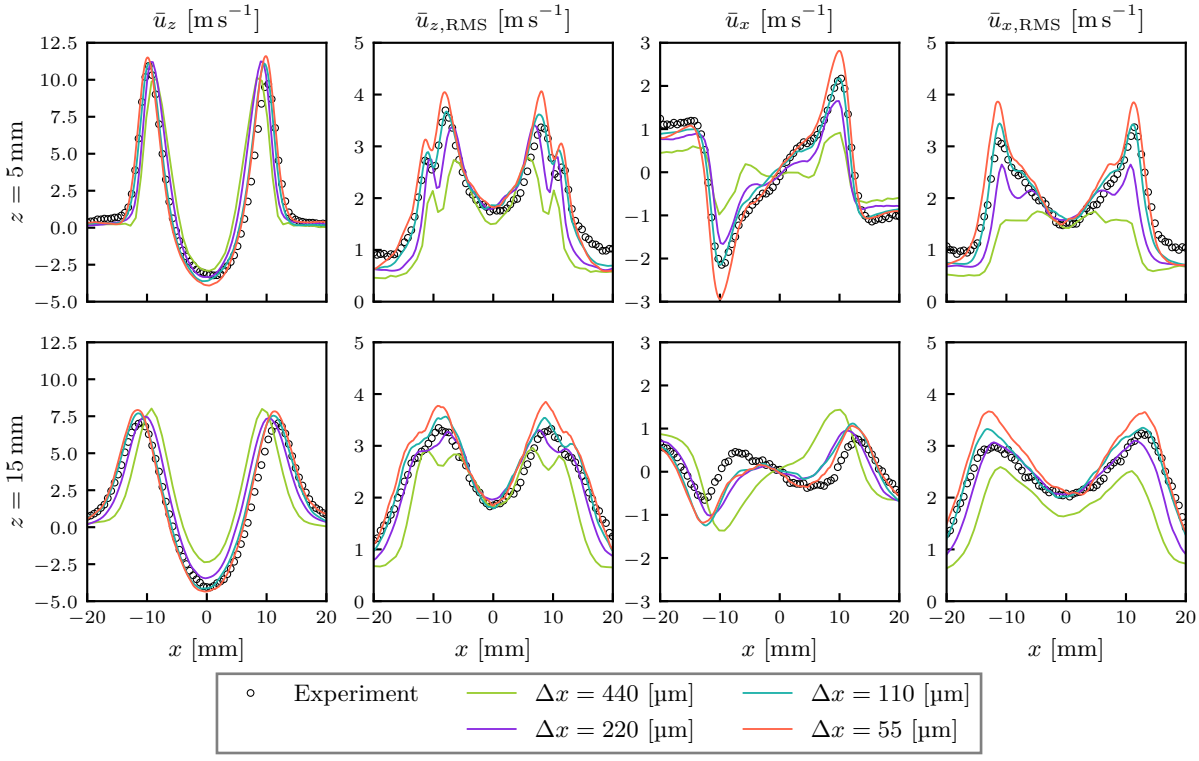

Figure 4.10 – Mean velocity profiles and related RMS of $\bar{u}_z$ and $\bar{u}_x$ for different mesh resolutions using waLBerla. Obtained at constant axial coordinate on the axial plane. First and second rows correspond to $z = 5$ mm and $z = 15$ mm, respectively..

4.6.2 Unconfined configuration

Finding the experimental measurements of the LDV with numerical simulation is more difficult because the flow is unconfined. The air can freely circulate in the experimental setup , which needs to be accounted for in the simulation. Therefore, a cylindrical domain with radius 880 mm (approximately 10 times the confinement wall cross-section) is placed at the backplane of the

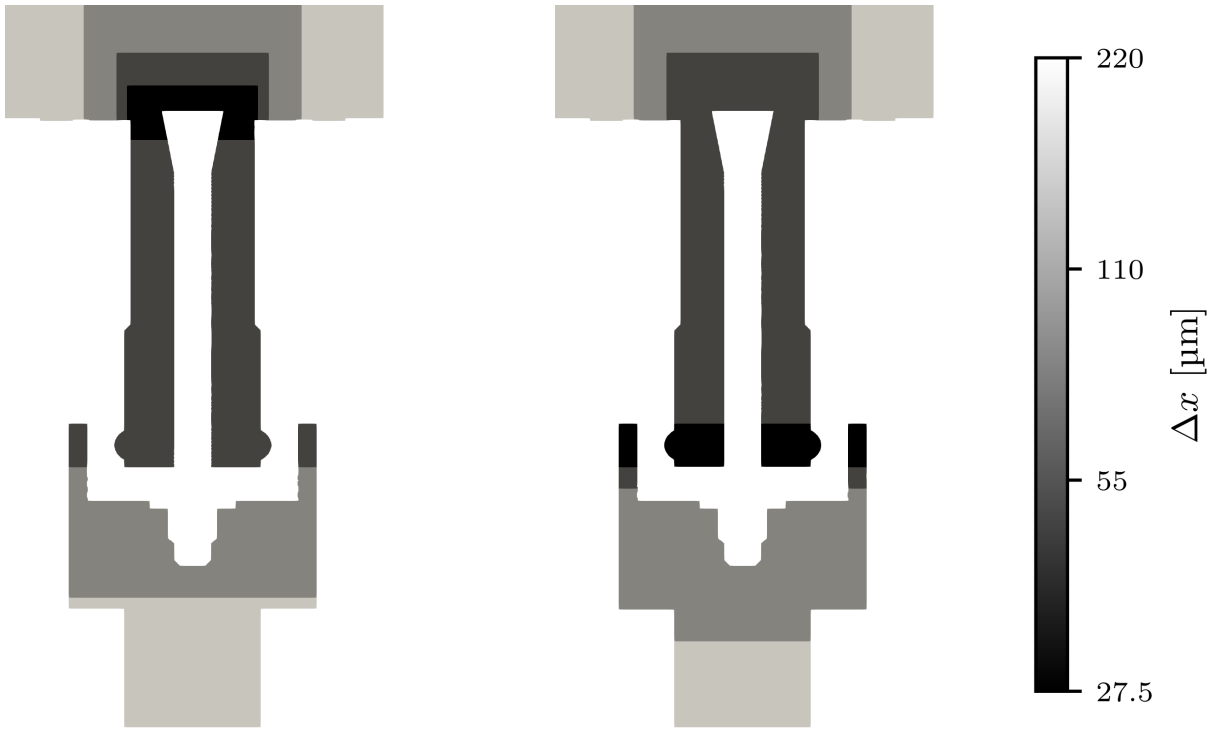

Figure 4.11 – Two different mesh layouts used for the unconfined configuration. Left: finest level at the injector; right: finest level at the swirlers channels.

combustion chamber. A free-slip boundary condition is set at the radius of the cylinder and the extension of an inlet condition with $u_{in} = 0.05u_b$ is set at the extension of the chamber backplane to ensure that there is no fluid being sucked in or out of the simulation domain.

The mesh resolution has to be fine to capture LDV results, especially for the radial component. Two different meshes, showed in Fig. 4.11, are investigate - mesh A with the finest grid level ($\min(\Delta x) = 27.5$ μm) in the vicinity of the injector and mesh B with the finest grid level at the swirler channels. Both meshes are composed of 9 grid levels in total and contain 234 M EFFN and 368 M EFFN, respectively.

Fig. 4.12 illustrates the simulation results of the two meshes against experimental measurements. The peaks in the radial mean velocity $\bar{u}_x$ at $x \pm 10$ mm are considerably underpredicted, but slightly better captured with mesh A. Placing the finest resolution at the injector also increases the peaks of RMS velocities $\bar{u}_{z,RMS}$ and $\bar{u}_{y,RMS}$ at the inner peak $x \pm 6$ mm. For $\bar{u}_{x,RMS}$ however, this peak is overpredicted with mesh A. Using a small grid size at the injector is important to accurately reproduce the sharp edge at the injector lip with the non body-fitted mesh. To find the exact velocity profile of $\bar{u}_x$ an even finer grid will be required.

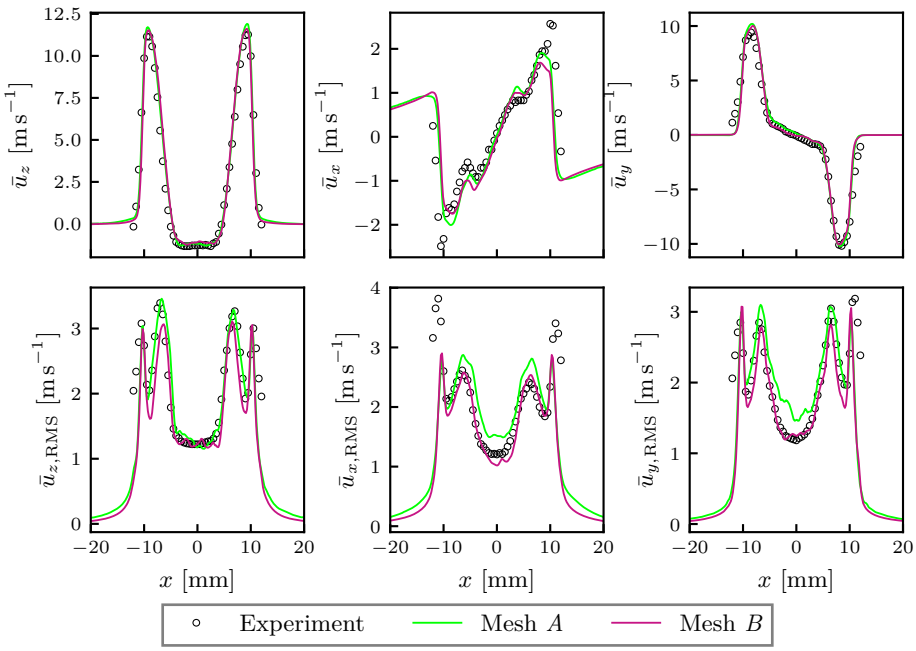

Figure 4.12 – Mean velocity profiles (top row) and related RMS (bottom row) of $\bar{u}_z$ and $\bar{u}_x$ and $\bar{u}_y$ for different meshes. Obtained at 1.5 mm distance from the bluff body.

4.7 Conclusions

One finite volume and two Lattice-Boltzmann solvers suitable for LES have been compared in terms of accuracy and CPU efficiency in a swirling flow test at CentraleSupelec EM2C, a typical aeronautical application.

The fidelity of the three solvers was demonstrated by comparing numerical and experimental PIV data in terms of: injector head pressure losses, mean and RMS velocity profiles and axial velocity spectra. Despite minor differences, the three solvers provide very similar and accurate results: the discrepancies with respect to experimental results are limited to the tenth of $\mathrm{m\,s^{-1}}$ on velocity profiles. For pressure losses, the finite volume solver using body-fitted meshes captures the experimental result very well (330 Pa for $\mathrm{AVBP_{pgs}}$ versus 335 Pa for the experiment) but the two LBM codes using structured meshes are also close to measurements (368 Pa for ProLB and 313 Pa for waLBerla). These results confirm that LES formulations provide high accuracy results for swirled flows, much better than usual RANS codes especially in terms of RMS data for all components. Furthermore LDV data at two specific locations are used to create PSD analysis of axial velocity: the three solvers as well as the LDV data do not reveal any hydrodynamic mode. Moreover, $\mathrm{AVBP_{pgs}}$ shows higher numerical dissipation in the high frequency range with respect to LBM solvers.

Strong scaling tests from 36 to 900 cores reveal that the finite volume solver maintains its performance, whereas the LBM codes exhibit some loss in efficiency as the workload per core decreases. On 360 cores the CPU times necessary to compute 1 ms of physical time are: 3.4 for waLBerla, 10.6 for ProLB and 19 CPU hours for $\mathrm{AVBP_{pgs}}$. The three solvers offer similar orders of magnitude in terms of absolute performance, especially considering the fact that the finite volume solver carried more equations (energy and chemical species) as well as complex thermochemical models.

A point which has been left for further studies is the importance of the mesh quality on the results. The results of $\mathrm{AVBP_{pgs}}$ and ProLB shown in this chapter were obtained with user-optimized meshes which play a crucial role in the final results, maybe as important as the solvers themselves. The Lattice-Boltzmann equation is discretized on cartesian cubic grids automatically generated in most solvers which alleviates cumbersome and time-demanding meshing. The block structured approach of waLBerla leaves less potential for mesh optimization, but it is easier to set up. Its scaling capabilities make it possible to efficiently perform simulations in the range of 1 M to over 300 M EFFN.

Finally I would like to give my personal recommendation to the reader. When results are needed quickly, when there is only few computational resources available and high accuracy is not the highest priority it is beneficial to employ a highly optimized, block-structured LBM code like waLBerla. On the other hand, when high fidelity results are desired a body-fitted FV code like $\mathrm{AVBP_{pgs}}$ is the best choice, since it was the only solver to accurately find the pressure loss from measurements. The algorithmic design of ProLB with its unstructured grid layout, which allows for refinement of individual grid cells, constitutes a good middle ground between the two other codes.

Chapter 5

Particles laden flow around a cylinder

Contents

This chapter corresponds to the work on an academic generic configuration, which was submitted to Physical Review Fluids in 2021 under the following reference [152]. In the introduction we motivate the topic by highlighting the importance of dispersed two-phase flows. The following section presents the numerical setup, including material properties, simulation parameters and the modeling of hydrodynamic interaction between particles. A comparison to data from literature is given for the single phase flow. Results are presented in terms of global flow parameters rationalized by means of effective suspension properties for water and three different particle materials: Hydrogel, Glass and Iron. The contributions of hydrodynamics and collisions to the drag force are discussed and the transition to granular flow is investigated. At last, we illustrate the performance of the fully coupled LBM-DEM algorithm for different particle volume fractions and the scalability up to 20480 cores.

5.1 Introduction

Dispersed two-phase flow are a widespread fluid dynamics problem that is encountered in various industrial (petroleum or nuclear engineering, concrete, food products, cosmetics and pharmacy) and natural processes (river flow, avalanches, dust storms) and even in biological fluids like blood. Suspensions of non-Brownian particles and granular flows are known to exhibit intricate behavior in response to shear flows. A large portion of today's energy transformation still relies on burning fossil fuels. Pulverized coal combustion is a gas-solid flow, that has been intensively studied to improve numerical predictions [153]. These simulation methods can be used to enhance efficiency of burners and boilers, such as the circulating fluidized bed [154, 155]. There have been recent efforts to compute small scale models with a few thousands particles by means of direct numerical simulation (DNS) [156, 157]. In medical research, red blood cells can be modeled by extending the numerical model to allow interfaces to deform. A combination of the Lattice Boltzmann method (LBM), immersed boundary method and finite element method has been used to simulate blood flow through an array of obstacles [158]. Most recently, humanity is fighting against a new thread that is propagated via dispersed particles in air. A deeper understanding of virus-laden droplet and aerosol flow patterns helps in creating guidelines to reduce COVID-19 transmission rates [159]. Particulate flows are also found in environmental engineering, such as sediment transport and dune formation in riverbeds [160] or erosion processes in geomorphological patterns [161]. There are also applications to astrophysics, where planet formation is explained by the hydrodynamics of dust grains in gaseous disks [162].

The insights gained by particle resolved DNS can help to improve closure models of unresolved methods such as the discrete particle method (DPM), where the size of particles is typically much smaller than the computational grid, and the two fluids model (TFM), where both fluid and solid phases are represented as a continuum. In large scale industrial applications this Eulerian-Eulerian approach is usually the only viable option due to the high computational demands of particle resolved methods.

We are aiming at providing information on the flow response due to the presence of particles by means of numerical simulations. The flow around a cylinder is one of the most generic flow configurations and it is well documented for the single phase configuration. By adding solid particles into the fluid we want to understand the interplay between fluid transport, particle inertia and collisions among individual particles as well as with the obstacle. This information is particularly relevant because the flow contains regions of particle impact in front of the obstacle and shear layers in the wake. The dynamics of neutrally buoyant particles in a stagnation point flow has been carefully studied by [163, 164]. When approaching an obstacle the particle motion strongly depends on it's size compared to the boundary layer thickness.

The granular phase in our simulations are resolved with a discrete element method (DEM) and tested against granular flow experiments [114] and numerical simulations [112, 165]. If the density ratio between particles and fluid is high and the suspension is sufficiently dilute there are only few interactions among particles and the fluid flow is unaffected by the presence of particles. Under these assumptions it is relevant to use one-way coupling between fluid and solid phases [166, 167, 168]. In this study, we make use of a fully-coupled approach, where fluid-particle and particle-particle interactions plus the feedback effect of particles on the fluid flow are captured. The physics changes when considering liquids instead of air as the carrying fluid (density ratio becomes close to unity for most solid materials), as shown by experiments of grain-water flows around a cylinder [169]. The presence of liquid (wet granular flow) modifies significantly the

flow behavior compared to granular media in the same situation [114]. Numerical simulations using Lattice Boltzmann method (LBM) have been conducted for suspension over an obstacle at Reynolds numbers well below the onset of unsteadiness [170]. They observed that isolated finite size particles released inside the recirculating wake region migrate towards a stable limit cycle at the boundary between wake and free stream. At low concentration, the wake remains depleted of particles. At higher density the limit cycle becomes unstable due to the particle's increased inertia [171]. Eventually this process will deplete the wake of particles, especially for particles of larger size. With many particles the hydrodynamic interactions and collisions among flowing particles can cause trajectory fluctuations which lead to an exchange of particles between the wake and the free stream.

Our work will utilize the computational efficient LBM coupled with a discrete element method to investigate this generic configuration over a wide range of Reynolds numbers and particle inertia to highlight the specific response of the fluid-solid mixture around an obstacle. We will test the applicability and limits of the assumption that a suspension can be interpreted as an equivalent Newtonian fluid whose viscosity and density depend on particle loading in the range of dilute to semi-dilute regime.

5.2 Numerical setup

The particle laden flow conditions of this study are characterized by low impact Stokes numbers

$$\mathrm{Stk}_{\mathrm{imp}} = \frac{(\rho_p + \rho_f/2)\, u_\infty d}{9\mu}, \tag{5.1}$$

hence fluid drainage before contact has a significant contribution to collisions. Momentum is being dissipated by the fluid as two obstacles approach each other. Particle interactions are strongly affected by hydrodynamic interaction and lubrication forces, which causes a reduction in the post-collision rebound velocity [86].

Including the calculation of short range hydrodynamic interactions into the algorithm, as discussed in [172], is numerically costly. Instead we model the effect of wet collisions by an effective rebound coefficient in the DEM simulations. The effective coefficient of restitution

$$e = e_{\mathrm{dry}} \exp\left(-\frac{\beta}{\mathrm{Stk}_{\mathrm{imp}}}\right), \tag{5.2}$$

with $\beta = 35$, is calculated [173] from the restitution coefficient without the presence of fluid e_{dry} and the impact Stokes number, which characterizes fluid drainage. At low Stokes numbers $\mathrm{Stk}_{\mathrm{imp}} \to 0$ the viscous forces of the fluid slow down the particle so far, that it will not come in contact or at least not rebound from the obstacle. At high Stokes numbers the influence of the fluid is negligible such that $e = e_{\mathrm{dry}}$.

Three different sets of material properties will be utilized that resemble three materials commonly used in experimental suspension flows. Hydrogel, which corresponds to neutrally buoyant particles in water and glass, iron for inertial particles. The corresponding parameters for the rigid body dynamic solver can be found in Tab. 5.1. The fixed cylinder is always assigned the properties of glass material. The effect of gravity is neglected.

The simulation domain size spans 40 cylinder diameters in streamwise direction ($\mathbf{x}$), 24 cross-stream ($\mathbf{y}$), and 5 spanwise ($\mathbf{z}$). The domain is periodic in cross-stream and spanwise directions. The cylinder has length L_z, the initial fluid velocity is equal to the upstream

Material	Density g cm^{-3}	$e_{\mathrm{dry,p-p}}$	$e_{\mathrm{dry,p-c}}$	$\mu_{\mathrm{s,p-p}}$	$\mu_{\mathrm{d,p-p}}$	$\mu_{\mathrm{s,p-c}}$	$\mu_{\mathrm{d,p-c}}$
Hydrogel	1	0.05	0.1	0.01	0.01	0.5	0.1
Glass	2.5	0.68	0.68	0.9	0.4	0.9	0.4
Iron	7.8	0.4	0.55	1.1	0.15	0.7	0.5

Table 5.1 – DEM material parameters used in this study[1,2,3]

velocity u_∞ and the fluid has density ρ_f. A constant, uniform velocity $u_{in} = u_\infty$ is prescribed at the inlet and a constant pressure condition (see Sec. 2.3.8) is applied on the outlet to mimic a free exit of fluid and particles. Non-reflective boundary conditions are not required because under current flow conditions, vortices leaving the domain are not expected to be strong enough to cause stability problems or unphysical behavior.

Particles are seeded in front of the domain inlet at random positions regarding **y** and **z** coordinates and their initial velocity is equivalent to the fluid inlet velocity u_{in}. The number of particles seeded per time step is

$$\dot{n} = \frac{u_{in}\Theta A}{V_p}, \tag{5.3}$$

where $A = L_y L_z$ is the cross section area and $V_p = \pi d^3/6$ is the particle volume, is set in order to achieve the desired solid volume fraction Θ . Particles will be removed from the computation when their volume is entirely outside of the fluid domain.

To ensure that the boundary conditions have no influence on simulation results, the domain size in each spatial direction has been varied to find the dimensions at which global flow parameters remain constant. The extent of the simulation domain in the cross-stream direction is large enough to consider the cylinder as isolated. For specific test cases, such as the oscillating particle or the Segré-Silberberg effect, the collision model with two relaxation times (TRT) gave better results. However, we employ the single relaxation time model (BGK) for the suspension flow around a cylinder, since it provides sufficiently accurate results.

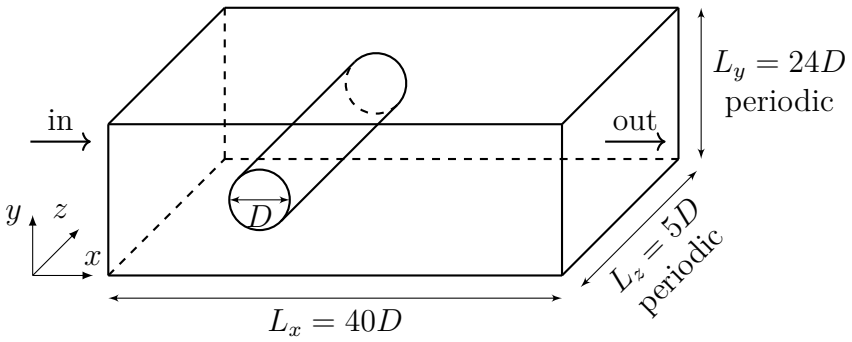

Figure 5.1 – Schematic presentation of the simulation domain.

The initial transient of the simulation is assumed to be completed once drag force, lift force RMS and recirculation length have reached a constant average value. From then, temporal

[1] https://engineeringlibrary.org/reference/coefficient-of-friction
[2] https://www.engineeringtoolbox.com/friction-coefficients-d_778.html
[3] https://en.wikipedia.org/wiki/Coefficient_of_restitution

signals and mean flow fields are recorded for 20 periods of the expected vortex shedding oscillation. The instantaneous fluid velocity is recorded at three points that are located one diameter in cross-stream and 1, 5, 20 diameters in streamwise direction away from the cylinder center in order to evaluate the vortex shedding frequency through fast Fourier transform. This is an unambiguous procedure for single phase flows since there is one distinct shedding frequency, but the introduction of particles creates noise in the velocity spectrum. At flow states close to the bifurcation, it becomes difficult to decide whether or not a flow is unsteady. We declare a configuration to be unsteady if we can find one distinct peak in the frequency spectrum.

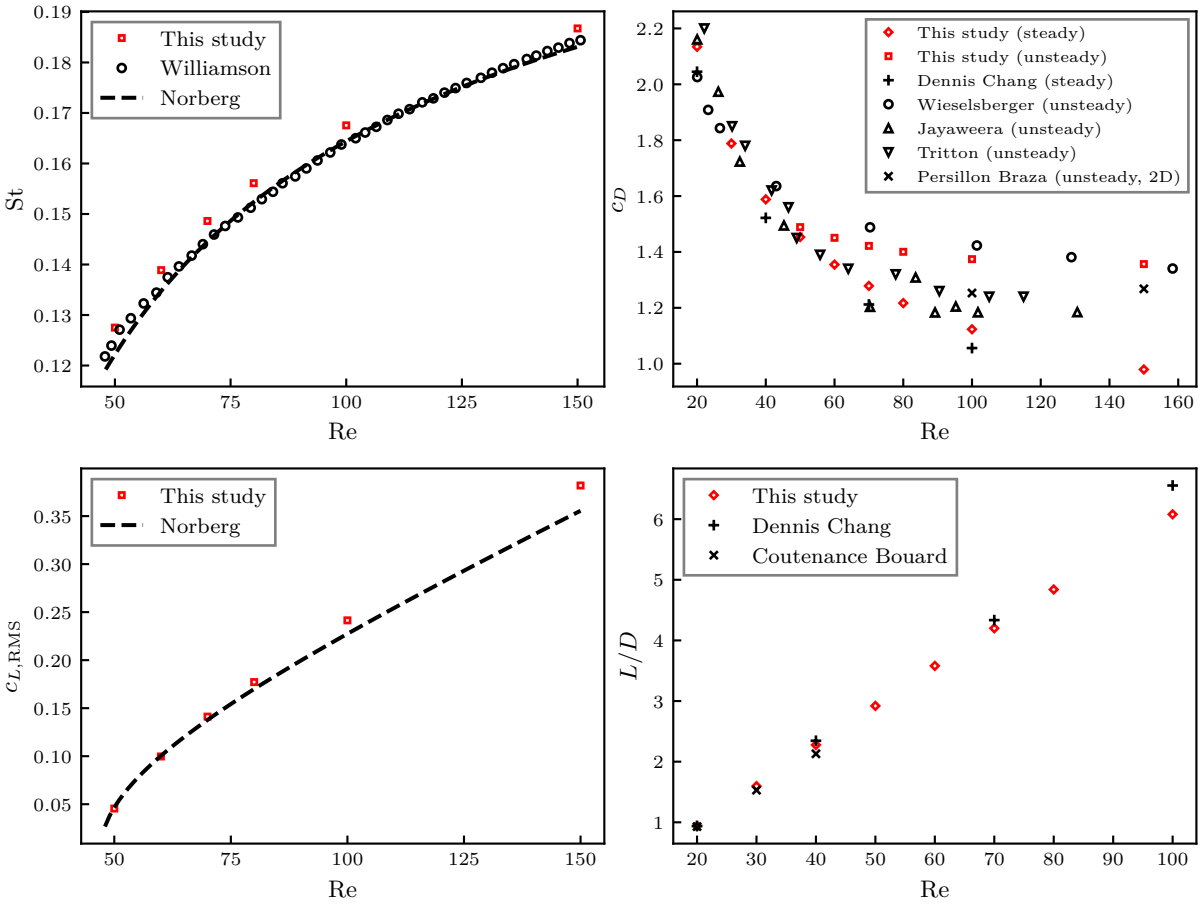

Figure 5.2 – Single phase flow past a circular cylinder: Top/left - Dimensionless vortex shedding frequency; top/right - drag coefficient; bottom/left - R.M.S. of lift coefficient; bottom/right - wake recirculation length under steady regime. Our results are compared to data from Williamson [174], Norberg [175], Dennis and Chang [176], Wieselsberger [177], Jayaweera and Mason [178], Tritton [179], Persillon and Braza [180], Coutanceau and Bouard [181].

For accuracy reasons we want particles to be resolved with at least 10 d/Δx, so to achieve a ratio of $D/d = 5$ the cylinder needs to have 50 cells per diameter. The total number of lattice cells amounts to 600M and at the highest solid volume fraction of 20% there are more than 220,000 particles simultaneously resolved inside the domain, increasing to 1.76 M for $D/d = 10$. The dimensionless frequency of particle oscillation due to vortex shedding in the wake of the cylinder can be estimated as $\Psi^2 = 2\pi \mathrm{StkRe}(d/D)^2$ which ranges from 1 to 5 for $D/d = 5$ and is always below 1.25 when $D/d = 10$. The effects of the size of the simulation domain and the spatial discretization have been tested on a reference case of particle laden flow (see Tab. 5.2).

L_x	L_y	d/Δ_x	St	c_D	$c_{L,\mathrm{RMS}}$
40	24	10	0.1401	1.392	0.100
80	24	10	0.1401	1.386	0.098
40	48	10	0.1401	1.383	0.099
40	24	15	0.1417	1.396	0.099

Table 5.2 – Effect of domain size and mesh discretization on particle laden flow properties. Fluid Reynolds number is Re = 80 with $\Theta = 10\%$ volume concentration of neutrally buoyant particles ($D/d = 5$).

We observe less than 1% variations of the Strouhal number or the drag and lift coefficients.

Four physical parameters from the classic single phase von Kármán vortex street are extracted and used to validate our computational methods. The vortex shedding frequency f is characterized by the Strouhal number

$$\mathrm{St} = \frac{fD}{u_\infty}, \tag{5.4}$$

fluid drag F_D and lift F_L forces are reduced to the dimensionless coefficients

$$c_D = \frac{F_D}{(1/2)\,\rho_f u_\infty^2 D L_z} \tag{5.5}$$

and

$$c_L = \frac{F_L}{(1/2)\,\rho_f u_\infty^2 D L_z}, \tag{5.6}$$

respectively and the recirculation zone length L, which is normalized by the cylinder diameter D. The simulation results we obtained using the BGK collision model are documented in Tab. 5.3, 5.4 and a comparison with reference experiments and numerical computations is found in Fig. 5.2.

Re	c_D	L/D
20	2.134	0.94
50	1.45	2.92
100	1.123	6.08
150	0.979	9.14

Table 5.3 – Steady single phase cylinder flow parameters from our simulations.

Re	St	c_D	$c_{L,\mathrm{RMS}}$	L/D
50	0.127	1.489	0.045	2.42
60	0.139	1.451	0.100	2.04
80	0.156	1.401	0.177	1.64
100	0.168	1.374	0.241	1.40
150	0.187	1.357	0.382	1.04

Table 5.4 – Unsteady single phase cylinder flow parameters from our simulations.

5.3 Results

5.3.1 Neutrally buoyant particles (hydrogel)

By introducing rigid spherical particles into the fluid, a specific response of the flow is expected relative to the solid volume fraction. A simple model of particle induced flow modification is based on the concept of effective physical properties for the mixture. The stiffness of particles allows them to resist compression and elongation generating hydrodynamic perturbations in the flow field which dissipate additional energy. At higher volume fraction, particle interactions such as lubrication effects and solid contact come into play. Close to packing volume fraction, hydrodynamic stresses are dominated by friction forces. As we investigate flow up to 20% volume fraction, this will not be the case for this study, except possibly for very localized zones in the vicinity of the cylinder. There are a number of correlations for estimating the effective suspension viscosity, namely Einstein [182], Batchelor & Green [183], Dougherty & Krieger [184], Hsueh & Becher [185], Eilers [186]. For this study we employ Eilers' equation with $\Theta_{\max} = 0.64$ corresponding to random assembly of spheres at close packing density

$$\eta_{\mathrm{eff}} = \eta_0 \left(1 + \frac{2.5\Theta}{2(1 - \Theta/\Theta_{\max})}\right)^2 . \tag{5.7}$$

The dimensionless shedding frequency St is represented as color map over the flow Reynolds number Re and solid volume fraction Θ in Fig. 5.3. Filled symbols indicate unsteady flow states and possibly vortex shedding, whereas open symbols and white area represent steady flow states. When increasing the particle volume fraction, the effective suspension viscosity increases causing flow oscillations to reduce. When accounting for the suspension viscosity by using an effective Reynolds number $\mathrm{Re}_{\mathrm{eff}} = \frac{\rho_f u_\infty L}{\mu_{\mathrm{eff}}}$, the contour lines of St become vertical indicating similar flow states for constant $\mathrm{Re}_{\mathrm{eff}}$, corresponding to the behavior of an equivalent fluid.

For the single phase flow the transition between steady and unsteady flow is marked by the critical Reynolds number $\mathrm{Re}_{\mathrm{crit}}(\Theta = 0) \approx 48$. The presence of particles triggers instabilities in the flow field, which is why we can find flow unsteadiness at sub-critical Reynolds numbers $\mathrm{Re}_{\mathrm{eff}} < \mathrm{Re}_{\mathrm{crit}}(\Theta = 0)$. These flows oscillate at lower frequency than the minimum vortex shedding frequency found in single phase flows $\mathrm{St} < \mathrm{St}(\Theta = 0, \mathrm{Re} = \mathrm{Re}_{\mathrm{crit}})$, but they are not necessarily shedding vortices. Local vorticity production at the top and bottom of the cylinder is not intense enough for the Kelvin-Helmholtz instability of the shear layer to set in. The wake is weakly meandering periodically without occurence of roll-up that yields alternative vortex

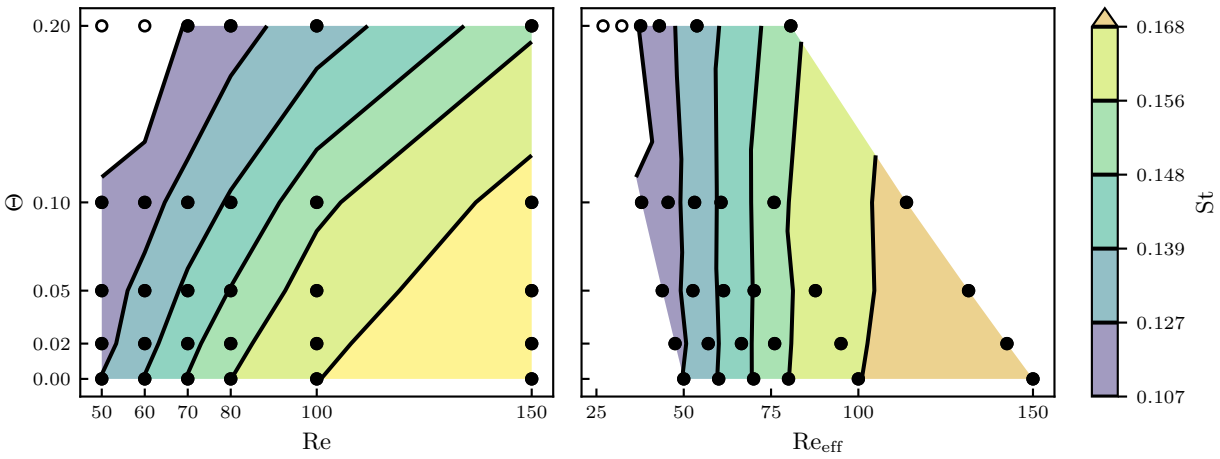

Figure 5.3 – Dimensionless shedding frequency St as map of Re, Θ for a suspension with hydrogel particles. Closed symbols: unsteady flow; open symbols: steady flow.

shedding typically observed in the von-Karman street. At Reynolds numbers $\mathrm{Re}_{\mathrm{eff}} > \mathrm{Re}_{\mathrm{crit}}(\Theta = 0)$ the classic vortex shedding is observed again.

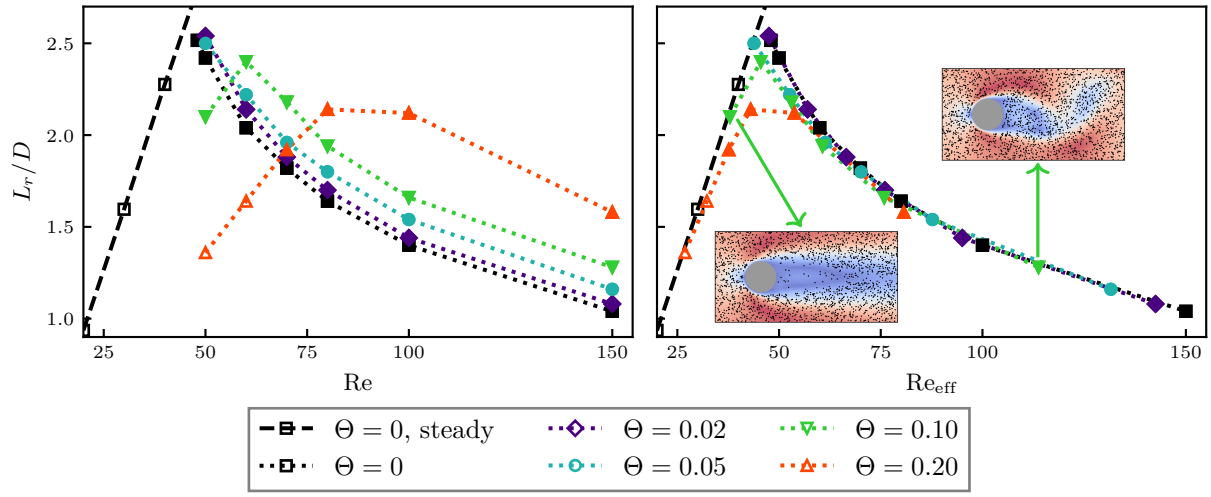

Figure 5.4 – Recirculation length as function of Re for a suspension with hydrogel particles. Closed symbols: unsteady flow; open symbols: steady flow. Instantaneous flow snapshots at Θ = 10% and $\mathrm{Re}_{\mathrm{eff}}$ = 38, 114 colored by fluid velocity magnitude and particles are represented as black points. Point size is not representative of particle size.

In an unsteady regime, the averaged recirculation zone will shrink as vortex shedding intensifies. The evolution of recirculation length for different Re and Θ is shown in Fig. 5.4. Due to the effect of effective viscosity a suspension can return to steady flow, which causes wake length to follow the trend seen in Fig. 5.2. When transforming the plot to effective parameters, all lines collapse onto a mastercurve that follows the steady single phase evolution up to $\mathrm{Re}_{\mathrm{crit}}$ and the unsteady single phase curve beyond. Haddidi et al. [170] have shown a depletion of particles in the recirculating wake for Reynolds numbers well below the onset of unsteadiness. We can observe a similar behavior in our simulations at Re = 50, where the concentration of particles in the wake is low. Simulations of neutrally buoyant particles in a confined channel using a

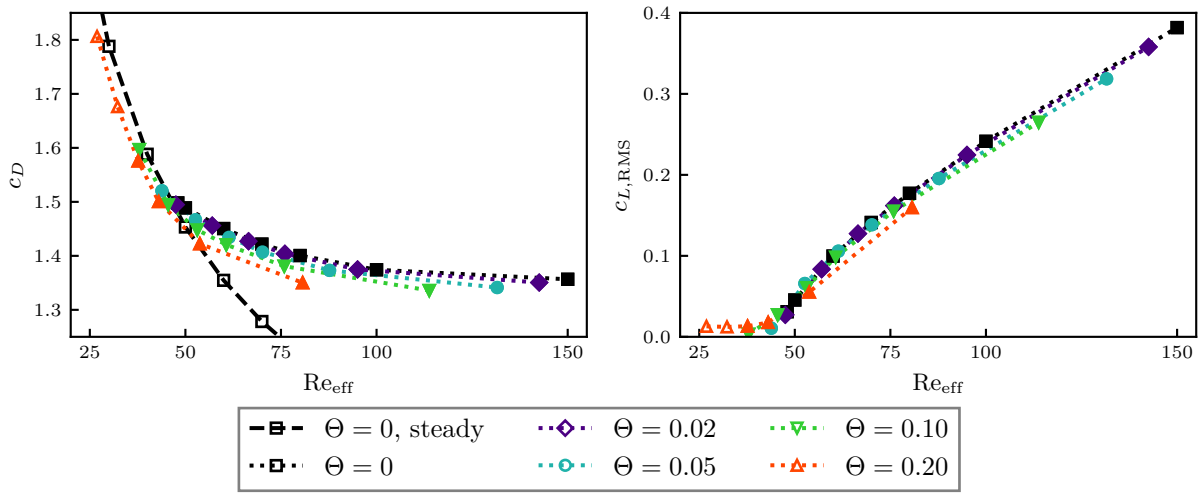

Figure 5.5 – Drag and lift coefficients as function of Re for a suspension with hydrogel particles. Closed symbols: unsteady flow; open symbols: steady flow.

Suspension Balance Direct-Forcing Immersed Boundary Model (SB-FD-IBM) by Dbouk [187] also yield a depletion of particles in the wake region, which is in agreement with our results. In their configuration, the onset of vortex shedding in terms of Reynolds number is delayed due to the confinement by the walls and in contrast to our approach the vortices are void of particles. This behavior indicates that particle-particle interactions play an important role in transporting finite size particles towards the vortex center for unsteady regime.

Using effective viscosity collapses all the simulation results onto the single phase flow evolution for cylinder drag and lift coefficients. Fig. 5.5 reveals a slight drag underprediction for high solid volume fraction as well as high Reynolds numbers. For suspensions below $\mathrm{Re}_{\mathrm{crit}}$, the single phase lift coefficient RMS is equal to zero but nonzero fluctuations are found in the signal for two-phase flows due to the random collisions of particles. A rolling average with window length of $T/10$ corresponding to the period T of minimum Strouhal number $\mathrm{St}_{\mathrm{min}} = 0.12$ was applied to smooth out random fluctuations.

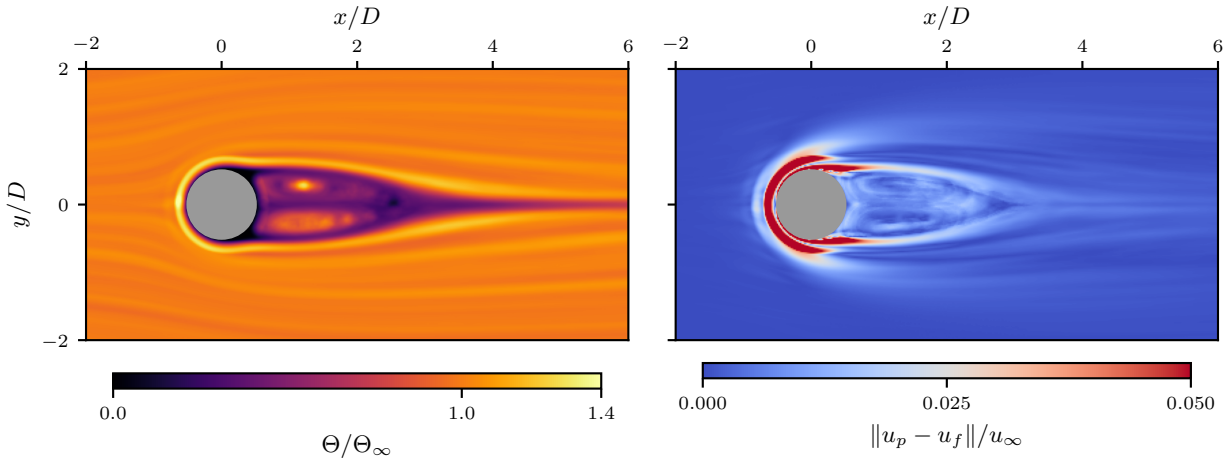

Figure 5.6 – Time averaged flow fields of solid volume fraction and slip velocity of a suspension with hydrogel particles, $\Theta_\infty = 0.1$ and $\mathrm{Re}_{\mathrm{eff}} = 38$.

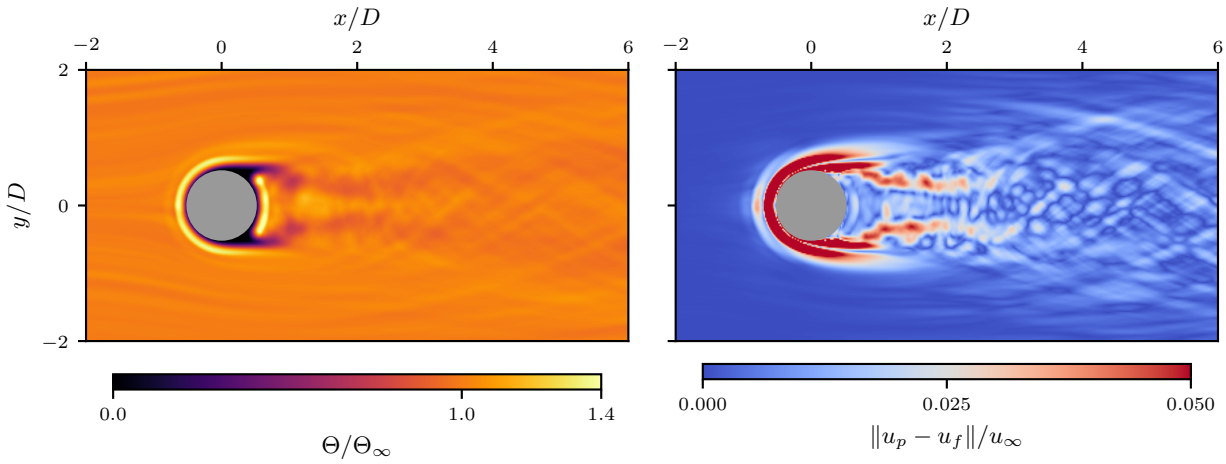

Figure 5.7 – Time averaged flow fields of solid volume fraction and slip velocity of a suspension with hydrogel particles, $\Theta_\infty = 0.1$ and $\mathrm{Re}_{\mathrm{eff}} = 114$.

Time averaged flow field of the particle concentration and the slip velocity between particle and fluid are presented in Fig. 5.6 and 5.7. When interpreting global flow parameters in terms of the effective viscosity, the underlying assumption is that the resulting suspension viscosity is uniform throughout the flow. The effective viscosity is proportional to the solid volume fraction, which is not homogeneous but there is an accumulation of particles in the stagnation zone in front of the cylinder and a lower concentration in the recirculation zone. We observe a slightly increased particle volume fraction along the edge of the recirculation zone for the non-oscillating case, whereas the recirculation zone is broken for the oscillating wake and instead we find an accumulation of particles that are stuck right behind the cylinder. The cyclic movement of particles inside the wake of $\mathrm{Re}_{\mathrm{eff}} = 38$ compared to $\mathrm{Re}_{\mathrm{eff}} = 114$ transports particles outwards towards the limit cycle. Contrary, fluctuations in the flow and collisions at the edge can cause particles to enter the recirculation zone. Slip velocity is largest at the stagnation point in the front of the cylinder, where particles moving very slowly due to contact with the cylinder. Also there is a slightly increased slip velocity along the edge of the recirculation length.

The effective viscosity correlation used here is derived from experiments of suspensions with small particle diameter compared to the cylinder $d \ll D$. It is not obvious that they can hold true for a diameter ratio of $D/d = 5$. To investigate the effect of particle size, we double the cylinder and domain sizes but keep the previous particle diameter to achieve a $D/d = 10$ while maintaining the particle resolution of 10 lattice cells per diameter. As shown in Fig. 5.8, the drag coefficient remains unchanged. However, the recirculation length evolution is closer to the single phase flow data in the region close to the onset of unsteady flow. The increased diameter ration brings us closer to the initial assumption of suspensions with minuscule particles compared to the cylinder.

5.3.2 Glass particles

The material we investigate now is composed of glass particles, which have a relative density $\rho^* = \rho_p/\rho_f = 2.5$. Increasing the material density means particles will have more inertia and less tendency to follow the flow streamlines. We recall that gravity is not considered. The effect of inertia is not accounted for in the effective viscosity model and can have an impact on the flow rheology, especially in the wake zone and in high shear stress regions at

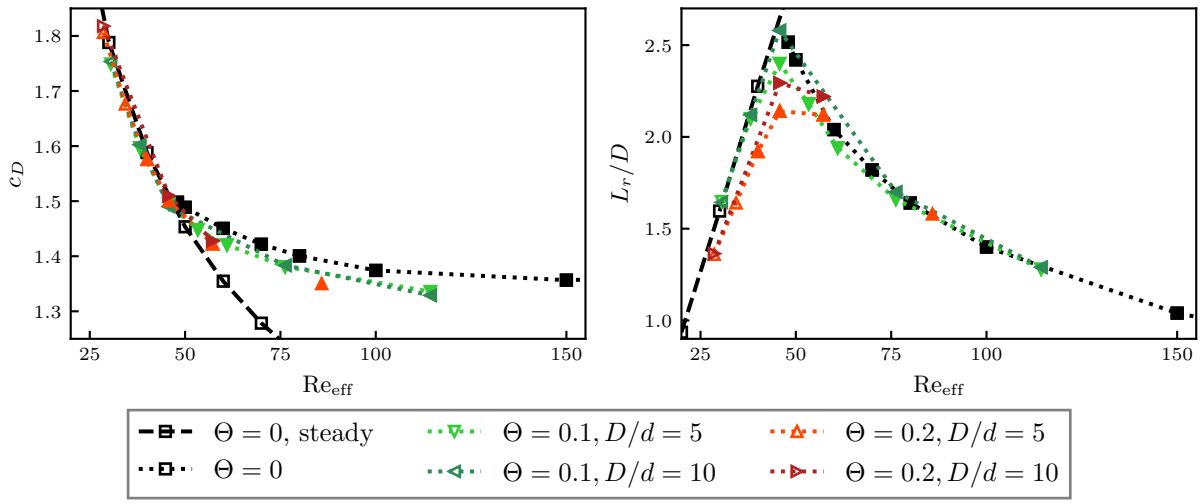

Figure 5.8 – Drag and recirculation length as function of Re for a suspension with hydrogel particles. Comparing particle sizes D/d=5 and D/d=10. Closed symbols: unsteady flow; open symbols: steady flow.

top and bottom of the cylinder. Contour lines of the dimensionless shedding frequency in Fig. 5.9 reveal a slight inclination to higher $\mathrm{Re_{eff}}$ at increasing volume fractions. Similarly to hydrogel, there is a sub-critical region where the flow is unsteady but not shedding vortices. Other quantities like drag and lift coefficients, recirculation zone length abide to the predicted collapse on the single phase curve, except for points at the higher Reynolds numbers, which show a slight deviation. It should be noted that the Reynolds number $\mathrm{Re_{eff}} = \frac{\rho_{\mathrm{eff}} u_\infty L}{\mu_{\mathrm{eff}}}$, as well as the drag and lift coefficient $c_{D,\mathrm{eff}} = \frac{F}{\rho_{\mathrm{eff}} u_\infty^2 A/2}$, now have to incorporate the suspension's effective density $\rho_{\mathrm{eff}} = (1-\Theta)\rho_f + \Theta\rho_p$ which is different from fluid density and evolves with particle concentration.

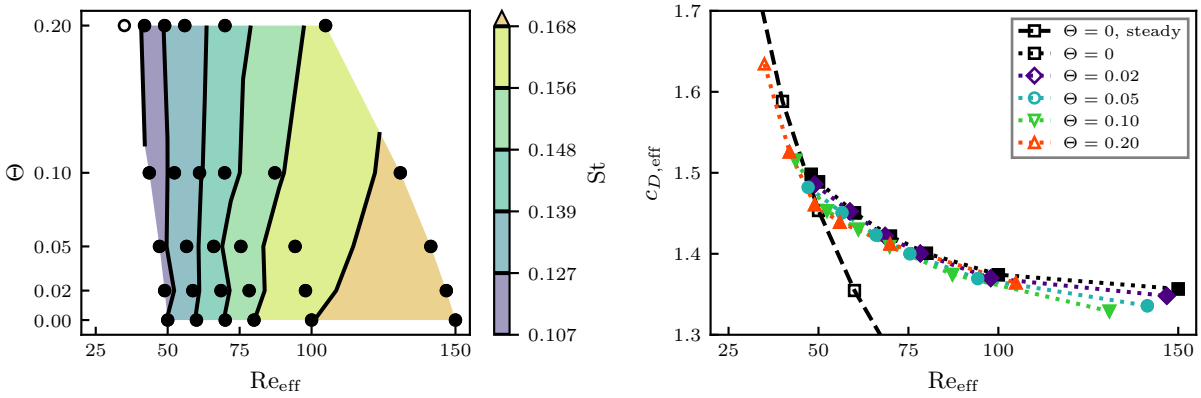

Figure 5.9 – Strouhal number and drag coefficient for a suspension with glass particles. Closed symbols: unsteady flow; open symbols: steady flow.

Glass has similar density than sand and all features we observed in our simulations are relevant to sediment transport in water. Inertia starts to come into play while effective density reaches 1.3 for volume fraction $\Theta = 20\%$.

5.3.3 Iron particles

At even higher relative density of $\rho^* = 7.8$ we find the failure of effective viscosity modeling due to significant inertia effect. Strouhal contour lines are heavily skewed with many simulations at high volume fraction showing flow oscillation without vortex shedding or with vortices developing further downstream, as we will see later. Suspension drag coefficients in the supposedly unsteady regime are deviating away from the single phase unsteady curve towards the steady curve. This response is due to the increased inertia of particles, which yields a detachment from fluid streamlines and inhibits the flow from developing its inherent flow structure. Similar to Fig. 5.10, suspension recirculation length above $\mathrm{Re}_{\mathrm{eff}} = \mathrm{Re}_{\mathrm{crit}}(\Theta = 0)$ is drifting away from the single phase unsteady curve and are approaching the steady curve. Lift RMS is strongly dampened compared to single phase unsteady flow.

In this regime, particles impact the cylinder with significant momentum. The Stokes number characterizing the particles is now sufficiently large to prevent the particles from following the fluid elements and the wake region remains depleted of particles. This is consistent with the simulation results of [171] which showed that when particle inertia is increased the limit cycle of particle trajectories in the wake region becomes unstable. Although those simulations were carried out for a single particle, here we observed the same response of the particle laden flow for many particles interacting in the wake region.

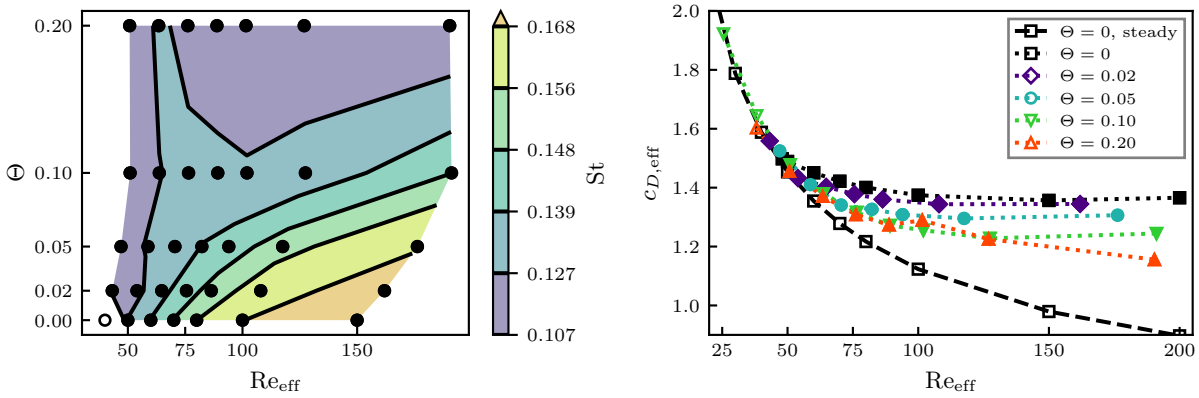

Figure 5.10 – Strouhal number and drag coefficient for a suspension with iron particles. Closed symbols: unsteady flow; open symbols: steady flow.

Once again we observe an inhomogeneous distribution of particles in the averaged flow fields in Fig. 5.11 and 5.12. The highest particle concentration is found at the stagnation point in front of the cylinder while the wake is void of particles. Additionally, we can identify the form of the bow shock, especially for the higher Reynolds number $\mathrm{Re}_{\mathrm{eff}} = 191$. The edge of the recirculation zone is distinctly recognizable by a thin layer of low slip velocity between particle and fluid compared to higher slip velocities inside and outside the recirculation zone.

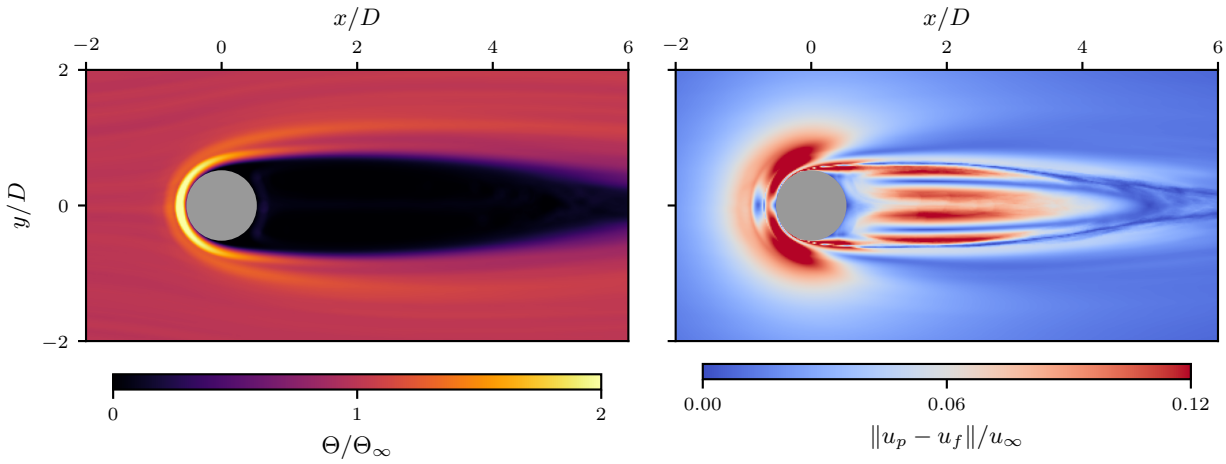

Figure 5.11 – Time averaged flow field of solid volume fraction and slip velocity of a suspension with iron particles, $\Theta_\infty = 0.1$ and $\mathrm{Re}_{\mathrm{eff}} = 64$.

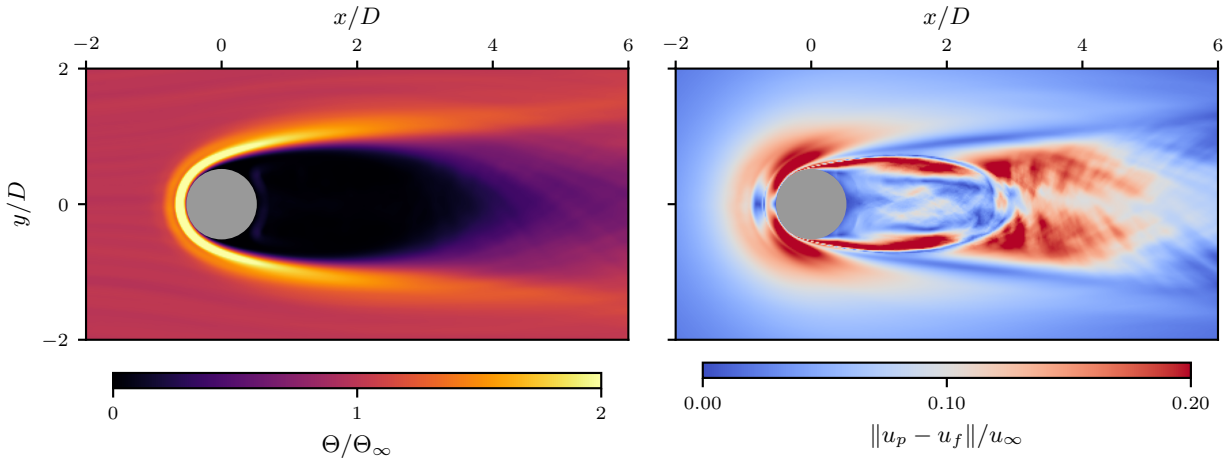

Figure 5.12 – Time averaged flow field of solid volume fraction and slip velocity of a suspension with iron particles, $\Theta_\infty = 0.1$ and $\mathrm{Re}_{\mathrm{eff}} = 191$.

5.4 Discussion of the contributions to drag force

The reliability of effective fluid prediction for the three different materials is summarized in Fig. 5.13 by relating the suspension drag coefficient to its single phase value at corresponding $\mathrm{Re}_{\mathrm{eff}}$. If the suspension is unsteady - even if it is not vortex shedding - we relate it to the unsteady single phase drag, otherwise we compare it to the steady drag coefficient. Hydrogel and glass suspensions are close to the ideal line, where the prediction matches the suspension drag exactly. However, with iron particles there is an overprediction for steady cases and an underprediction for unsteady cases.

From our simulations, we can extract separately the contribution to the drag force which is exerted by the fluid phase and the rest which is caused by particle collisions transferring momentum to the cylinder. We added another suspension material with particles of relative density $\rho^* = 100$ to verify if it approaches the response of a granular flow in a gas ($\rho^* \gg 1$). Fig. 5.14 shows the suspension's particle contribution as a granular coefficient, revisiting eq. (3.16). Increasing the relative density brings the drag particle contribution closer to a dry granular flow. At high Reynolds number the effect of fluid viscosity is low, thus the fluid has less resistance

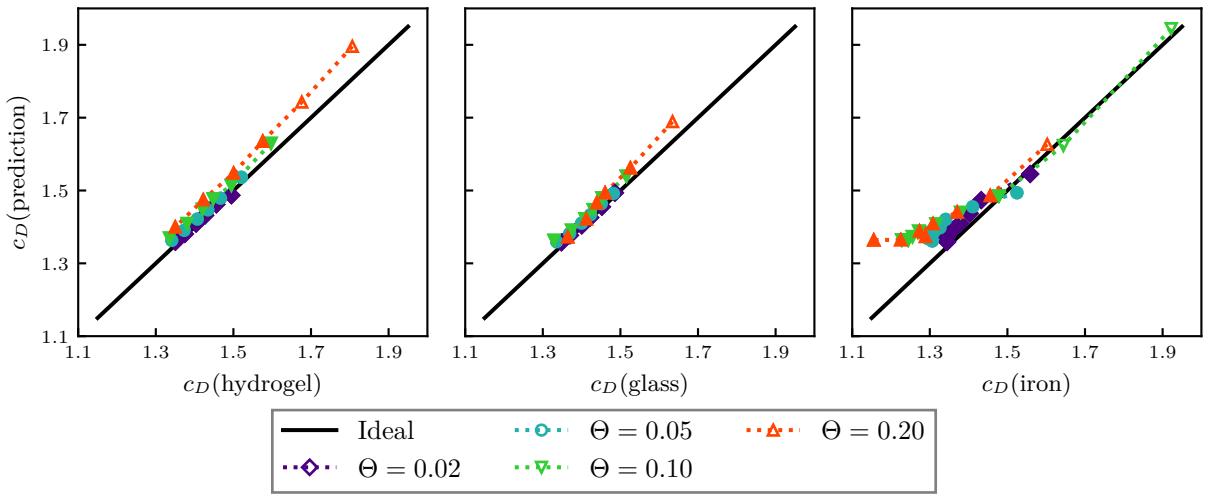

Figure 5.13 – Suspension drag coefficient compared to equivalent fluid prediction. Closed symbols: unsteady flow; open symbols: steady flow.

against particles and more of their momentum is being transferred onto the cylinder through collisions. This is especially true for the case of iron and $\rho^* = 100$ but opposite for hydrogel. Additionally, the particle contribution at high density ratio follows the trend of increased drag at high Knudsen number, whereas hydrogel suspension shows the opposite trend. There are two main distinctions in the flow structure that can be made responsible for these observations. One is that low density ratio suspensions are more easily prone to unsteady vortex shedding while particles are following fluid pathlines and the other one is the formation of a bow shock, typically observed for granular flows at high solid volume fraction. The occurence of bow shock points out the strong decorrelation of fluid and particles motion in the wake.

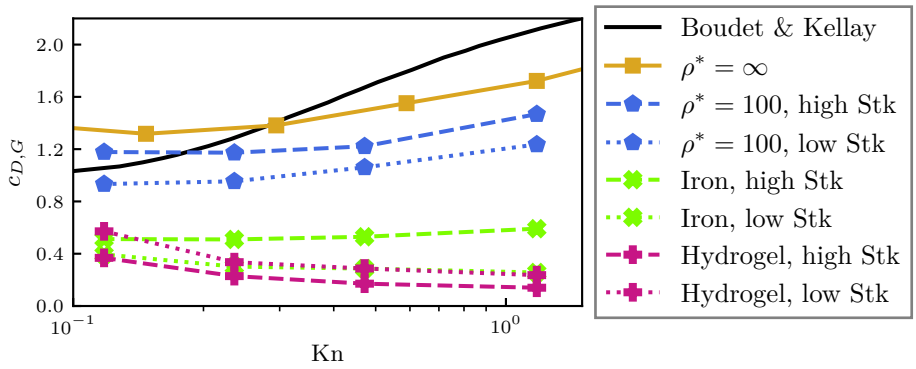

Figure 5.14 – Particle drag contribution for different suspensions compared to granular drag coefficient. Experiments from Boudet & Kellay [114].

Finally we give an overview on the ratio between fluid $c_{D,f,\mathrm{sus}}$ and solid $c_{D,p,\mathrm{sus}}$ drag contributions of suspensions with different materials and how they compare to the equivalent single phase fluid or granular flow respectively. The particle contribution $c_{D,p,\mathrm{sus}}$ in Fig. 5.15 is small for neutrally buoyant particles but grows with increasing density ratios. For suspensions of hydrogel and glass particles, the drag coefficient is equal to the single phase $c_{D,\mathrm{sp}}$ at corresponding effective Reynolds number. The same estimate is valid for iron but only in the steady regime.

When $\mathrm{Re}_{\mathrm{eff}} > \mathrm{Re}_{\mathrm{crit}}(\Theta = 0)$ a suspension of iron particles can neither be described as an effective single phase steady nor unsteady flow, nor as granular media. At high density ratios the particle influence on the drag force dominates, but the fluid part cannot be neglected. The equivalent fluid model is no longer applicable, instead the suspension drag is approximately equal to the pure granular drag $c_{D,g}$.

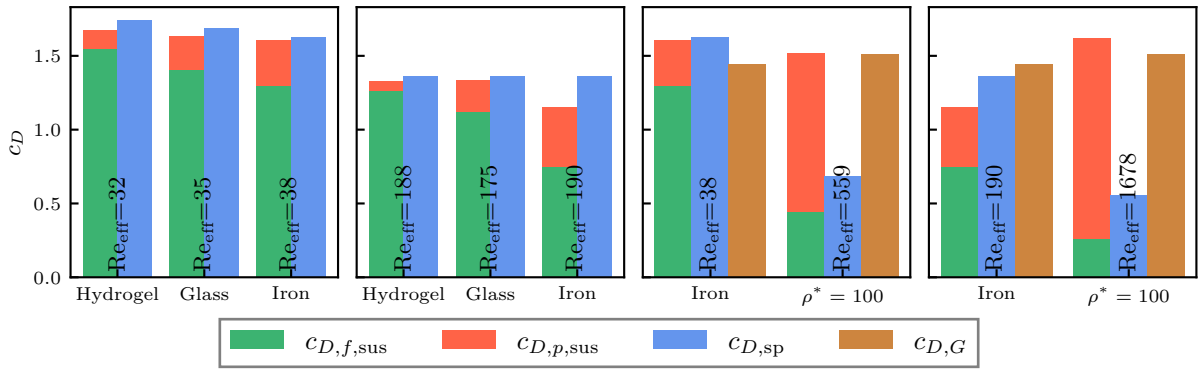

Figure 5.15 – Fluid $c_{D,f,\mathrm{sus}}$ and particle $c_{D,p,\mathrm{sus}}$ contributions to suspension drag coefficient compared to single phase drag $c_{D,\mathrm{sp}}$, granular drag $c_{D,g}$. All suspensions contain $\Theta = 20\%$ solid volume. Single phase drag coefficient at $\mathrm{Re} > 200$ is an extrapolation from obtained simulation results.

The observations on the drag also manifest in the local distribution of particles in the instantaneous flow field, showed in Fig. 5.16. The fluid viscosity is kept constant while the density ratio changes, leading to different Stokes numbers $\mathrm{Stk} = \frac{\tau_p u_\infty}{D}$ with $\tau_p = \frac{\left(\rho_p + \rho_f/2\right) d^2}{18 \mu_f}$. We can identify four unique flow states. Hydrogel particles are uniformly distributed throughout the domain, even in vortex regions. On the other hand, glass particles at $\mathrm{Stk} = 1$ yield vortices depleted of particles. For low Stokes numbers $\mathrm{Stk} \leq 1$ no bow shock is present. For the heavier iron particles we observe that vortex shedding is spatially delayed downstream due to the formation of a subtle bow shock. The wake region and vortices are largely depleted of particles. When the Stokes number increases further to $\mathrm{Stk} > 10$, the wake is completely free of particles and an apparent bow shock is visible similar to dry granular flow. Vortex shedding is stalled or delayed so far that it is outside of the simulation domain. Shi et al. [167] conducted numerical studies of one-way coupled particle laden flows around a cylinder for high density ratios $\rho^* = 1000$ and low volume fraction $\Theta = 10^{-6}$. The bow shock observed in their simulations is wider than ours and fluid vortex shedding is not inhibited by particle inertia, since the fluid is not influenced by the presence of particles. But we notice the same downstream delay of vortex shedding in terms of the particles. Similarly the results of Luo et al. [168] show unsteady vortex shedding for Stokes numbers up to 100. They examined dilute flows with high density ratios and a one-way fluid-particle coupling, where only Stokes drag force is considered. In agreement with our results, there is a depletion of particles in vortex regions and an extended recirculation zone for $\mathrm{Stk} > 1$. Snapshots from computations of pure granular flows can be found in the work of Jalali [165], which depict a bow shock that is comparable to our high density particles.

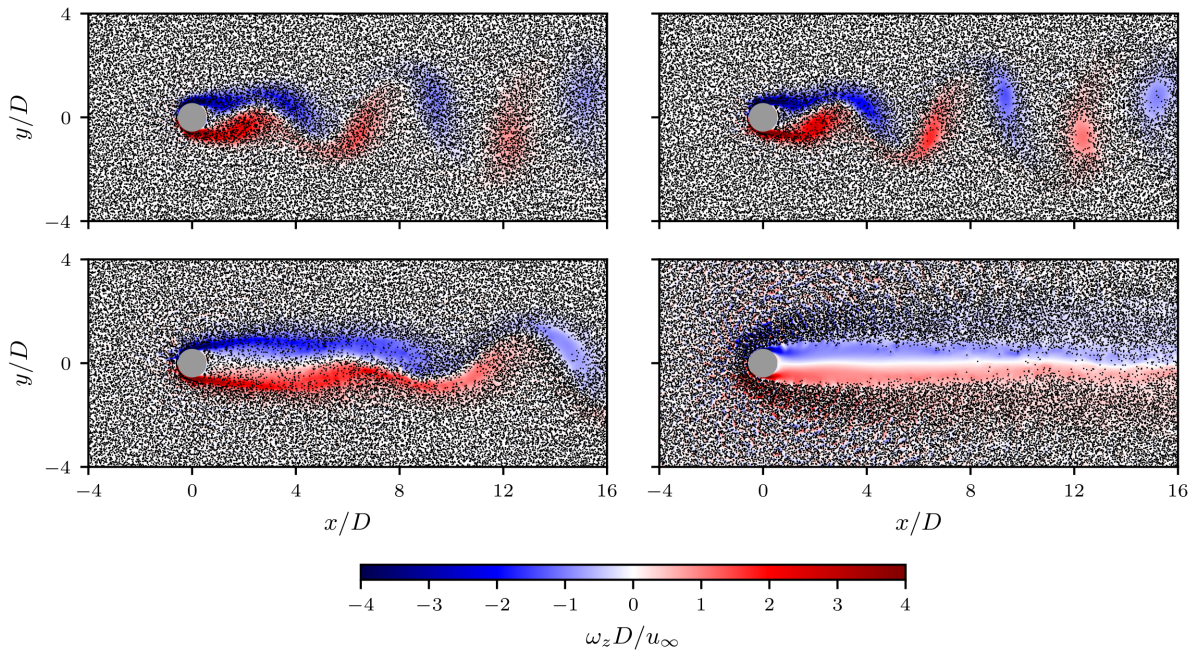

Figure 5.16 – Snapshot of particle positions and vorticity field at volume fraction $\Theta = 20\%$. Hydrogel (Stk = 0.5): top/left; Glass (Stk = 1): top/right; Iron (Stk = 2.8): bottom/left; $\rho^* = 100$ (Stk = 33.5): bottom/right.

5.5 Performance aspects

The computational speed of our LBM-DEM approach will be presented in Million Lattice Updates Per Second (MLUPS) in this section. This number involves not only the fluid solver but the granular solver and all routines necessary for the coupling of these two. For single phase, we achieve 5620 MLUPS on 15 nodes on the *Intel Cascade Lake 6248* architecture of the *Jean Zay* supercomputer[1]. When introducing Lagrangian particles into the domain, the additional treatment of collisions, particles boundary conditions and refilling of missing distribution functions slow down the performance to 1580 MLUPS at 20% volume fraction. To complete a typical simulation of 200,000 time steps on 600 cores a total of 3660 (resp, 13030) CPU hours are required at $\Theta = 0\%$ (resp., 20%), corresponding to a size ratio $D/d = 5$. These numbers do not include post processing routines. The number of lattice cells for simulations at size ratio $D/d = 10$ amounts to 4,800 M with over 1.8 M particles inside the computational domain at 20% solid volume fraction. These larger computations were performed on the *OCCIGEN* supercomputer[2] with *Intel Haswell E5-2690V3* architecture using 4,800 cores.

We investigate the change in performance for increasing particle volume fraction in Fig. 5.17. At $\Theta = 0.05$ the overall computational speed of the fully coupled algorithm is roughly 40% lower compared to the single phase and at $\Theta = 0.20$ the speed is reduced by more than two thirds. These numbers correspond to simulations of hydrogel particles with $d/\Delta x = 10$ and $D/d = 5$. We recall that the LBM algorithm iterates over all grids cells, regardless of the cell status. Consequently the performance of the fluid solver stays constant when introducing particles in the flow, but the number of bodies treated by the granular solver and the number of

[1] `http://www.idris.fr/eng/jean-zay/`

[2] `https://www.cines.fr/en/supercomputing-2/hardwares/the-supercomputer-occigen/`

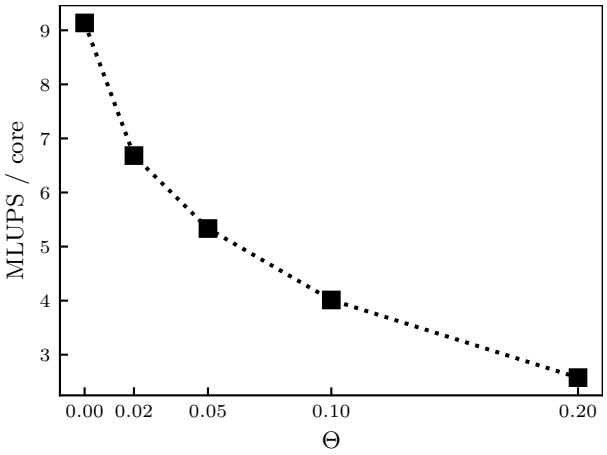

Figure 5.17 – Performance of the fully coupled algorithm for varying particle volume fraction on the *Jean Zay* supercomputer.

.

boundary cells at the fluid-solid interface increases. Fig. 5.18 shows the percentage of consumed CPU time of the three main components of the algorithm. The percentage of the fluid solver decreases proportionally with the particle volume fraction, whereas the granular percentage is almost constant when particles are present. The most CPU time at high volume fractions is consumed by the treatment of boundary conditions. Not shown here are contributions of the distribution functions refilling scheme, whose proportional consumption increases slightly from 4% to 6% between $\Theta = 0.02$ and $\Theta = 0.20$. Additionally the continuous mapping of particles into the simulation domain uses considerably more CPU time, increasing from 3% to 12% between $\Theta = 0.02$ and $\Theta = 0.20$.

Another important aspect of this configuration in terms of computational efficiency is the parallel scaling. For this test we use slightly smaller dimensions, such that the required memory will fit on a single computing node on the *Jean Zay* supercomputer. The simulations domain spans $L_x, L_y, L_z = 32D, 20D, 4D$ and contains 10% in volume of hydrogel particles with size $d/\Delta x = 8$ at a cylinder to sphere size ratio $D/d = 5$. We consider three different scaling modes:

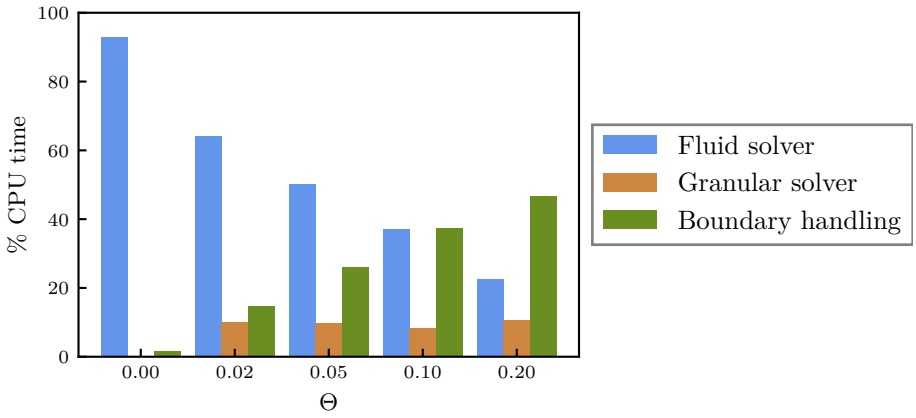

Figure 5.18 – CPU time distribution of main components of the coupled algorithm for increasing particle volume fraction

.

- Weak scaling: Domain, cylinder and particle size increase proportionally to the number of cores used
- Strong scaling: Domain cylinder and particle size stay constant
- A scaling which is specific to this configuration: Domain and cylinder increase proportionally to the number of cores used but particles keep the same size

As the number of cores increases by a factor of 8, the cylinder diameter, particle diameter and domain size doubles during weak scaling. The number of grid cells per block remains constant for weak and configuration specific scaling, but reduces during strong scaling. One block holds $128^3, 64^3, 32^3, 16^3$ cells at 1, 8, 64, 512 nodes respectively in the strong scaling mode. Fig. 5.19 illustrates the nearly ideal parallel scaling of our approach until 20480 cores for weak and configuration specific scaling. During weak scaling the performance can surpass ideal scaling because larger particles entail fewer boundary cells than smaller particles at the same volume fraction, which reduces the proportional CPU consumption of the boundary handling routine. The loss of efficiency in strong scaling can be attributed to the increased communication between processes. At 20480 cores, the computational speed is reduced by 72% compared to 40 cores. A block size of 32^3 is generally a good target value, while 16^3 is too small to guarantee good performance.

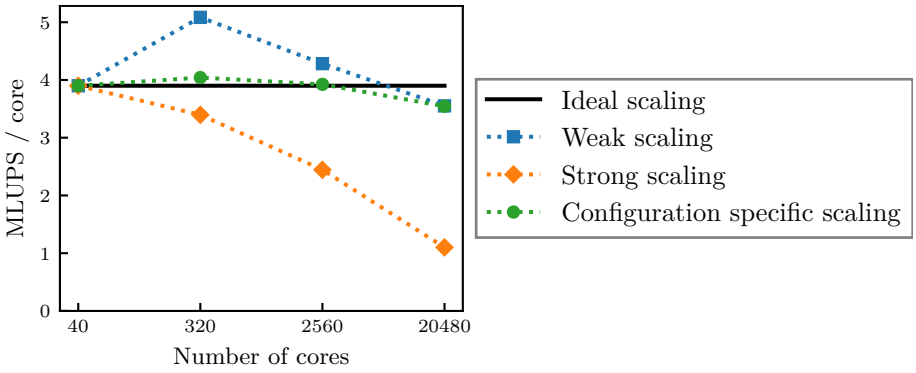

Figure 5.19 – Parallel scaling of the fully coupled algorithm for hydrogel particles with $\Theta = 0.10$, $d/\Delta x = 8$ and $D/d = 5$ using 1, 8, 64, 512 nodes on the *Jean Zay* supercomputer

5.6 Conclusions

This study utilizes efficient capabilities of the LBM to simulate particle-laden flows. Particle resolved simulations allow to investigate the unsteady response of particulate flows around a circular cylinder. To validate the computational model several configurations have been tested, such as single phase flow past a cylinder, granular drag coefficients and particle response to unsteady and shear forces. Our LBM-DEM delivers high accuracy since it is based on geometrically resolved moving bodies, while remaining sufficiently efficient to perform large simulations with hundreds of thousands of particles in decent computation time on a supercomputer.

The predicted global flow parameters using an effective viscosity are well recovered for neutrally buoyant and slightly inertial particles (typically glass beads in water) at a cylinder sphere diameter ratio equal to 5. Decreasing the particle size relative to the cylinder did not significantly change the drag coefficient and recirculation length predictions, except for points close to the onset of unsteady vortex shedding. We observe that steady wake is depleted of neutrally-buoyant particle as previously observed in microfluidic experiments while higher Reynolds flows are unsteady and von-Karman vortices are populated with particles because their Stokes number is low. Increasing particle inertia shows that the simple modeling of dispersed two-phase flows with mixture physical properties is not adequate to predict the drag force experienced by the cylinder.

Suspensions with relative density higher than 2.5 are more complex to describe due to the interplay between hydrodynamic and granular effects. In the steady regime, suspension flows exert a drag force similar to an equivalent fluid, but in the unsteady regime the evolution of the drag coefficient neither follows the prediction based on an equivalent fluid, nor as a granular flow. Inertia of particles forces them to cross the flow streamlines, leading to a stabilization of the wake zone depleted of particles and delaying the development of vortices. This yields global flow parameters to evolve in an intermediate regime between unsteady and steady response. We have observed that the spatial distribution of particles is depending on the Stokes number characterizing the response time of particles. When Stokes number is equal to one or larger, the vortices are depleted of particles. Further simulations and experiments will be necessary to better predict flow parameters with a composite law including both hydrodynamic and granular features of suspensions at moderate relative densities.

At specific density ratios of $\mathcal{O}(100)$ or higher, the suspension largely resembles a granular flow, and a bow shock is present. The onset of von-Karman street is delayed. Drag coefficients are closer to the prediction for a dry granular material, even though the fluid contribution cannot be completely neglected.

Chapter 6

Conclusions

6.1 Summary

The LBM is an alternative approach to solve hydrodynamic flow problems in an efficient manner. While thermal and compressible flows remain difficult to handle and are an ongoing field of research, this PhD work has put the focus on flows in the incompressible or weakly compressible regimes. We were interested at flows from the Stokes regime (low Reynolds number) to turbulent flows (high Reynolds number) and the coupling to a granular solver for simulating a dispersed particle phase. Several test configurations were conducted and compared to analytic or empirical predictions to verify the validity and the accuracy of our simulation techniques.

The code generation technique offered by waLBerla and *lbmpy* allows to execute different collision operators (BGK, TRT, MRT, cumulants), include a SGS turbulence model or entropic stabilization in the "stream & collide" scheme without loss of performance. On a uniform grid with sufficiently large block size, the performance is optimized to attain the limit predicted by the roofline model.

It was not possible to maintain this performance for a complex geometry with multiple levels of refinement. That is a shortcoming that we found for the swirler simulations. Nevertheless, the comparison with ProLB and AVBP has demonstrated the potential of the block structured grid layout. All three codes were able to obtain highly accurate velocity profiles in terms of mean and RMS quantities, but it remains a difficult tasks to obtain the correct prediction of pressure loss with the non-body-fitted mesh, that is inherent to the LBM. Simulating the unconfined swirler configuration required a finer mesh resolution and even then it was difficult to capture the peaks in the mean radial velocity. We observed less energy dissipation in the high frequency range for the two LBM codes compared to the finite volume solver AVBP. While waLBerla performed 3 to 5 times faster in terms of reduced efficiency, it suffers from two drawbacks compared to the solvers using unstructured grids. Firstly, the refinement of whole blocks instead of single cells (as is the case in ProLB) limits the flexibility of refining the mesh spatially, which leads to more grid cells being required to obtain equivalent spatial accuracy. Secondly, the concept of iterating on the whole block irrespective of the cells residing inside the domain or not generates an overhead of non-fluid cells. Whether or not the higher computational efficiency outweighs the excess amount of cells is not obvious and will depend on the specific geometry. The code efficiency and the simplicity of creating a mesh for waLBerla makes it an ideal candidate for when results are needed quickly.

We investigated the transition to unsteadiness of particulate flows around an obstacle. Simulations of particle resolved dynamics with up to 4,800 million grid cells and 1.8 million spher-

ical particles have been carried out for different flow regimes and dilute to semi-dilute particle concentrations. Particles are fully-coupled meaning that fluid-particle and particle-particle interactions plus the feedback effect of particles on the fluid flow are resolved down to the particle scale. We observed that flow regimes with neutrally-buoyant particles can be rationalized by means of mixture material properties. Global flow parameters like drag and lift coefficients or the mean recirculation length are equal to single phase value at corresponding effective Reynolds number. The presence of particles trigger flow unsteadiness without shedding vortices at subcritical Reynolds number. Increasing the inertia of the particles leads to a progressive transition to granular flow and an increased particle collision contribution to the drag force. At a relative particle density 2.5 we observe the depletion of particles from the vortices in the wake; at relative density 7.8 the prediction with mixture material properties is no longer valid and vortex shedding is delayed downstream; at relative density 100 the formation of a bow shock and a complete particle depletion of the wake occurs. A cylinder to particle diameter ratio of 5 was sufficient to obtain accurate flow predictions. The scaling capabilities of the fully coupled approach for up to 512 nodes (20480 cores) on the *Jean Zay* supercomputer were demonstrated.

6.2 Outlook

Evidently, the next step would be to study particle-laden, turbulent flows. While particle resolved simulations of swirling flows seemed unfeasible in the past, they might become a reality in the near future. Let us entertain the idea of injecting spherical liquid droplets of size 100 μm into the swirler configuration of Chap. 4. Adhering to the earlier proposed minimum particle size $d/\Delta x = 10$, the required mesh resolution is 10 μm. Assuming that the code scales ideally, the cost of a simulation of 5% particle volume and 100 ms of physical time will be approximately 7.5 M CPU-hours. Today, we would have to use the entire computing power of the SuperMUC-NG cluster[1] to perform this simulation in 24 hours (the newer Intel Skylake Xeon Platinum 8174 of SuperMUC-NG will perform better than the CPU of Kraken or Jean Zay). In the future this type of simulation will also become possible on smaller computing clusters.

To make waLBerla competitive in the context of industrial applications at very high Reynolds numbers, an explicit model for the logarithmic law of the wall (e.g. [188]) will be necessary. Moreover, non-reflecting boundary conditions such as the NSCBC in AVBP are essential for damping spurious acoustic reflections and stabilizing the flow. Recursive Regularized (RR) and Hybrid Recursive Regularized (HRR) collision operators have demonstrated good properties and can be included in the code generation process of *lbmpy*. Incorporating these features within waLBerla has the potential to create a highly efficient code with good stability and accuracy to challenge software, that is already used in industry, such as ProLB and AVBP.

[1] `https://doku.lrz.de/display/PUBLIC/Hardware+of+SuperMUC-NG`

Bibliography

[1] Sydney Chapman. "On the law of distribution of molecular velocities, and on the theory of viscosity and thermal conduction, in a non-uniform simple monatomic gas". In: *Philosophical Transactions of the Royal Society of London. Series A, Containing Papers of a Mathematical or Physical Character* 216 (538-548 1916), pp. 279–348.

[2] David Enskog. "Kinetische Theorie der Vorgänge in mässig verdünnten Gasen." ger. PhD thesis. 1917.

[3] P. L. Bhatnagar, E. P. Gross, and M. Krook. "A Model for Collision Processes in Gases. I. Small Amplitude Processes in Charged and Neutral One-Component Systems". en. In: *Phys. Rev.* 94.3 (1954), pp. 511–525. DOI: 10.1103/PhysRev.94.511.

[4] U. Frisch, B. Hasslacher, and Y. Pomeau. "Lattice-Gas Automata for the Navier-Stokes Equation". In: *Phys. Rev. Lett.* 56 (14 1986), pp. 1505–1508. DOI: 10.1103/PhysRevLett.56.1505.

[5] Li Chen et al. "A critical review of the pseudopotential multiphase lattice Boltzmann model: Methods and applications". In: *International Journal of Heat and Mass Transfer* 76 (2014), pp. 210–236. DOI: https://doi.org/10.1016/j.ijheatmasstransfer.2014.04.032.

[6] Huili Wang et al. "A brief review of the phase-field-based lattice Boltzmann method for multiphase flows". In: *Capillarity* 2 (2019), pp. 33–52. DOI: 10.26804/capi.2019.03.01.

[7] M. Wöhrwag et al. "Ternary Free-Energy Entropic Lattice Boltzmann Model with a High Density Ratio". In: *Phys. Rev. Lett.* 120 (23 2018), p. 234501. DOI: 10.1103/PhysRevLett.120.234501.

[8] Simon Marié, Denis Ricot, and Pierre Sagaut. "Comparison between lattice Boltzmann method and Navier–Stokes high order schemes for computational aeroacoustics". In: *Journal of Computational Physics* 228.4 (2009), pp. 1056–1070. DOI: https://doi.org/10.1016/j.jcp.2008.10.021.

[9] Linlin Fei and Kai Hong Luo. "Cascaded lattice Boltzmann method for incompressible thermal flows with heat sources and general thermal boundary conditions". In: *Computers & Fluids* 165 (2018), pp. 89–95. DOI: https://doi.org/10.1016/j.compfluid.2018.01.020.

[10] Andreas Lintermann and Wolfgang Schröder. "Lattice–Boltzmann simulations for complex geometries on high-performance computers". In: *CEAS Aeronautical Journal* 11 (3 2020), pp. 745–766. DOI: 10.1007/s13272-020-00450-1.

[11] S. Guo et al. "An efficient lattice Boltzmann method for compressible aerodynamics on D3Q19 lattice". In: *Journal of Computational Physics* 418 (2020), p. 109570. DOI: https://doi.org/10.1016/j.jcp.2020.109570.

[12] Jonas Latt et al. "Efficient supersonic flow simulations using lattice Boltzmann methods based on numerical equilibria". In: *Philosophical Transactions of the Royal Society A Mathematical Physical and Engineering Sciences* 378, 20190559 (2175 2020), p. 20190559. DOI: 10.1098/rsta.2019.0559.

[13] Florian Renard et al. "Improved compressible hybrid lattice Boltzmann method on standard lattice for subsonic and supersonic flows". In: *Computers & Fluids* 219 (2021), p. 104867. DOI: https://doi.org/10.1016/j.compfluid.2021.104867.

[14] M.D. Mazzeo and P.V. Coveney. "HemeLB: A high performance parallel lattice-Boltzmann code for large scale fluid flow in complex geometries". In: *Computer Physics Communications* 178.12 (2008), pp. 894–914. DOI: https://doi.org/10.1016/j.cpc.2008.02.013.

[15] C.A. Niedermeier, C.F. Janssen, and T. Indinger. "Massively-parallel multi-GPU simulations for fast and accurate automotive aerodynamics". en. In: *6th ECCOMAS European Conference on Computational Mechanics: Solids, Structures and Coupled Problems, ECCM 2018 and 7th ECCOMAS European Conference on Computational Fluid Dynamics, ECFD 2018*. Scottish Events CampusGlasgow; United Kingdom: International Centre for Numerical Methods in Engineering, CIMNE, 2020.

[16] Christoph Riesinger et al. "A Holistic Scalable Implementation Approach of the Lattice Boltzmann Method for CPU/GPU Heterogeneous Clusters". In: *Computation* 5.4 (2017). DOI: 10.3390/computation5040048.

[17] Rainald Löhner. "Towards overcoming the LES crisis". In: *International Journal of Computational Fluid Dynamics* 33.3 (2019), pp. 87–97. DOI: 10.1080/10618562.2019.1612052.

[18] Zhao Liu et al. "SunwayLB: Enabling Extreme-Scale Lattice Boltzmann Method Based Computing Fluid Dynamics Simulations on Sunway TaihuLight". In: *2019 IEEE International Parallel and Distributed Processing Symposium (IPDPS)*. 2019, pp. 557–566. DOI: 10.1109/IPDPS.2019.00065.

[19] Sebastian Geller et al. "Benchmark computations based on lattice-Boltzmann, finite element and finite volume methods for laminar flows". In: *Computers & Fluids* 35.8 (2006). Proceedings of the First International Conference for Mesoscopic Methods in Engineering and Science, pp. 888–897. DOI: https://doi.org/10.1016/j.compfluid.2005.08.009.

[20] Karl-Robert Wichmann et al. "A runtime based comparison of highly tuned lattice Boltzmann and finite difference solvers". In: *The International Journal of High Performance Computing Applications* (2021). DOI: 10.1177/10943420211006169.

[21] Christian Godenschwager et al. "A framework for hybrid parallel flow simulations with a trillion cells in complex geometries". In: *SC '13: Proceedings of the International Conference on High Performance Computing, Networking, Storage and Analysis*. ACM Press, 2013, pp. 1–12. DOI: 10.1145/2503210.2503273.

[22] Christian Feichtinger et al. "WaLBerla: HPC software design for computational engineering simulations". In: *Journal of Computational Science* 2.2 (2011), pp. 105–112. DOI: https://doi.org/10.1016/j.jocs.2011.01.004.

[23] J. Götz et al. "Coupling multibody dynamics and computational fluid dynamics on 8192 processor cores". In: *Parallel Computing* 36.2 (2010), pp. 142–151. DOI: https://doi.org/10.1016/j.parco.2010.01.005.

[24] Florian Schornbaum and Ulrich Rüde. "Massively Parallel Algorithms for the Lattice Boltzmann Method on NonUniform Grids". In: *SIAM Journal on Scientific Computing* 38.2 (2016), pp. C96–C126. DOI: 10.1137/15M1035240.

[25] Dominik Bartuschat and Ulrich Rüde. "Parallel multiphysics simulations of charged particles in microfluidic flows". In: *Journal of Computational Science* 8 (2015), pp. 1–19. DOI: https://doi.org/10.1016/j.jocs.2015.02.006.

[26] Christoph Rettinger and Ulrich Rüde. "A comparative study of fluid-particle coupling methods for fully resolved lattice Boltzmann simulations". In: *Computers & Fluids* (2017).

[27] Martin Bauer, Harald Köstler, and Ulrich Rüde. "lbmpy: Automatic code generation for efficient parallel lattice Boltzmann methods". In: *Journal of Computational Science* 49 (2021), p. 101269. DOI: https://doi.org/10.1016/j.jocs.2020.101269.

[28] L. D. Landau and E. M. Lifshitz. *Fluid Mechanics*. Second. Vol. 6. Course of Theoretical Physics. Pergamon Press, 1987.

[29] D. J. Acheson. *Elementary fluid dynamics*. Oxford applied mathematics and computing science series. Oxford : New York: Clarendon Press ; Oxford University Press, 1990.

[30] Joseph Boussinesq. *Application des potentiels à l'étude de l'équilibre et du mouvement des solides élastiques, principalement au calcul des déformations et des pressions que produisent, dans ces solides, des efforts quelconques exercés sur une petite partie de leur surface ou de leur intérieur : mémoire suivi de notes étendues sur divers points de physique mathématique et d'analyse*. Tech. rep. Impr. L. Danel (Lille), 1885.

[31] Alfred Barnard Basset. "III. On the motion of a sphere in a viscous liquid". en. In: *Philosophical Transactions of the Royal Society of London. (A.)* 179 (1888), pp. 43–63. DOI: 10.1098/rsta.1888.0003.

[32] G. Segré and A. Silberberg. "Radial Particle Displacements in Poiseuille Flow of Suspensions". en. In: *Nature* 189.4760 (1961), pp. 209–210. DOI: 10.1038/189209a0.

[33] S.B. Pope et al. *Turbulent Flows*. Cambridge University Press, 2000.

[34] Leonhard Euler. "Principes généraux du mouvement des fluides". In: *Mémoires de l'académie des sciences de Berlin* 11 (1757), pp. 274–315.

[35] Augustin Louis Cauchy. "Sur l'équilibre et le mouvement des liquides et des fluides élastiques". In: *Mémoire de l'Académie Royale des Sciences* 11 (1829), pp. 413–418.

[36] George Gabriel Stokes. "On the effect of the internal friction of fluids on the motion of pendulums". In: *Transactions of the Cambridge Philosophical Society* 8 (1845), pp. 287–305.

[37] P.A. Thompson. *Compressible-Fluid Dynamics*. McGraw-Hill, New York, 1972.

[38] S. Chapman and T.G. Cowling. "The Mathematical Theory of Non-uniform Gases. 2nd Edn." In: *The Mathematical Gazette* 38.323 (1952). DOI: 10.2307/3609795.

[39] James Clerk Maxwell. "IV. On the dynamical theory of gases". In: *Philosophical Transactions of the Royal Society of London* 157 (1867). Publisher: Royal Society, pp. 49–88. DOI: 10.1098/rstl.1867.0004.

[40] L. Boltzmann. *Weitere Studien über das Wärmegleichgewicht unter Gasmolekülen*. 1872.

[41] Tamas I. Gombosi. *Gaskinetic Theory*. Cambridge Atmospheric and Space Science Series. Cambridge University Press, 1994. DOI: 10.1017/CBO9780511524943.

[42] Sybren Ruurds de Groot and Peter Mazur. *Non-equilibrium thermodynamics*. eng. New York, NY: Dover Publications, 1984.

[43] Timm Krüger et al. *The lattice Boltzmann method: principles and practice*. New York, NY: Springer Berlin Heidelberg, 2016.

[44] R. Benzi, S. Succi, and M. Vergassola. "The lattice Boltzmann equation: theory and applications". In: *Physics Reports* 222.3 (1992), pp. 145–197. DOI: https://doi.org/10.1016/0370-1573(92)90090-M.

[45] Shiyi Chen and Gary D. Doolen. "Lattice Boltzmann Method for Fluid Flows". en. In: *Annual Review of Fluid Mechanics* 30.1 (1998), pp. 329–364. DOI: 10.1146/annurev.fluid.30.1.329.

[46] Sauro Succi. *The Lattice Boltzmann Equation: For Fluid Dynamics and Beyond*. Numerical Mathematics and Scientific Computation. Oxford, New York: Oxford University Press, 2001.

[47] Dieter A. Wolf-Gladrow. *Lattice-Gas Cellular Automata and Lattice Boltzmann Models: An Introduction*. en. Springer, 2005.

[48] Cyrus K. Aidun and Jonathan R. Clausen. "Lattice-Boltzmann Method for Complex Flows". en. In: *Annual Review of Fluid Mechanics* 42.1 (2010), pp. 439–472. DOI: 10.1146/annurev-fluid-121108-145519.

[49] Y. H Qian, D D'Humières, and P Lallemand. "Lattice BGK Models for Navier-Stokes Equation". In: *Europhysics Letters (EPL)* 17.6 (1992), pp. 479–484. DOI: 10.1209/0295-5075/17/6/001.

[50] Xiaoyi He and Li-Shi Luo. "Lattice Boltzmann Model for the Incompressible Navier–Stokes Equation". en. In: *Journal of Statistical Physics* 88.3 (1997), pp. 927–944. DOI: 10.1023/B:JOSS.0000015179.12689.e4.

[51] Dieter Hänel. *Molekulare Gasdynamik: Einführung in die kinetische Theorie der Gase und Lattice-Boltzmann-Methoden*. German. OCLC: 315785105. Berlin, Heidelberg: Springer-Verlag Berlin Heidelberg, 2004.

[52] Y. H Qian and S. A Orszag. "Lattice BGK Models for the Navier-Stokes Equation: Nonlinear Deviation in Compressible Regimes". In: 21.3 (1993), pp. 255–259. DOI: 10.1209/0295-5075/21/3/001.

[53] Xiaowen Shan, Xue-Feng Yuan, and Hudong Chen. "Kinetic theory representation of hydrodynamics: a way beyond the Navier–Stokes equation". In: *Journal of Fluid Mechanics* 550 (2006), pp. 413–441. DOI: 10.1017/S0022112005008153.

[54] Marc B. Reider and James D. Sterling. "Accuracy of discrete-velocity BGK models for the simulation of the incompressible Navier-Stokes equations". In: *Computers & Fluids* 24.4 (1995), pp. 459–467. DOI: https://doi.org/10.1016/0045-7930(94)00037-Y.

[55] David J Holdych et al. "Truncation error analysis of lattice Boltzmann methods". In: *Journal of Computational Physics* 193.2 (2004), pp. 595–619. DOI: https://doi.org/10.1016/j.jcp.2003.08.012.

[56] Irina Ginzburg, Dominique d'Humières, and Alexander Kuzmin. "Optimal Stability of Advection-Diffusion Lattice Boltzmann Models with Two Relaxation Times for Positive/Negative Equilibrium". en. In: *Journal of Statistical Physics* 139.6 (2010), pp. 1090–1143. DOI: 10.1007/s10955-010-9969-9.

[57] Irina Ginzburg, Frederik Verhaeghe, and Dominique d'Humieres. "Two-relaxation-time lattice Boltzmann scheme: About parametrization, velocity, pressure and mixed boundary conditions". In: *Communications in computational physics* 3.2 (2008), pp. 427–478.

[58] Dominique d'Humières. "Multiple–relaxation–time lattice Boltzmann models in three dimensions". In: *Physical and Engineering Sciences 360* 360 (1792 2002), pp. 437–451. DOI: https://doi.org/10.1098/rsta.2001.0955.

[59] Paul J. Dellar. "Bulk and shear viscosities in lattice Boltzmann equations". In: *Phys. Rev. E* 64 (3 2001), p. 031203. DOI: 10.1103/PhysRevE.64.031203.

[60] Pietro Asinari and Ilya V. Karlin. "Quasiequilibrium lattice Boltzmann models with tunable bulk viscosity for enhancing stability". In: *Phys. Rev. E* 81 (1 2010), p. 016702. DOI: 10.1103/PhysRevE.81.016702.

[61] Irina Ginzburg. "Study of Simple Hydrodynamic Solutions with the Two-Relaxation-Times Lattice Boltzmann Scheme". In: *Communications in Computational Physics* (2008).

[62] Martin Geier et al. "The cumulant lattice Boltzmann equation in three dimensions: Theory and validation". In: *Computers & Mathematics with Applications* 70.4 (2015), pp. 507–547. DOI: https://doi.org/10.1016/j.camwa.2015.05.001.

[63] Martin Geier, Andrea Pasquali, and Martin Schönherr. "Parametrization of the cumulant lattice Boltzmann method for fourth order accurate diffusion part I: Derivation and validation". In: *Journal of Computational Physics* 348 (2017), pp. 862–888. DOI: https://doi.org/10.1016/j.jcp.2017.05.040.

[64] Orestis Malaspinas and Pierre Sagaut. "Consistent subgrid scale modelling for lattice Boltzmann methods". In: *Journal of Fluid Mechanics* 700 (2012), pp. 514–542. DOI: 10.1017/jfm.2012.155.

[65] Pierre Sagaut. "Large Eddy Simulation for Incompressible Flows". In: (2006). DOI: 10.1007/b137536.

[66] J. Smagorinsky. "General Circulation Experiments with the Primitive Equations". EN. In: *Monthly Weather Review* 91.3 (1963). Publisher: American Meteorological Society Section: Monthly Weather Review, pp. 99–164. DOI: 10.1175/1520-0493(1963)091<0099:GCEWTP>2.3.CO;2.

[67] I. V. Karlin, F. Bösch, and S. S. Chikatamarla. "Gibbs' principle for the lattice-kinetic theory of fluid dynamics". In: *Phys. Rev. E* 90 (3 2014), p. 031302. DOI: 10.1103/PhysRevE.90.031302.

[68] B. Dorschner et al. "Entropic multi-relaxation time lattice Boltzmann model for complex flows". In: *Journal of Fluid Mechanics* 801 (2016), pp. 623–651. DOI: 10.1017/jfm.2016.448.

[69] Li-Shi Luo. "Lattice-Gas Automata and Lattice Boltzmann Equations for Two-Dimensional Hydrodynamics". PhD thesis. Georgia Institute of Technology, 1993.

[70] Li-Shi Luo. "Unified Theory of Lattice Boltzmann Models for Nonideal Gases". In: *Phys. Rev. Lett.* 81 (8 1998), pp. 1618–1621. DOI: 10.1103/PhysRevLett.81.1618.

[71] Zhaoli Guo, Chuguang Zheng, and Baochang Shi. "Discrete lattice effects on the forcing term in the lattice Boltzmann method". In: *Phys. Rev. E* 65 (4 2002), p. 046308. DOI: 10.1103/PhysRevE.65.046308.

[72] Ulf Daniel Schiller. "Thermal fluctuations and boundary conditions in the lattice Boltzmann method". PhD thesis. Johannes Gutenberg Universität Mainz, 2008.

[73] J. M. Buick and C. A. Greated. "Gravity in a lattice Boltzmann model". In: *Phys. Rev. E* 61 (5 2000), pp. 5307–5320. DOI: 10.1103/PhysRevE.61.5307.

[74] I. Ginzbourg and P. M. Adler. "Boundary flow condition analysis for the three-dimensional lattice Boltzmann model". In: *J. Phys. II France* 4.2 (1994), pp. 191–214. DOI: 10.1051/jp2:1994123.

[75] Anthony J. C. Ladd. "Numerical simulations of particulate suspensions via a discretized Boltzmann equation. Part 1. Theoretical foundation". In: *Journal of Fluid Mechanics* 271 (1994), pp. 285–309. DOI: 10.1017/S0022112094001771.

[76] Cyrus K. Aidun, Yannan Lu, and E.-Jiang Ding. "Direct analysis of particulate suspensions with inertia using the discrete Boltzmann equation". In: *Journal of Fluid Mechanics* 373 (1998), pp. 287–311.

[77] Binghai Wen et al. "Galilean invariant fluid–solid interfacial dynamics in lattice Boltzmann simulations". en. In: *Journal of Computational Physics* 266 (2014), pp. 161–170. DOI: 10.1016/j.jcp.2014.02.018.

[78] Shi Tao, Junjie Hu, and Zhaoli Guo. "An investigation on momentum exchange methods and refilling algorithms for lattice Boltzmann simulation of particulate flows". In: *Computers & Fluids* 133 (2016), pp. 1–14. DOI: https://doi.org/10.1016/j.compfluid.2016.04.009.

[79] Cheng Peng et al. "Implementation issues and benchmarking of lattice Boltzmann method for moving rigid particle simulations in a viscous flow". In: *Computers & Mathematics with Applications* 72.2 (2016), pp. 349–374. DOI: https://doi.org/10.1016/j.camwa.2015.08.027.

[80] Pierre Lallemand and Li-Shi Luo. "Lattice Boltzmann method for moving boundaries". In: *Journal of Computational Physics* 184.2 (2003), pp. 406–421. DOI: https://doi.org/10.1016/S0021-9991(02)00022-0.

[81] Alfonso Caiazzo. "Analysis of lattice Boltzmann nodes initialisation in moving boundary problems". In: *Progress in Computational Fluid Dynamics An International Journal* 8 (2008), pp. 3–10. DOI: 10.1504/PCFD.2008.018074.

[82] Haiping Fang et al. "Lattice Boltzmann method for simulating the viscous flow in large distensible blood vessels". In: *Phys. Rev. E* 65 (5 2002), p. 051925. DOI: 10.1103/PhysRevE.65.051925.

[83] Cheng Peng et al. "Implementation issues and benchmarking of lattice Boltzmann method for moving rigid particle simulations in a viscous flow". en. In: *Computers & Mathematics with Applications* 72.2 (2016), pp. 349–374. DOI: 10.1016/j.camwa.2015.08.027.

[84] P. A. Cundall and O. D. L. Strack. "A discrete numerical model for granular assemblies". In: *Géotechnique* 29.1 (1979), pp. 47–65. DOI: 10.1680/geot.1979.29.1.47.

[85] Samuel F. Foerster et al. "Measurements of the collision properties of small spheres". In: *Physics of Fluids* 6.3 (1994), pp. 1108–1115. DOI: 10.1063/1.868282.

[86] Tobias Kempe and Jochen Fröhlich. "Collision modelling for the interface-resolved simulation of spherical particles in viscous fluids". In: *Journal of Fluid Mechanics* 709 (2012), pp. 445–489. DOI: 10.1017/jfm.2012.343.

[87] Volker Becker, Thomas Schwager, and Thorsten Pöschel. "Coefficient of tangential restitution for the linear dashpot model". en. In: *Physical Review E* 77.1 (2008). DOI: 10.1103/PhysRevE.77.011304.

[88] Clayton Crowe et al. *Multiphase flows with droplets and particles*. CRC Press, 2011.

[89] Aman G. Kidanemariam and Markus Uhlmann. "Interface-resolved direct numerical simulation of the erosion of a sediment bed sheared by laminar channel flow". In: *International Journal of Multiphase Flow* 67 (2014), pp. 174–188. DOI: https://doi.org/10.1016/j.ijmultiphaseflow.2014.08.008.

[90] Martin Bauer et al. "waLBerla: A block-structured high-performance framework for multiphysics simulations". In: *Computers & Mathematics with Applications* 81 (2021), pp. 478–501. DOI: https://doi.org/10.1016/j.camwa.2020.01.007.

[91] Thomas Pohl et al. "Optimization and profiling of the cache performance of parallel lattice Boltzmann codes". In: *Parallel Processing Letters* 13.04 (2003), pp. 549–560. DOI: https://doi.org/10.1142/S0129626403001501.

[92] Christian Feichtinger et al. "Performance modeling and analysis of heterogeneous lattice Boltzmann simulations on CPU–GPU clusters". In: *Parallel Computing* 46 (2015), pp. 1–13. DOI: https://doi.org/10.1016/j.parco.2014.12.003.

[93] Zhao Liu et al. "Sunwaylb: Enabling extreme-scale lattice boltzmann method based computing fluid dynamics simulations on sunway taihulight". In: *2019 IEEE International Parallel and Distributed Processing Symposium (IPDPS)*. IEEE. 2019, pp. 557–566. DOI: https://doi.org/10.1109/IPDPS.2019.00065.

[94] Thomas Pohl et al. "Performance evaluation of parallel large-scale lattice Boltzmann applications on three supercomputing architectures". In: *SC'04: Proceedings of the 2004 ACM/IEEE Conference on Supercomputing*. IEEE. 2004, pp. 21–21. DOI: https://doi.org/10.1109/SC.2004.37.

[95] Samuel Williams, Andrew Waterman, and David Patterson. "Roofline: an insightful visual performance model for multicore architectures". In: *Communications of the ACM* 52.4 (2009), pp. 65–76. DOI: 10.1145/1498765.1498785.

[96] M. Wittmann et al. "Lattice Boltzmann benchmark kernels as a testbed for performance analysis". In: *Computers & Fluids* 172 (2018), pp. 582–592. DOI: https://doi.org/10.1016/j.compfluid.2018.03.030.

[97] M. Rohde et al. "A generic, mass conservative local grid refinement technique for lattice-Boltzmann schemes". In: *International Journal for Numerical Methods in Fluids* 51.4 (2006), pp. 439–468. DOI: https://doi.org/10.1002/fld.1140.

[98] Anthony JC Ladd. "Numerical simulations of particulate suspensions via a discretized Boltzmann equation. Part 1. Theoretical foundation". In: *Journal of fluid mechanics* 271 (1994), pp. 285–309.

[99] K. Stewartson. "On the impulsvie motion of a flat plate in a viscous fluid". In: *The Quarterly Journal of Mechanics and Applied Mathematics* 4.2 (1951), pp. 182–198. DOI: 10.1093/qjmam/4.2.182.

[100] G.K. Batchelor. *An Introduction to Fluid Dynamics*. Cambridge mathematical library. Cambridge University Press, 2000.

[101] Jacques Magnaudet, Mayela Rivero, and Jean Fabre. "Accelerated flows past a rigid sphere or a spherical bubble. Part 1. Steady straining flow". In: *Journal of Fluid Mechanics* 284 (1995), pp. 97–135. DOI: 10.1017/S0022112095000280.

[102] R. Gatignol. "The Faxén formulae for a rigid particle in an unsteady non-uniform Stokes flow". In: *Journal de mécanique théorique et appliquée* 2.2 (1983), pp. 143–160.

[103] Martin R. Maxey and James J. Riley. "Equation of motion for a small rigid sphere in a nonuniform flow". In: *The Physics of Fluids* 26.4 (1983), pp. 883–889. DOI: 10.1063/1.864230.

[104] Guiquan Wang, Micheline Abbas, and Eric Climent. "Modulation of large-scale structures by neutrally buoyant and inertial finite-size particles in turbulent Couette flow". In: *Phys. Rev. Fluids* 2 (8 2017), p. 084302. DOI: 10.1103/PhysRevFluids.2.084302.

[105] Isabelle Calmet and Jacques Magnaudet. "Large-eddy simulation of high-Schmidt number mass transfer in a turbulent channel flow". In: *Physics of Fluids* 9.2 (1997), pp. 438–455. DOI: 10.1063/1.869138.

[106] M. Maxey and B. Patel. "Localized force representations for particles sedimenting in Stokes flow". In: *International Journal of Multiphase Flow* 27 (2001), pp. 1603–1626.

[107] Sune Lomholt and Martin R. Maxey. "Force-Coupling Method for Particulate Two-Phase Flow: Stokes Flow". In: *J. Comput. Phys.* 184.2 (2003), pp. 381–405. DOI: 10.1016/S0021-9991(02)00021-9.

[108] Éric Climent and Martin R. Maxey. "The force coupling method: A flexible approach for the simulation of particulate flows". In: *Theoretical Methods for Micro Scale Viscous Flows*. Ed. by François Feuillebois and Antoine Sellier. Thanks to Transworld Research Network. Theoretical Methods for Micro Scale Viscous Flows is available at http://www.trnres.com/. Kerala, India: Transworld Research Network, 2009, pp. 1–21.

[109] Evgeny S. Asmolov. "The inertial lift on a spherical particle in a plane Poiseuille flow at large channel Reynolds number". en. In: *Journal of Fluid Mechanics* 381 (1999), pp. 63–87. DOI: 10.1017/S0022112098003474.

[110] Vincent Loisel et al. "The effect of neutrally buoyant finite-size particles on channel flows in the laminar-turbulent transition regime". In: *Physics of Fluids* 25.12 (2013), p. 123304. DOI: 10.1063/1.4848856.

[111] Siarhei Khirevich, Irina Ginzburg, and Ulrich Tallarek. "Coarse- and fine-grid numerical behavior of MRT/TRT lattice-Boltzmann schemes in regular and random sphere packings". en. In: *Journal of Computational Physics* 281 (2015), pp. 708–742. DOI: 10.1016/j.jcp.2014.10.038.

[112] C. R. Wassgren et al. "Dilute granular flow around an immersed cylinder". In: *Physics of Fluids* 15.11 (2003), pp. 3318–3330. DOI: 10.1063/1.1608937.

[113] Volkhard Buchholtz and Thorsten Pöschel. "Interaction of a granular stream with an obstacle". In: *Granular Matter* 1.1 (1998), pp. 33–41. DOI: 10.1007/PL00010908.

[114] J. F. Boudet and H. Kellay. "Drag Coefficient for a Circular Obstacle in a Quasi-Two-Dimensional Dilute Supersonic Granular Flow". In: *Phys. Rev. Lett.* 105 (10 2010), p. 104501. DOI: 10.1103/PhysRevLett.105.104501.

[115] Johan Meyers and Pierre Sagaut. "Evaluation of Smagorinsky variants in large-eddy simulations of wall-resolved plane channel flows". In: *Physics of Fluids* 19.9 (2007), p. 095105. DOI: 10.1063/1.2768944.

[116] Hatem Touil, Denis Ricot, and Emmanuel Lévêque. "Direct and large-eddy simulation of turbulent flows on composite multi-resolution grids by the lattice Boltzmann method". In: *Journal of Computational Physics* 256 (2014), pp. 220–233. DOI: 10.1016/j.jcp.2013.07.037.

[117] Robert D. Moser, John Kim, and Nagi N. Mansour. "Direct numerical simulation of turbulent channel flow up to $\mathrm{Re}_\tau = 590$". In: *Physics of Fluids* 11.4 (1999), pp. 943–945. DOI: 10.1063/1.869966.

[118] Andrea Aniello et al. "Comparison among Lattice Boltzmann and finite volume solvers for swirled confined flows". In: *Computer & Fluids* (2020).

[119] P Sagaut and S Deck. "Large eddy simulation for aerodynamics: status and perspectives". In: *Philosophical Transactions of the Royal Society A: Mathematical, Physical and Engineering Sciences* 367.1899 (2009), p. 2849. DOI: https://doi.org/10.1098/rsta.2008.0269.

[120] Z. Wang et al. "High-Order CFD Methods: Current Status and Perspective". In: *International Journal for Numerical Methods in Fluids* 72 (2013), pp. 811–845. DOI: https://doi.org/10.1002/fld.3767.

[121] *Comparison of Various CFD Codes for LES Simulations of Turbomachinery: From Inviscid Vortex Convection to Multi-Stage Compressor*. Vol. Volume 2C: Turbomachinery. Turbo Expo: Power for Land, Sea, and Air. 2018. DOI: 10.1115/GT2018-75523.

[122] Marco Gatti et al. "Impact of swirl and bluff-body on the transfer function of premixed flames". In: *Proceedings of the Combustion Institute* 37 (2019), pp. 5197–5204. DOI: https://doi.org/10.1016/j.proci.2018.06.148.

[123] Fabien Dupuy et al. "Combining analytical models and LES data to determine the transfer function from swirled premixed flames". In: *Combustion and Flame* 217 (2020), pp. 222–236. DOI: https://doi.org/10.1016/j.combustflame.2020.03.026.

[124] Thilo Schonfeld and Michael Rudgyard. "Steady and unsteady flow simulations using the hybrid flow solver AVBP". In: *AIAA journal* 37.11 (1999), pp. 1378–1385. DOI: https://doi.org/10.2514/2.636.

[125] O. Colin and M. Rudgyard. "Development of high-order Taylor-Galerkin schemes for unsteady calculations". In: *J. Comp. Physics* 162.2 (2000), pp. 338–371. DOI: https://doi.org/10.1006/jcph.2000.6538.

[126] T. Poinsot. "Prediction and control of combustion instabilities in real engines (Invited Hottel lecture)". In: *Proc. Comb. Inst.* (2017), pp. 1–28. DOI: http://dx.doi.org/10.1016/j.proci.2016.05.007.

[127] O. Vermorel, P. Quillatre, and T Poinsot. "LES of explosions in venting chamber: a test case for premixed turbulent combustion models". In: *Comb. Flame* 183 (2017), pp. 207–223. DOI: http://dx.doi.org/10.1016/j.combustflame.2017.05.014.

[128] T J&amp Poinsot and SK Lele. "Boundary conditions for direct simulations of compressible viscous flows". In: *Journal of computational physics* 101.1 (1992), pp. 104–129. DOI: https://doi.org/10.1016/0021-9991(92)90046-2.

[129] Laurent Selle, Franck Nicoud, and Thierry Poinsot. "Actual impedance of nonreflecting boundary conditions: Implications for computation of resonators". In: *AIAA journal* 42.5 (2004), pp. 958–964. DOI: https://doi.org/10.2514/1.1883.

[130] V. Granet et al. "Comparison of Non reflecting Outlet Boundary Conditions for Compressible Solvers on Unstructured Grids". In: *AIAA journal* 48.10 (2010), pp. 2348–2364. DOI: https://doi.org/10.2514/1.J050391.

[131] Guillaume Daviller, Gorkem Oztarlik, and Thierry Poinsot. "A generalized non-reflecting inlet boundary condition for steady and forced compressible flows with injection of vortical and acoustic waves". In: *Computers & Fluids* 190 (2019), pp. 503–513. DOI: https://doi.org/10.1016/j.compfluid.2019.06.027.

[132] JD Ramshaw, PJ O'Rourke, and LR Stein. "Pressure gradient scaling method for fluid flow with nearly uniform pressure". In: *Journal of Computational Physics* 58.3 (1985), pp. 361–376. DOI: https://doi.org/10.1016/0021-9991(85)90168-8.

[133] PJ O'Rourke and FV Bracco. "Two scaling transformations for the numerical computation of multidimensional unsteady laminar flames". In: *Journal of Computational Physics* 33.2 (1979), pp. 185–203. DOI: https://doi.org/10.1016/0021-9991(79)90015-9.

[134] *http://www.prolb-cfd.com/research-and-development/*. CLIMB: ComputationaL methods with Intensive Multiphysics Boltzmann solver BPIFrance Project No. P3543-24000.

[135] Yu Hou et al. "Lattice-Boltzmann and Navier-Stokes Simulations of the Partially Dressed, Cavity-Closed Nose Landing Gear Benchmark Case". en. In: *25th AIAA/CEAS Aeroacoustics Conference*. Delft, The Netherlands: American Institute of Aeronautics and Astronautics, 2019. DOI: 10.2514/6.2019-2555.

[136] Hatem Touil, Denis Ricot, and Emmanuel Lévêque. "Direct and large-eddy simulation of turbulent flows on composite multi-resolution grids by the lattice Boltzmann method". en. In: *Journal of Computational Physics* 256 (2014), pp. 220–233. DOI: 10.1016/j.jcp.2013.07.037.

[137] Jérôme Jacob, Orestis Malaspinas, and Pierre Sagaut. "A new hybrid recursive regularised Bhatnagar–Gross–Krook collision model for Lattice Boltzmann method-based large eddy simulation". In: *Journal of Turbulence* (2018). Publisher: Taylor & Francis, pp. 1–26. DOI: 10.1080/14685248.2018.1540879.

[138] Thomas Astoul et al. "Lattice Boltzmann method for computational aeroacoustics on non-uniform meshes: a direct grid coupling approach". en. In: *arXiv:2004.14887 [physics]* (2020). arXiv: 2004.14887.

[139] Sebastien Bocquet et al. "Evaluation of the Lattice Boltzmann Method for Aero-acoustic Simulations of Industrial Air Systems". en. In: *25th AIAA/CEAS Aeroacoustics Conference*. Delft, The Netherlands: American Institute of Aeronautics and Astronautics, 2019. DOI: 10.2514/6.2019-2415.

[140] B. Dorschner et al. "Grad's approximation for moving and stationary walls in entropic lattice Boltzmann simulations". en. In: *Journal of Computational Physics* 295 (2015), pp. 340–354. DOI: 10.1016/j.jcp.2015.04.017.

[141] Mario Falese. "A study of the effects of bifurcations in swirling flows using Large Eddy Simulation and mesh adaptation". PhD thesis. Institut Natioanl Polytechnique de Toulouse, 2013.

[142] Guillaume Daviller et al. "A Mesh Adaptation Strategy to Predict Pressure Losses in LES of Swirled Flows". In: *Flow, Turbulence and Combustion* 99.1 (2017), pp. 93–118. DOI: 10.1007/s10494-017-9808-z.

[143] M Hall. "Cell vertex multigrid solution of the Euler equations for transonic flow past aerofoils". In: *Rapport technique, Royal Aerospace Establishment* (1984), p. 26.

[144] Franck Nicoud et al. "Using singular values to build a subgrid-scale model for large eddy simulations". In: *Physics of Fluids* 23.8 (2011), p. 085106. DOI: https://doi.org/10.1063/1.3623274.

[145] Timm Krüger et al. *The Lattice Boltzmann Method: Principles and Practice*. en. Graduate Texts in Physics. Cham: Springer International Publishing, 2017. DOI: 10.1007/978-3-319-44649-3.

[146] R. Courant, K. Friedrichs, and H. Lewy. "On the Partial Difference Equations of Mathematical Physics". In: *IBM J. Res. & Dev.* 11.2 (1967), pp. 215–234. DOI: 10.1147/rd.112.0215.

[147] Emmanuel Lévêque et al. "Shear-improved Smagorinsky model for large-eddy simulation of wall-bounded turbulent flows". In: *Journal of Fluid Mechanics* 570 (2007). Publisher: Cambridge University Press (CUP), pp. 491–502. DOI: 10.1017/S0022112006003429.

[148] Kilian Oberleithner et al. "Formation and flame-induced suppression of the precessing vortex core in a swirl combustor: Experiments and linear stability analysis". In: *Comb. Flame* 162.8 (2015), pp. 3100–3114.

[149] S Terhaar, K Oberleithner, and C O Paschereit. "Key parameters governing the precessing vortex core in reacting flows: An experimental and analytical study". In: *Proc. Comb. Inst.* 35 (2014).

[150] Jonas P Moeck et al. "Nonlinear interaction between a precessing vortex core and acoustic oscillations in a turbulent swirling flame". In: *Comb. Flame* 159.8 (2012), pp. 2650–2668.

[151] N. Syred. "A review of oscillation mechanims and the role of the precessing vortex core in swirl combustion systems". In: *Prog. En. Comb. Sci* 32.2 (2006), pp. 93–161.

[152] Dominik Schuster, Eric Climent, and Ulrich Rüde. "From hydrodynamic to granular regime: Particle laden flows around a cylinder". In: (2021).

[153] Oliver Stein et al. "Towards Comprehensive Coal Combustion Modelling for LES". In: *Flow Turbulence Combust* 90 (2012), pp. 859–884. DOI: 10.1007/s10494-012-9423-y.

[154] Wojciech P. Adamczyk et al. "Modeling of particle transport and combustion phenomena in a large-scale circulating fluidized bed boiler using a hybrid Euler–Lagrange approach". In: *Particuology* 16 (2014), pp. 29–40. DOI: 10.1016/j.partic.2013.10.007.

[155] Srdjan Belošević et al. "Numerical prediction of processes for clean and efficient combustion of pulverized coal in power plants". en. In: *Applied Thermal Engineering*. 6th International Conference on Clean Coal Technologies CCT2013 74 (2015), pp. 102–110. DOI: 10.1016/j.applthermaleng.2013.11.019.

[156] Y. Tang et al. "Direct numerical simulations and experiments of a pseudo-2D gas-fluidized bed". In: *Chemical Engineering Science* 143 (2016), pp. 166–180. DOI: https://doi.org/10.1016/j.ces.2015.12.026.

[157] Amir Esteghamatian et al. "Particle resolved simulations of liquid/solid and gas/solid fluidized beds". In: *Physics of Fluids* 29.3 (2017), p. 033302. DOI: 10.1063/1.4979137.

[158] Timm Krüger, David Holmes, and Peter V. Coveney. "Deformability-based red blood cell separation in deterministic lateral displacement devices—A simulation study". en. In: *Biomicrofluidics* 8.5 (2014), p. 054114. DOI: 10.1063/1.4897913.

[159] Rajat Mittal, Rui Ni, and Jung-Hee Seo. "The flow physics of COVID-19". In: *Journal of Fluid Mechanics* 894 (2020), F2. DOI: 10.1017/jfm.2020.330.

[160] Christoph Rettinger et al. "Fully Resolved Simulations of Dune Formation in Riverbeds". In: *High Performance Computing*. Ed. by Julian M. Kunkel et al. Cham: Springer International Publishing, 2017, pp. 3–21.

[161] F. Lachaussée et al. "Competitive dynamics of two erosion patterns around a cylinder". In: *Phys. Rev. Fluids* 3 (1 2018), p. 012302. DOI: 10.1103/PhysRevFluids.3.012302.

[162] Homann, H. et al. "Effect of turbulence on collisions of dust particles with planetesimals in protoplanetary disks". In: *A&A* 589 (2016), A129. DOI: 10.1051/0004-6361/201527344.

[163] Qing Li et al. "Near-wall dynamics of a neutrally buoyant spherical particle in an axisymmetric stagnation point flow". In: *Journal of Fluid Mechanics* 892 (2020), A32. DOI: 10.1017/jfm.2020.185.

[164] Qing Li, Micheline Abbas, and Jeffrey F. Morris. "Particle approach to a stagnation point at a wall: Viscous damping and collision dynamics". In: *Phys. Rev. Fluids* 5 (10 2020), p. 104301. DOI: 10.1103/PhysRevFluids.5.104301.

[165] Payman Jalali. "Flow characteristics and stresses on cylindrical objects immersed in a flow of inelastic hard disks". In: *Powder Technology* 219 (2012), pp. 217–227. DOI: https://doi.org/10.1016/j.powtec.2011.12.047.

[166] Holger Homann and Jérémie Bec. "Concentrations of inertial particles in the turbulent wake of an immobile sphere". In: *Physics of Fluids* 27.5 (2015), p. 053301. DOI: 10.1063/1.4919723.

[167] Zhaoyu Shi et al. "Bow shock clustering in particle-laden wetted cylinder flow". In: *International Journal of Multiphase Flow* 130 (2020), p. 103332. DOI: https://doi.org/10.1016/j.ijmultiphaseflow.2020.103332.

[168] Kun Luo et al. "Transient, three-dimensional simulation of particle dispersion in flows around a circular cylinder Re=140–260". In: *Fuel* 88.7 (2009), pp. 1294–1301. DOI: https://doi.org/10.1016/j.fuel.2008.12.026.

[169] Sandro Longo, Alessandro Valiani, and Luisfilippo Lanza. "Experiments on the two-dimensional flow of a grain–water mixture past a circular cylinder". In: *European Journal of Mechanics - B/Fluids* 36 (2012), pp. 139–151. DOI: https://doi.org/10.1016/j.euromechflu.2012.04.002.

[170] Hamed Haddadi et al. "Suspension flow past a cylinder: particle interactions with recirculating wakes". In: *Journal of Fluid Mechanics* 760 (2014), R2. DOI: 10.1017/jfm.2014.613.

[171] Hamed Haddadi, Shahab Shojaei-Zadeh, and Jeffrey F. Morris. "Lattice-Boltzmann simulation of inertial particle-laden flow around an obstacle". In: *Phys. Rev. Fluids* 1 (2 2016), p. 024201. DOI: 10.1103/PhysRevFluids.1.024201.

[172] C. Rettinger and U. Rüde. "A coupled lattice Boltzmann method and discrete element method for discrete particle simulations of particulate flows". In: *Computers & Fluids* 172 (2018), pp. 706–719. DOI: https://doi.org/10.1016/j.compfluid.2018.01.023.

[173] Dominique Legendre et al. "A note on the modelling of the bouncing of spherical drops or solid spheres on a wall in viscous fluid". In: *Chemical Engineering Science* 61.11 (2006), pp. 3543–3549. DOI: https://doi.org/10.1016/j.ces.2005.12.028.

[174] K Williamson. "Vortex Dynamics in the Cylinder Wake". en. In: *Annual Review of Fluid Mechanics* 28.1 (1996), pp. 477–539. DOI: doi:10.1146/annurev.fl.28.010196.002401.

[175] C. Norberg. "Fluctuating lift on a circular cylinder: review and new measurements". en. In: *Journal of Fluids and Structures* 17.1 (2003), pp. 57–96. DOI: 10.1016/S0889-9746(02)00099-3.

[176] S. C. R. Dennis and Gau-Zu Chang. "Numerical solutions for steady flow past a circular cylinder at Reynolds numbers up to 100". In: *Journal of Fluid Mechanics* 42.3 (1970), pp. 471–489. DOI: 10.1017/S0022112070001428.

[177] C. Wieselsberger. "New Data on the Laws of Fluid Resistance". In: 1922.

[178] K. O. L. F. Jayaweera and B. J. Mason. "The behaviour of freely falling cylinders and cones in a viscous fluid". In: *Journal of Fluid Mechanics* 22.4 (1965), pp. 709–720. DOI: 10.1017/S002211206500109X.

[179] D. J. Tritton. "Experiments on the flow past a circular cylinder at low Reynolds numbers". In: *Journal of Fluid Mechanics* 6.4 (1959), pp. 547–567. DOI: 10.1017/S0022112059000829.

[180] Hélène Persillon and Marianna Braza. "Physical analysis of the transition to turbulence in the wake of a circular cylinder by three-dimensional Navier–Stokes simulation". en. In: *Journal of Fluid Mechanics* 365 (1998), pp. 23–88. DOI: 10.1017/S0022112098001116.

[181] Madeleine Coutanceau and Roger Bouard. "Experimental determination of the main features of the viscous flow in the wake of a circular cylinder in uniform translation. Part 1. Steady flow". en. In: *Journal of Fluid Mechanics* 79.02 (1977), p. 231. DOI: 10.1017/S0022112077000135.

[182] A. Einstein. "Eine neue Bestimmung der Moleküldimensionen". In: *Annalen der Physik* 324.2 (1906), pp. 289–306. DOI: https://doi.org/10.1002/andp.19063240204.

[183] G. K. Batchelor and J. T. Green. "The determination of the bulk stress in a suspension of spherical particles to order c^2". In: *Journal of Fluid Mechanics* 56.3 (1972), pp. 401–427. DOI: 10.1017/S0022112072002435.

[184] Irvin M. Krieger and Thomas J. Dougherty. "A Mechanism for Non-Newtonian Flow in Suspensions of Rigid Spheres". In: *Transactions of the Society of Rheology* 3.1 (1959), pp. 137–152. DOI: 10.1122/1.548848.

[185] Chun-Hway Hsueh and Paul F. Becher. "Effective Viscosity of Suspensions of Spheres". In: *Journal of the American Ceramic Society* 88.4 (2005), pp. 1046–1049. DOI: https://doi.org/10.1111/j.1551-2916.2005.00204.x.

[186] H. Eilers. "Die Viskosität von Emulsionen hochviskoser Stoffe als Funktion der Konzentration". In: *Kolloid-Zeitschrift* 97.3 (1941), pp. 313–321. DOI: 10.1007/BF01503023.

[187] Talib Dbouk. "A suspension balance direct-forcing immersed boundary model for wet granular flows over obstacles". In: *Journal of Non-Newtonian Fluid Mechanics* 230 (2016), pp. 68–79. DOI: https://doi.org/10.1016/j.jnnfm.2016.01.003.

[188] S. Wilhelm, J. Jacob, and P. Sagaut. "An explicit power-law-based wall model for lattice Boltzmann method–Reynolds-averaged numerical simulations of the flow around airfoils". In: *Physics of Fluids* 30.6 (2018), p. 065111. DOI: 10.1063/1.5031764.